# Experimental Investigation of Effect of Gravity on Properties of Parts Fabricated by Fused Deposition Modeling Additive Manufacturing

Angela Huang

A THESIS SUBMITTED TO THE FACULTY OF GRADUATE STUDIES
IN PARTIAL FULFILLMENT OF THE REQUIREMENTS FOR THE DEGREE OF
MASTER OF SCIENCE

Graduate Program in Mechanical Engineering

York University
Toronto, Ontario

## Abstract

Additive manufacturing in space has the potential to revolutionize space exploration by enabling the in-situ production of parts. Although fused deposition modeling (FDM) additive manufacturing has been demonstrated in microgravity, its impact on the properties of FDM printed components remains unclear. This thesis attempts to reveal how microgravity affects the mechanical and material properties of parts printed by FDM with microgravity conditions simulated by varying raster and print orientations relative to gravity in the printing process.

The experimental study examines the tensile, compressive, and dimensional properties of fabricated specimens, noting a general decline in tensile strength with increased gravity level at interfacial layers, except for full-gravity specimens that showed a different failure mechanism. Compressive strength and dimensions also decreased with higher gravity. Micro-CT imaging revealed voids, air gaps, and poor interlayer bonding in specimens at low gravity. These findings enhance the understanding of how gravity conditions impact FDM additive manufacturing.

## Acknowledgments

For those who have supported me for the past two years: my family, my friends, and my boyfriend, Tristan.

To my research group, the bright graduate students of York's Mechanical Engineering department, and the unfailingly knowledgeable lab technicians, who guided me and inspired me with their hard work.

To my supervisor, Dr. Zheng Hong (George) Zhu, who is an excellent example of professorial leadership and nurturing.

# Table of Contents

## List of Tables

## List of Figures

## List of Abbreviations

| | |
|---|---|
| ABS | Acrylonitrile Butadiene Styrene |
| AM | Additive Manufacturing |
| ANOVA | Analysis of Variance |
| ASTM | American Society for Testing and Materials |
| FDM | Fused Deposition Modelling |
| FFF | Fused Filament Fabrication |
| ISM | In-Space Manufacturing |
| Micro-CT | Micro Computed Tomography |
| SR30 | Soluble Support Removal |
| UCS | Ultimate Compressive Strength |
| UTS | Ultimate Tensile Strength |

# Chapter 1 Introduction

## 1.1. Motivation and Justification of Research

Space exploration, as it extends further from Earth, has been significantly hindered by logistical constraints, including the weight and volumetric limits of launch vehicles, the complexity and costs of resupply missions, and the challenges associated with in-situ repair [1]. Current space missions, e.g., the International Space Station (ISS) and the Tiangong Space Station (TSS), rely on launch vehicles from Earth for supplies. To reduce dependency on resupply ships and thus make long-distance and duration space missions feasible, a new method of in-space manufacturing must be established.

Additive manufacturing (AM), or 3D printing, provides a paradigm shift for future space exploration missions by fabricating structures and/or parts of various shapes in situ [2] and building layer by layer out of plastic, metal, or other materials. It is estimated that the spacecraft made in space by AM could save mass by 40 to 90% and reduce fabrication times by months and years [3]. Traditional AM techniques face numerous challenges in the extraterrestrial environment, specifically within the micro/zero-gravity conditions of space. The difficulties and complexities in handling fabricating materials in liquid and powder forms in microgravity make Fused Deposition Modelling (FDM) or Fused Filament Fabrication (FFF) the preferred technology aboard spacecraft for plastics [4]. In the FDM process, a thermoplastic filament is melted and extruded through a heated nozzle, which precisely deposits it onto the top of previous layers following a digital

model's path to construct the object from the bottom-up layer by layer. The extruded material quickly solidifies, bonding with the layers below as they cool. The key to successful FDM printing is ensuring proper adhesion and alignment between layers, maintaining the object's shape and precision [5].

There is limited research on the impact of microgravity on the material and mechanical properties of FDM-AM parts. The unique conditions of microgravity significantly influence the behavior of polymers during the printing process, as well as the properties of the final printed parts. Understanding these effects is crucial for optimizing printing techniques and ensuring the reliability and functionality of printed components in space missions.

This thesis fills this gap by investigating the effects of microgravity on the mechanical strength, dimensions, and material properties of FDM-AM parts. The study employs a ground-based method to simulate microgravity conditions during the FDM 3D printing process to achieve this.

## 1.2. Research Objectives

This study investigates the influence of gravity on the mechanical properties and dimensional accuracy of parts fabricated by FDM AM using ABS-M30. Specifically, this thesis studies the effect of gravity magnitude relative to layer interface on

1. the bonding strength between raster interlayers,
2. the tensile properties of FEM AM parts, including ultimate tensile strength (UTS), fracture stress, and fracture strain, yield strength, and Young’s Modulus,
3. the compressive properties of FDM AM parts, such as ultimate compressive strength, fracture strain, fracture stress, yield strength, compressive modulus, and densification

modulus, and

4. the dimensional accuracy of FDM AM parts.

## 1.3. Layout of Thesis

As the FDM process was the only 3D-printing method employed in this thesis, all references henceforth shall be to it. The layout of this thesis is structured as follows: Chapter 1 introduces the work. Chapter 2 presents a comprehensive literature review of the state-of-the-art in the field to justify this study. This includes the FDM and FFF processes, the resultant anisotropy caused by build orientation and raster angle, the significance of interlayer fusion on mechanical properties, and the challenges and considerations specific to in-space FDM/FFF applications. Chapter 3 details the manufacturing process of the testing specimens, with a focus on how the microgravity environment was simulated through careful manipulation of build orientation and raster angle. Chapter 4 provides a thorough description of the tests conducted to evaluate the mechanical properties of the specimens. Chapter 5 discusses the processing of the data collected during experimentation, including an in-depth analysis of the gathered data, identifying any trends and interpreting the findings. Finally, Chapter 6 presents the conclusions and avenues for future research and applications.

# Chapter 2 Literature Review

## 2.1. In-Space Polymer Additive Manufacturing

Much pioneering research has been attempted to extend FDM into space. FDM and FFF have been successfully tested in microgravity environments using various platforms. These platforms include drop towers, which provide short microgravity periods (1.3 to 9.5 seconds) [6], parabolic flights offering ~22 seconds of microgravity per maneuver [7], sounding rockets with 3 to 20 minutes of free-fall microgravity [2], and ISM aboard space stations or specialized satellites [8]. Cowley *et al.* demonstrated that careful selection of printing parameters can mitigate significant impacts caused by gravity fluctuations, although variable loads may still affect the structure and performance of printed parts [9].

NASA pioneered AM in space since 2000 and sponsored the company, Made In Space, Inc., in 2014 to successfully demonstrate the first part made by FDM with ABS in microgravity inside the ISS [10]. In comparison with the same part printed on Earth, their findings revealed that space-printed specimens were denser and demonstrated higher tensile and flexural strength against ground-based counterparts [11], [12], [13]. This phase also observed material densification, particularly at the specimen's bottom half. Their subsequent work in 2018 refined the manufacturing process by controlling extruder standoff distance, and it was found that mechanical properties were only marginally increased by the microgravity environment [12]. It was determined that inconsistency in extruder standoff in the 2014 study was the major cause in

variability between the samples made on Earth and in microgravity condition [14]. However, another work in 2019 utilized a physics-based model to simulate the process under various conditions and found that the specimen showed no engineering-significant microgravity effect on mass, density, tensile and compression properties, and internal material structure [15]. Soon after NASA in-space AM experiments, ESA demonstrated its first 3D polymer printer in the ISS in 2018 [16] and China conducted first 3D printing experiment in Tiangong Space Station in 2018 [17], all tested the FDM process. However, the details of space printed samples and mechanical/physical properties of ESA and Chinese experiments are not available in the public domain. Despite these advancements, the challenge remains of characterizing the global mechanical differences between FDM-AM polymer parts manufactured on Earth and in microgravity and zero-gravity environment. Given the scarcity of data of space printed parts, the inconsistent interpretation on microgravity effects the properties of space printed parts, and the limited access to microgravity 3D printing testbed in ISS, it is necessary to explore the implications of microgravity on the FDM process on Earth by controlled gravity conditions.

## 2.2. Polymer Fused Deposition Modelling

Polymeric Fused Deposition Modeling (FDM) and Fused Filament Fabrication (FFF) are among the most prevalent additive manufacturing (AM) techniques used to produce polymer-based parts. Both technologies involve the layer-by-layer deposition of thermoplastic materials to create three-dimensional objects. The terms FDM and FFF are often used interchangeably, although FDM is a trademarked term by Stratasys Inc. [18], [19], while FFF is the generic term used in the industry. The FDM process employs an externally heated, enclosed chamber, whereas the FFF process may or may not employ a heated chamber. An FFF chamber is ambiently heated from the print bed and the nozzle, not from an external chamber heater.

The FDM/FFF process begins with a digital 3D model sliced into thin horizontal layers using specialized software. Polymeric filament, typically a thermoplastic, is fed into an extrusion system by rollers and conveyed to the extruder head. The extruder head, which includes a heater and nozzle, melts and extrudes the filament as a viscous liquid. This liquid is then deposited onto a hot bed layer by layer to form a 3D object [20], [21]. This process continues until the entire model is built. Unlike other polymer shaping methods, this process does not use a feed screw or die; the filament is melted through thermal conduction and extruded through a circular nozzle, cooling and solidifying quickly with minimal shrinkage. Key parameters such as layer height, print speed, infill density, and nozzle temperature can be adjusted to optimize the print quality and mechanical properties of the final product. If needed, support structures can be added (breakaway or soluble) to certain part features to aid in the deposition process [22].

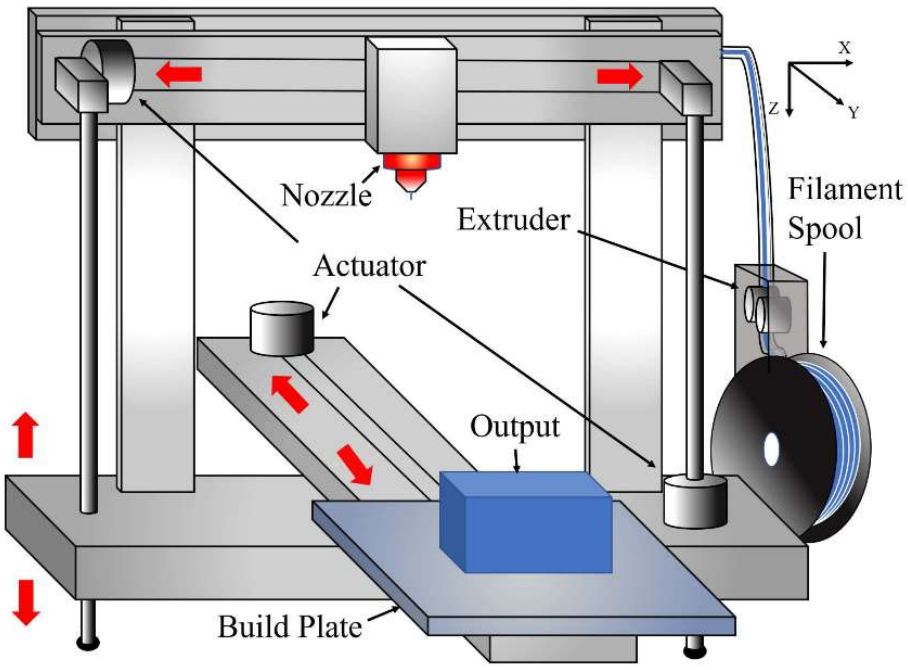


Figure 1 Schematic of a typical FDM/FFF printer with highlighted axes movement. (Courtesy of Creative Commons [23], [24])

The most common and cost-effective FDM/FFF systems have three degrees of freedom: the hotbed moves in the y and z directions, and the print head in the x and y directions. Figure 1 shows the typical configuration of an FDM/FFF printer and highlights how the various parts move along the x, y, and x axes.

Understanding the FDM/FFF process is crucial for providing the necessary background information about AM in microgravity environments. This foundational knowledge helps explain how layer-by-layer deposition works and why the mechanical properties of printed parts can be influenced by external conditions such as microgravity.

## 2.3. Mechanical Anisotropy in FDM/FFF Manufactured Polymer Parts

Anisotropy in FDM-AM parts is influenced by several factors, including the part's build orientation, the raster angle during printing, and the degree of interlayer fusion. Reduced gravity environments during FDM-AM, such as zero or microgravity, can exacerbate these effects by mimicking the mechanical outcomes of suboptimal build orientation, raster alignment, and poor interlayer bonding as typically seen in terrestrial environments. The following section examines these contributing factors to anisotropy in greater detail.

### 2.3.1. Build Orientation

One of the key challenges in FDM/FFF is the anisotropic nature of the printed parts. Anisotropy refers to the directional dependence of mechanical properties, which is a significant concern for parts subjected to mechanical loading. This variation is due to the nature of FDM parts, which possess macroscopic entities such as infill pattern, interlayer fusion, and raster angle. Traditional methods, such as injection molding, produce parts of far superior mechanical strength [24]. Compared to injection molded ABS parts, tensile strength was found to be 48-72% lower and compressive strength 57-90% lower [24], [25]. For polycarbonate parts (PC), tensile strength was

30-53% lower than those of specimens composed of bulk material [26]. Carneiro *et al.* [27] noted a 20-30% decrease in the tensile properties of (PP) and glass-reinforced polypropylene (GRPP) produced via FDM compared to those produced via compression molding. The mechanical properties of FDM/FFF parts, such as tensile strength, impact resistance, and flexural strength, are highly dependent on the build orientation and the printing parameters [28], [29], [29], [30], [31]. Compressive strength [32], creep [33], and fatigue properties are also highly anisotropic depending on build orientation [24], [34]. In general, parts printed with layers parallel to the loading direction (see Figure 2, namely the XZ and XY orientations) exhibit higher strength compared to those printed with layers perpendicular to the loading direction (ZX) [28], [35], [36].

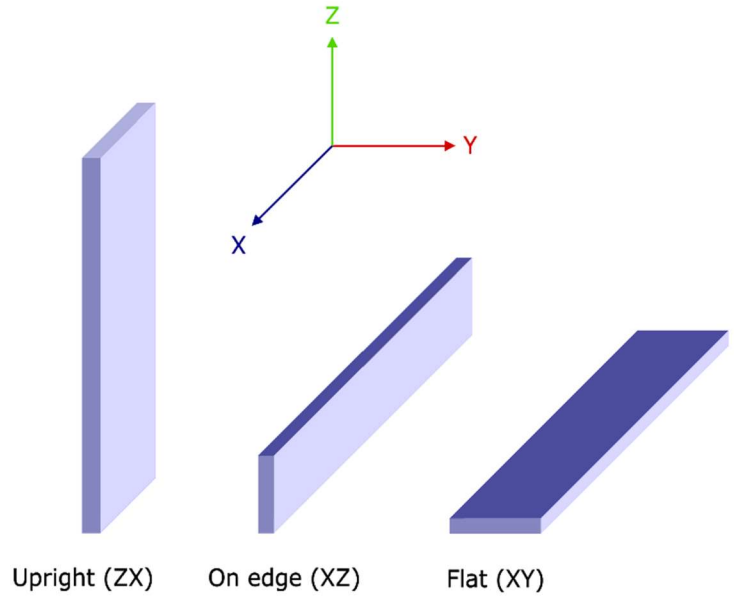

Figure 2 FDM manufacturing axes and their nomenclature.

Generally, specimens printed with XZ and XY orientation have higher strength, with ZX orientation being the weakest [37], [38], [39]. Chacón *et al.* [40], printing PLA via FFF, found that specimens printed with ZX orientation possessed 47% lower tensile strength (25.1 MPa) than specimens printed with XZ and XY orientations. It was also discovered that the XZ orientation is

optimal for strength, stiffness, and ductility. Similarly, using FFF and PLA, Lanzotti *et al.* [41] found that fatigue strength decreases as infill orientation becomes more parallel to the x-axis, with the lowest values seen in infill orientations closer to the y-axis.

In accordance with the axes presented in Figure 2, Raut *et al.* [42] found that the maximum tensile strength of ABS-P400 occurs in specimens printed parallel to the y-axis (XY), whereas maximum flexural strength occurs in specimens parallel to the x-axis (XZ). In this same study, specimens printed at 45° to the z-axis showed the weakest tensile and flexural results. Also, using ABS-P400, Sood *et al.* [43] found that tensile and flexural strength decreases as the specimen's angle to the print bed increases. For reference, a specimen printed at 0° is flat to the print bed, while 90° is parallel to the z-axis. Hossain *et al.* [44] discovered that the maximum tensile strength occurs for PC specimens with XZ orientation, while the lowest tensile strength occurs for specimens with ZX orientation. It should be noted that [44] did not investigate the XY orientation, as seen in Raut *et al.* [42]. Es-Said *et al.* [45], Onwubolu and Rayegani [46], and Raut *et al.* [42] found that ABS and ABS P400 specimens printed horizontally on the print bed, with longitudinal layers (XY), exhibit greater tensile strength and impact resistance. Lee *et al.* [32] found that the compressive strength of ABS specimens was 11.6% higher for build orientations aligned with the x-axis, as opposed to those aligned with the z-axis. Build orientation appears to have less influence on compressive strength than tensile strength [25]. Varying build orientation yielded maximum compressive properties differences of only 11% because compression-mode failure occurs via layer tear-off rather than fracture at the bond interface [38].

The relationship between build orientation and significant mechanical anisotropy remains despite the variation of other factors that may affect specimen strength, such as layer thickness, nozzle temperature, and filament feed rate [38], [40]. This is due to the close relationship between

build orientation and raster angle, which will be further explored upon in the next section.

### 2.3.2. Raster Angle

Raster angle is defined as the angle of the deposited polymer path with respect to the x-axis [47], measured from -90° to 0° to 90°. As rasters primarily bear the tensile load [48], variations in raster angle significantly affect mechanical properties and how the load is transferred within the specimen [49], [50], [51]. Specimens with a 0° raster exhibit slightly lower tensile strength comparted to injection-molded counterparts due to discontinuities in the interlayer caused by voids that reduce the load-bearing area [48]. As the raster angle increases from 0° to 90°, the raster interlayer takes on a greater role in load-bearing, leading to a decrease in tensile properties [24], [52]. Gao *et al*. [48] showed that as the raster angle increased from 0° to 90°, the tensile strength of PLA specimens decreased from 64.3 MPa to 25.7 MPa. Li *et al.* [53] showed a similar decrease, from 34.87 MPa to 26.72 MPa for polyamide 12 (PA-12). The trend of 90° raster being weaker than lower angle raster is consistent with nearly all FDM/FFF produced thermoplastic parts under tensile loading [54], [55], [56], [57]. The same trend is observed for flexural strength, while the opposite is observed for compressive properties [51]. The anisotropic effects of the raster angle can be negated with an alternating layer pattern of +45°/-45° raster in the XZ and XY build orientations [58]; for this reason, FDM/FFF machines often have this as an automatic setting for tensile strength optimization. Based on these trends in the literature, it can be reasonably inferred that the interfacial bonds between raster layers are weaker than the bulk material.

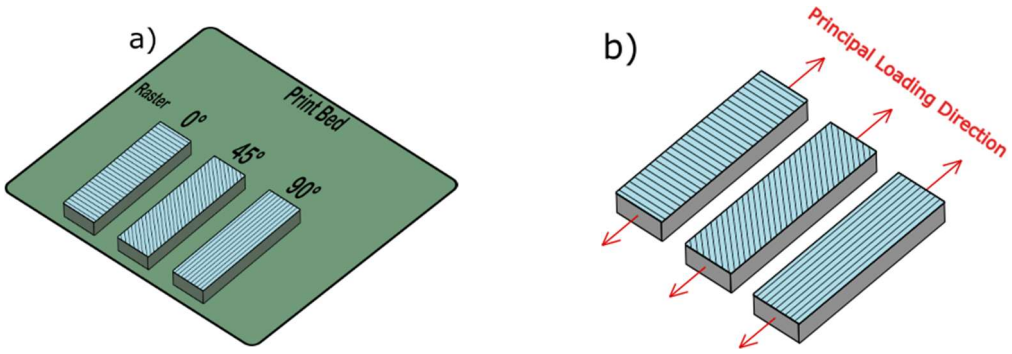

Figure 3 (a) Schematic representation of raster angle with respect to axes on a print bed (b) raster angle in relation to the principal loading direction.

The existing literature on raster angle-induced anisotropy primarily focuses on the tensile properties of samples printed with XZ and/or XY build orientation. Specimens printed in the ZX orientation tend to fail along the interlayer bond, making them unsuitable candidates for raster angle analysis, whereas XZ and XY orientation prints fail along the raster [40]. Loading conditions such as flexure, compression, and fatigue involve complex interactions of shear and stress, making it difficult to determine if the values obtained are due solely to the raster [59]. Therefore, the remainder of this section will focus on anisotropy in tensile properties.

The term "degree of anisotropy ($D_a$)" is used to quantify anisotropy. Knowing that 0° raster produces the strongest specimens and 90° the weakest, $D_a$ for tensile mode can be calculated as:

$$D_a = \frac{UTS_0 - UTS_{90}}{UTS_0} \times 100\% \quad (1)$$

where UTS represents ultimate tensile strength, while the subscripts 0 and 90 represent raster angle. Generally, specimens printed with ABS exhibit higher $D_a$ than other thermoplastic polymers, with values ranging between 43-86% [24], [60], [61], [62]. For PLA specimens, $D_a$ is variable but still significant, between 14-60% [41], [48], [60], [63], [64]. Parts fabricated from polyether ketone (PEEK) and thermoplastic polyurethane (TPU) show $D_a$ values between 10-26% [65], [66], [67]

and 24-39% [68], respectively. Certain materials, such as PA-12, polypropylene (PP), and polyethylene (PE) exhibit $D_a$ values so low that they are nearly isotropic. Specifically, PA-12 parts range between 9.8-11% [53], [69], [70], PP between 4-14% [27], [71], [72], and PE between 0-1.5% [73].

## 2.4. Interlayer Fusion

In the context of FDM and FFF, interlayer fusion refers to the process by which successive layers of extruded thermoplastic material bond together to form a solid, cohesive structure. This process is critical for the mechanical integrity and overall quality of the printed part. It should be noted that there are two types of interlayers in the FDM print process: the raster interlayer, and the regular interlayer. Regular interlayer fusion deals with the bonding between one entire layer and the next, ensuring that each successive layer adheres well to the previous one. On the other hand, raster interlayer fusion specifically refers to the bonding between adjacent rasters of material within the same layer. Figure 4 depicts a detailed view of the raster interlayer on a computer-generated image.

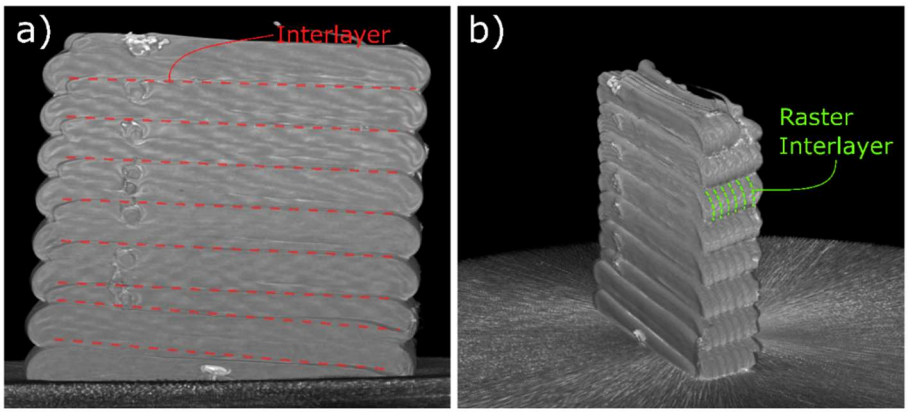


Figure 4 (a) X-ray image of an FDM ABS specimen with dashed lines highlighting areas of interlayer fusion; (b) Same specimen, with dashed lines highlighting areas of raster interlayer fusion.

Testing methods isolating the measurement of interlayer bond strength place the principal loading direction along the z-axis. In reference to Figure 2, a specimen of ZX orientation would be used. In the ZX orientation, almost all specimens fail at the interlayer bond [40]. The interlayer is the mechanically weakest part of an FDM/FFF specimen: ZX orientation builds are usually weaker than XZ and XY builds [24], [52].

### 2.4.1. Mechanisms of Interlayer Fusion

The functionality of interlayer fusion in the FDM process is affected by the level of gravity present. On Earth, gravity assists in pulling layers together as they are deposited. During FDM/FFF, molten polymer fibre is extruded and deposited onto the previous layer [74], allowing the two layers to make surface contact. Following contact, surface tension drives neck growth at the interface [75], while viscous and inertial forces act as resistant forces [75], [76]. Filament coalescence (synonymously: polymer chain entanglement or inter-molecular diffusion) instantaneously transpires after surface contact [77]. Inter-molecular diffusion occurs when polymer chains from adjacent layers penetrate into each other, entangling, and creating a strong bond [74], [78], [79]. The process is similar to polymer welding [75]. The strength of the bond is determined by the deposition/formation of the wetted interfaces and the extent of inter-molecular diffusion between the two polymer layers [80].

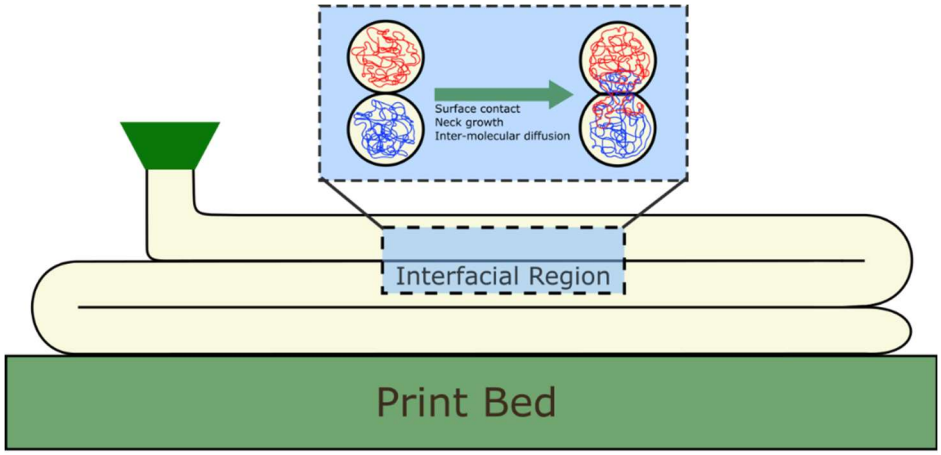

Figure 5 Visual of the interlayer fusion process.

FDM can be described as a melting-solidification process [80] that requires precise temperature control to achieve optimal properties. Controlling the temperature gradient in the interlayer during fabrication is crucial for ensuring good bond quality between adjacent polymer layers. As the deposited material cools from its extrusion temperature to ambient temperature, it undergoes thermal contraction, known as the shrinkage coefficient [81]. The layer deposited on top is hotter, and the thermal energy of this semi-molten freshly deposited material drives inter-molecular diffusion between adjacent layers [82]. If there is a large temperature gradient between the old and freshly deposited layers, then the non-uniform cooling rates can lead to the development of residual stress and strains within the part [83]. Higher thermal gradients during the solidification process results in lower internal stress relaxation, leading to higher residual stresses between layers, and this influences layer volume contraction, warping, and bond quality [82], [84]. Thermal control mechanisms, such as a heated print bed or a heated enclosed build chamber, can minimize the thermal gradient and these unwanted effects [85], [86]. Additionally, the width of the wetted surface is critical for interlayer adhesion. Using self-consistent field theory (SCFT), Zhang and Wang [87] showed that lower cooling rates result in larger wetted interfaces,

enhancing inter-molecular diffusion. However, prolonged exposure above the polymer's glass transition temperature ($T_g$) during the fabrication process lead to higher compressive residual strains [82]. Thus, optimal bond quality in the interlayer results from a low thermal gradient, with temperatures maintained close but not exceeding the glass transition temperature.

Periodic temperature fluctuations occur as new layers are deposited, as investigated by K-type thermocouples, infrared thermography, and heat transfer analysis [80], [88], [89]. Temperatures at the interface periodically peak and then cool to near print bed or build chamber temperatures. The bonding time between adjacent layers is very short, as the time spent above the polymer's glass transition temperature is only a couple seconds [90]. This timeframe is insufficient for complete neck formation and filament coalescence before polymer solidification; as a result, large amounts of voids are present at the interface [91]. In ABS, neck growth was found to occur at interfacial temperatures exceeding 200°C [75].

Chemical additives may be used to improve the strength of the interlayer bond. Stark [92] showed that the use of chemical cross-linking agents, specifically 4,4'-diaminodipheylmethane (DADPM), significantly improved the interlayer bond strength, and evidenced through T-peel tests. Li *et al.* [93] introduced 3wt% trisilanophenyl polyhedral oligomeric silsesquioxane (t-POSS) nanocomposites to PEEK filament, and found improvements in tensile strength and Young's modulus, near isotropy in the XY plane, and a reduction in porosity from 3.02% to 0.2%. It was found that the pyrolysis products of t-POSS (water, $CO_2$, and benzene derivatives) acted as plasticizers, which promoted the mobility of PEEK chains at the interface [93].

# Chapter 3 Methodology of Specimen Fabrication

This chapter provides a detailed description of the design and fabrication of specimens for tensile and compressive testing, along with the underlying rationale for each process. The chapter begins with the material selection, in-depth discussion of the tensile specimens, followed by the compression specimens. Finally, the chapter presents the samples prepared for qualitative micro-CT analysis, explaining the specific techniques and considerations involved in their production.

## 3.1. Acrylonitrile Butadiene Styrene

Acrylonitrile Butadiene Styrene, more commonly known as ABS, is a common thermoplastic polymer known for its good mechanical properties and ease of processing [94]. ABS has grown in popularity, specifically in its use for FDM and injection molding, due to its relatively low cost, recyclability, and robust range of applications [95], [96]. The name ABS is derived from its three constituent monomers: acrylonitrile, which contributes tensile strength, hardness, and resistance to heat and chemicals; butadiene, which enhances impact strength; and styrene, which in high concentrations improves processability, aiding in molding, mixing, and extruding [97], [98]. It has moderate tensile strength, high impact resistance, and good flexural strength, making it suitable for various structural applications and durable against physical shocks [97]. Additionally, ABS has moderate thermal resistance, typically up to 100°C, and moderate chemical resistance, resistant to aqueous and concentrated acids, alkalis, alcohols, salts, and oils [98], [99]. Table 1 shows the

mechanical and material properties of ABS.

Table 1 Mechanical Properties of Bulk ABS [100], [101], [102].

| Tensile Strength | | Tensile Elongation | Compressive Yield Strength | Compressive Modulus | Young's Modulus | Flexural Modulus | Impact Strength |
|---|---|---|---|---|---|---|---|
| Yield | Break | % | [MPa] | [GPa] | [GPa] | [GPa] | [J/m] |
| [MPa] | | | | | | | |
| 29.6-48 | 29.8-43 | 4.03 | 65 | 1.6-2.4 | 1.79-3.2 | 4.03 | 200-215 |

As previously mentioned, parts produced via FDM AM are anisotropic and possess different values based on the principal loading direction applied during testing. Table 2 shows the mechanical properties of additively manufactured ABS by FDM. Tensile properties are tested according to the American Society for Testing and Materials (ASTM) International D638 [103] standard and compressive properties of ASTM D695 [104].

Table 2 Mechanical Properties of FDM Additively Manufactured ABS.

| Tensile Properties | Unit | XZ axis | ZX axis | XY axis | Reference |
|---|---|---|---|---|---|
| Yield Strength | MPa | 21.7 | 17.2 | 21.68 | [105], [106] |
| Modulus | GPa | 1.46-2.20 | 1.62 | 0.65-1.54 | [102], [105], [106], [107] |
| Elongation at Yield | % | 2.8 | - | - | [107] |
| Elongation at Failure | % | 1.49-2.8 | 1.10 | 10.67 | [105], [106], [107] |
| Compressive Properties | | | | | |
| Yield Strength | MPa | 64.15 | 25 | 22.38 | [102], [106], [107] |
| Modulus | GPa | 1.243 | 0.478 | 0.484 | [102], [106], [107] |
| Strain at Failure/UCS | % | 73.34 | 17 | 23.67 | [102], [106], [107] |

The axes in Table 3 is shown in Figure 2. A specimen with XZ axis orientation is printed with the principal loading direction parallel to the X axis, with the width extending into the z-axis.

Similarly, a specimen with ZX axis orientation is printed with the principal loading direction parallel to the z-axis, with the width extending into the x-axis.

All specimens investigated in this thesis for tensile, compression, and micro-CT analysis were manufactured from ABS-M30. ABS-M30 is an enhanced, aerospace-grade variant of standard ABS offered by Stratasys. Relative to ABS, the ABS-M30 material exhibits higher tensile strength, flexural strength, impact resistance, and thermal resistance, thus making it a better choice for in-space manufacturing [108]. These qualities present it as an improvement over standard ABS for engineering applications, primarily for the low-volume production of highly customized parts, such as jigs, fixtures, and manufacturing tools [109]. The filament is optimized and proprietary to the Stratasys F370 FDM 3D printer, which was used to fabricate all specimens in this study. Bulk material properties for ABS-M30 are currently unavailable, but Table 3 shows the mechanical properties of additively manufactured ABS-M30.

Table 3 Mechanical Properties of FDM Additively Manufactured ABS-M30* [110].

| **Tensile Properties** | **Unit** | **XZ axis** | **σ†** | **ZX axis** | **σ** |
|---|---|---|---|---|---|
| Yield Strength | MPa | 30.8 | 0.85 | 27.5 | 0.28 |
| Modulus | GPa | 2.40 | 0.080 | 2.30 | 0.16 |
| Elongation at Yield | % | 1.8 | 0.43 | 1.7 | 0.13 |
| Strength at Failure | MPa | 28.1 | 0.58 | 26.8 | 0.84 |
| Elongation at Failure | % | 8.1 | 1.5 | 1.8 | 0.16 |
| Compressive Properties | | | | | |
| Yield Strength | MPa | 88.3 | 3.0 | 208 | 15 |
| Modulus | GPa | 2.20 | 0.11 | 2.16 | 0.092 |

* All specimens were manufactured on a Stratasys F900 FDM machine with a T16 tip.
† Standard deviation.

## 3.2. Fabrication of Testing Specimens

All specimens were fabricated in accordance with the American Society for Testing and Materials (ASTM) standards. These standards were ASTM D638 (type IV) and ASTM D695, for tensile and compression specimens, respectively [103], [104]. Figure 6 shows the dimensions for the specimens. Type IV specimens were chosen due to their suitability for testing rigid plastics such as ABS-M30. This geometry is particularly useful for directly comparing rigidity, which is quantified by Young's Modulus in tensile testing. Since parts used from ISM should only operate within their elastic range, any components that experience plastic deformation would be unsuitable for space missions. Young's Modulus is a key measure of stiffness in the elastic region, making it an ideal parameter for testing, and justifying the use of Type IV specimens for these evaluations.

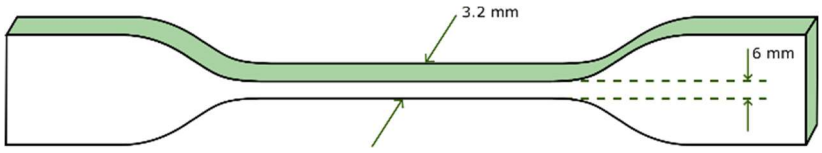


(a) Tensile specimen as per ASTM D638-IV.

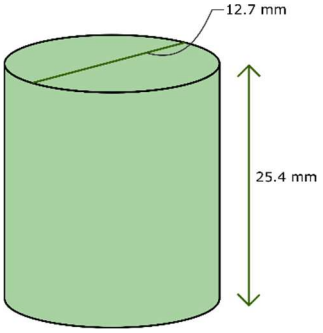


(b) Compressive specimen as per ASTM D695

Figure 6 Dimensions of tensile and compressive specimens. All measurements in millimeters.

## 3.3. Specimen Manufacturing Parameters

Figure 7 Stratasys F370 FDM 3D printer and tensile specimens encased in SR-30 [111] support structure.

The FDM 3D printer used to manufacture the specimens is Stratasys F370, see in Figure 7. The specimens were fabricated in accordance with the American Society for Testing and Materials (ASTM) standards D638-IV and D695, for tensile and compressive specimens, respectively. A distinctive aspect of our methodology involved the variation of print orientation relative to the gravitational direction. The specimens were printed at different angles, ranging from 0° to 90°, with increments of 15° between each orientation. This variation in orientation, hereafter referred to as "print orientation" was implemented to explore the impact of gravity on the mechanical properties and geometry precision of the ABS specimens.

## 3.4. Ground-Based Microgravity Mimicry

A custom raster pattern was developed for each layer printed to study the gravity influence on the interfacial bonding strength between the layers. This raster orientation was set at a 90° angle

relative to the principal loading direction anticipated during tensile and compressive testing, as shown in Figure 8. The aim of this approach was to evaluate the effects of gravity on the fusion between the deposited raster layers. The rationale behind this raster orientation was to ensure that the principal loading during testing would only act upon layers that are influenced together by gravitational force rather than directly on inherently stronger polymer deposition directions. Specifically, this methodological choice seeks to avoid loading conditions where the raster aligns constructively to the loading direction, which would result in an overestimation of the interlayer bonding strength. Along this line, any borders and surface finish automatically generated by the slicing software were removed to ensure the specimen was pure of one raster pattern. In this way, the impact of gravity variation on the interlayer bonding strength is isolated from material strength during testing. Figure 9 and Figure 10 depict the microstructure (raster and layering) of ASTM D638 and ASTM D695 tensile and compression coupons, respectively, and their relationship to the loading forces during testing. Figure 11 shows the force of gravity acting with respect to the raster interlayer.

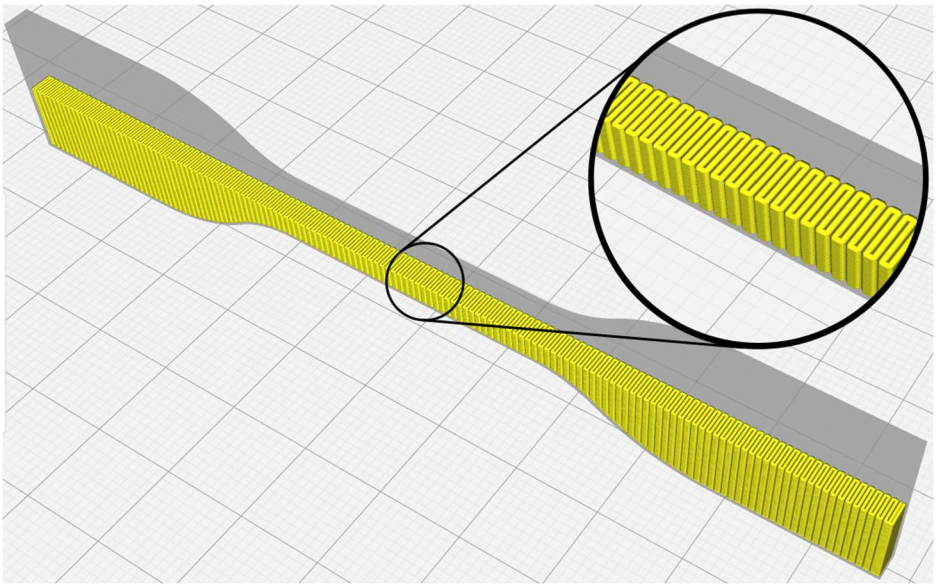

Figure 8 Cross-section of a sliced CAD file showing consistent 90° raster in an ASTM D638

tensile specimen, as seen on Cura Slicer software.

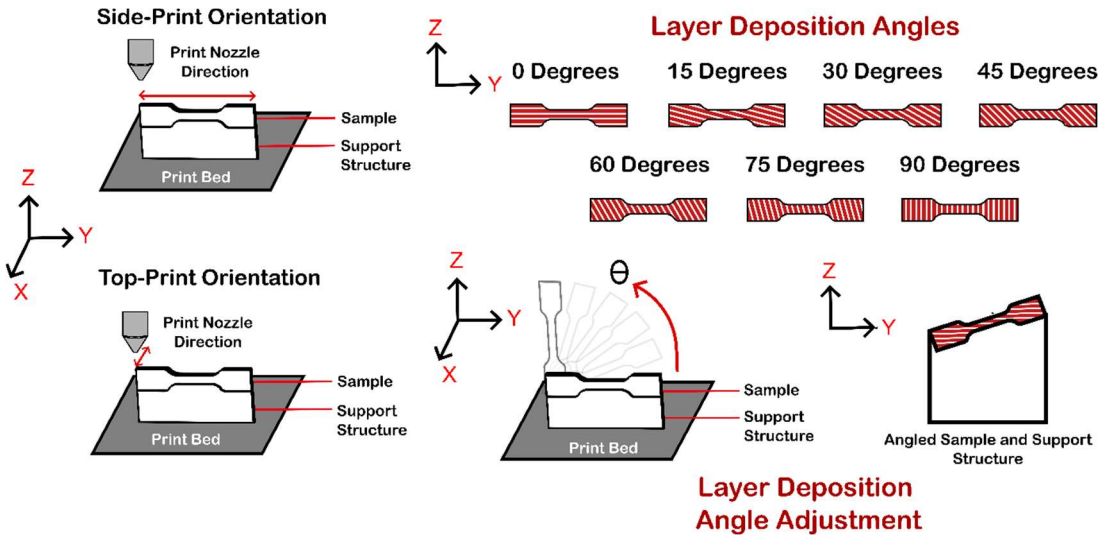


Figure 9 Graphic representation of the printing orientations and layer deposition patterns for tensile specimens according to ASTM D638-IV.

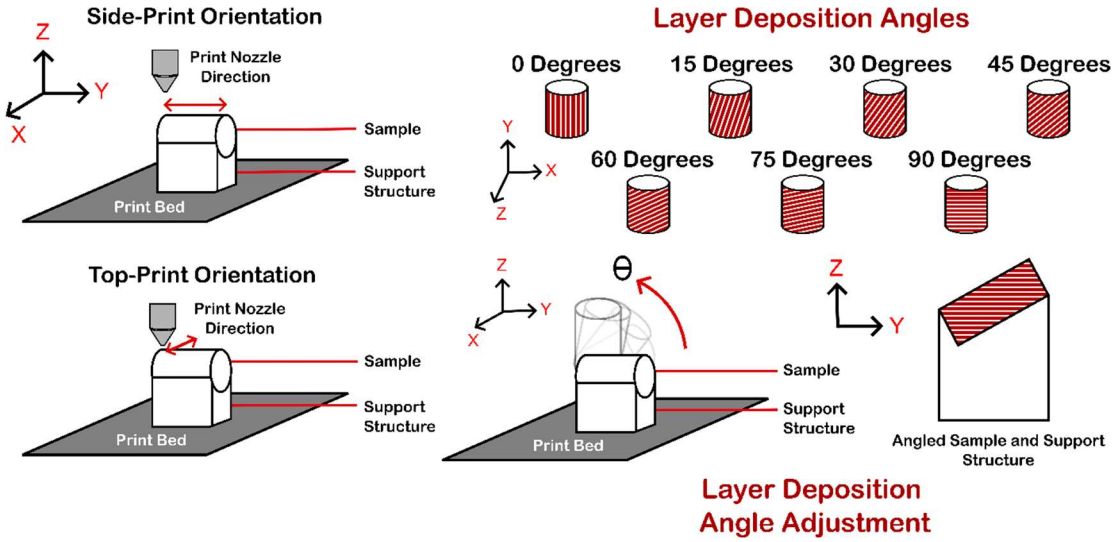


Figure 10 Graphic representation of the printing orientations and layer deposition patterns for compression specimens according to ASTM D695.

There is a trigonometric relationship between the gravitational force acting on deposited

layers and print orientation. The relationship is defined as:

$$g_f = g \sin\theta \tag{2}$$

where $g_f$ is the fractional gravity, $g$ is the Earth gravity at the sea level, and $\theta$ is the printing orientation. As an example, at a printing orientation of 15°, the fractional gravity acting on interlayer fusion is:

$$g_f\big|_{\theta=15^\circ} = g \sin 15^\circ = 0.259g \tag{3}$$

Figure 11 gives a representation of these calculations. Table 4 shows the fractional gravity acting on the interlayer interfaces at each printing orientation.

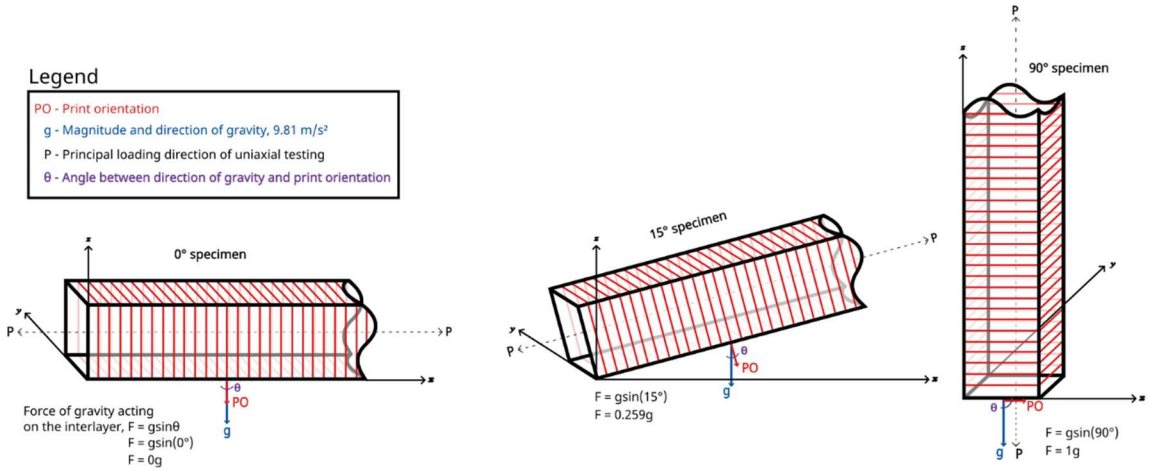


Figure 11 Graphic representation of the gravity direction relative to interlayer interfaces and the principal loading direction during uniaxial tensile and compression testing at each print orientation.

Table 4 Gravitational Force per Print Orientation.

| Print Orientation (°) | 0 | 15 | 30 | 45 | 60 | 75 | 90 |
|---|---|---|---|---|---|---|---|
| Fraction of Gravity at Layer Interface (g) | 0 | 0.259 | 0.5 | 0.707 | 0.866 | 0.966 | 1 |

## 3.5. FDM Parameters

Testing specimens were produced by a Stratasys F370 printer due to its compatibility with ABS-M30 and its ability to maintain a controlled environment suited for high-precision manufacturing.

ABS-M30 filament was heated to 270°C inside the printer's nozzle and the temperature in the printer's heated chamber was consistently maintained at 90°C. The nozzle's adjustable diameter was set to 0.254mm and operated with an accuracy of +/- 0.002mm/mm. This dimension also represents the deposited strand diameter (raster width) and the interlayer width. Percentage infill was set to 100% and the rate of polymer strand deposition was set to 250 mm/second. Table 5 summarizes the printing parameters. To ensure the utmost accuracy and repeatability, the printer's X, Y, and Z axes were calibrated before each printing session. This step guaranteed that the dimensions of the specimens remained consistent across all prints.

Table 5 FDM Printing Parameters

| Nozzle Temp. | Chamber Temp. | Nozzle Diameter | Percent Infill | Deposition Speed |
|---|---|---|---|---|
| 270°C | 90°C | 0.254 mm | 100% | 250 mm/sec |

Encasing SR-30 support material was used to (i) provide necessary support for all print orientations, (ii) for dimensional accuracy of the test specimens, and (iii) to ensure a smooth surface finish, as the parts were printed with the automatic border generated by the slicing software. After printing, the SR-30 support material was dissolved away in an alkaline detergent bath‡ maintained at 85°C for a duration of 10 hours. Following this, the specimens were thoroughly

‡ Waterworks™ Soluble Support Concentrate P400SC at a concentration of 950g/42L.

rinsed with cold, distilled water and dried, preparing them for subsequent mechanical testing.

### 3.6. Produced Specimens

Figure 12 provides detailed visualizations of the 75° tensile specimen as prepared and printed using the Insight slicing software and the Stratasys F373 printer. In Figure 12a), the orthographic projection of the specimen is displayed, while Figure 12c) presents the front view. Each red line indicates an individual layer in the 3D printing. Figure 12b) and d) introduce the same views of the printed specimen when sliced for printing, including the encasing SR-30 support structure. Finally, Figure 12e) shows the completed printed specimen after the SR-30 support structure was dissolved, revealing the final form of the tensile specimen.

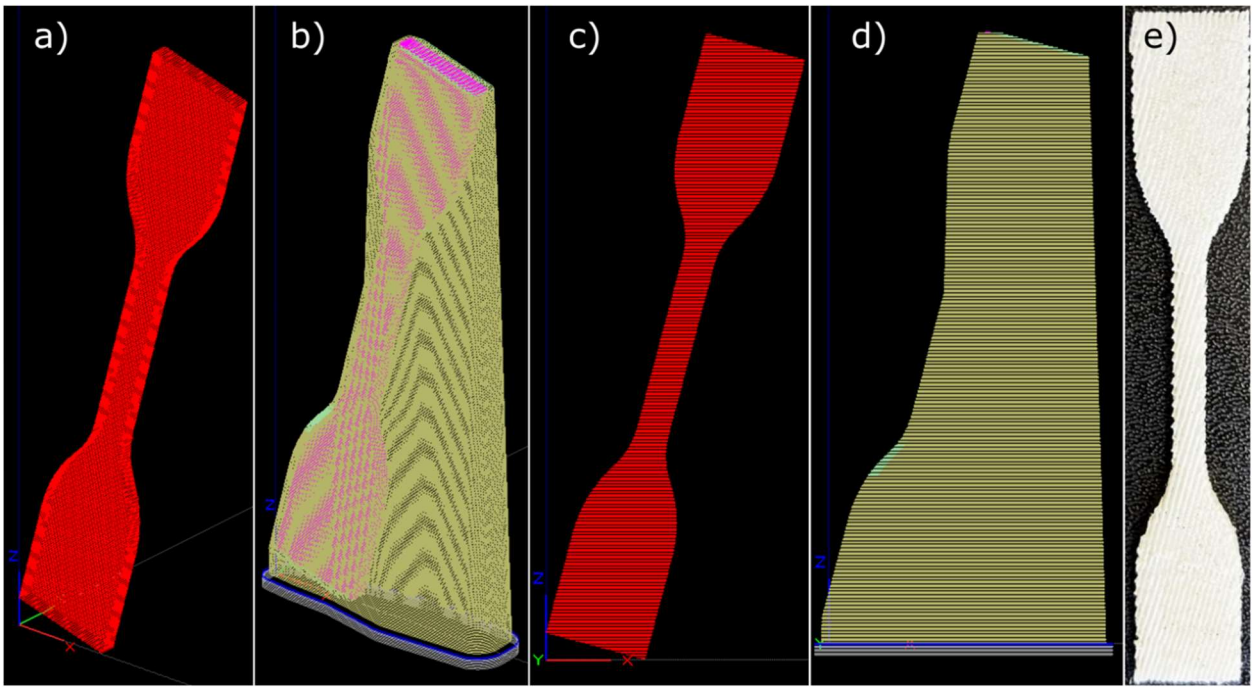


Figure 12 a) Orthographic projection of a sliced CAD file of a 75° tensile specimen; b) Same 75° specimen, with generated encasing SR-30 support; c) Front view; d) Front view with SR-30 support; e) The printed specimen after dissolution of the SR-30 support.

## 3.7. Specimens for Micro-Computed Tomography

The specimens were produced using the same method as the tensile and compression samples, with dimensions of 50 mm by 6 mm by 3.2 mm. Images of an FDM-produced micro-CT specimen of 0º print orientation can be seen in Figure 13. They were designed to mimic the testing region of the ASTM D369-IV tensile samples (as seen in Figure 6) but with a reduced length to accommodate the chamber of microtomography scanner.

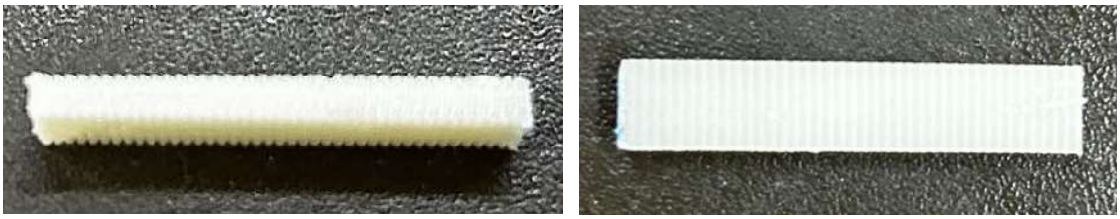

Figure 13 Micro-CT specimens.

# Chapter 4 Experimental Setup

## 4.1. Tensile Testing

Uniaxial tensile testing was performed as per ASTM D638. Five samples were tested for each print orientation. Testing was conducted with an MTS Criterion™ High Peak Force Universal Mechanical Tester (Model# C43-304)§, equipped with a 30 kN load cell (model number LPS.304 D)** (Figure 14, Figure 15). The MTS C43 had a resolution of 0.000049 mm. The strain was measured with an MTS LX 500 High Resolution Laser Extensometer††, with a resolution of 0.001 mm (Figure 14). Data collection was conducted at a frequency of 10 Hz. Figure 16 shows the tensile test setup with a specimen in the material testing machine. Figure 17 shows a schematic setup of tensile testing, compression testing, and laser strain data acquisition. The tensile test was conducted with a constant crosshead motion rate of 5mm/min, as specified by ASTM D638-IV procedure, until interlayer fracture occurred (Figure 18).

§ Serial number: 05000758.
** Serial number: 900939.
†† Serial number: 14101302.


Figure 14 From left to right: LX 500 High Resolution Laser Extensometer [112]; MTS Criterion™ High Peak Force Universal Mechanical Tester [113], in compression mode.


Figure 15 The 30 kN Load Cell used during tensile and compressive testing.

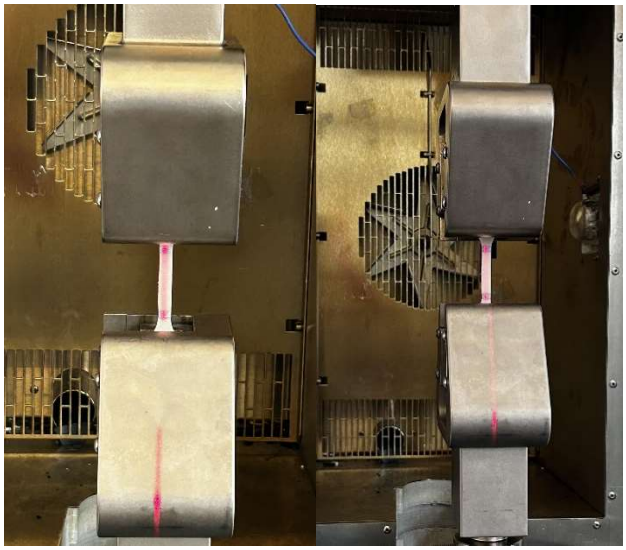

Figure 16 MTS C43 employed in tensile mode with a specimen and laser extensometer engaged.

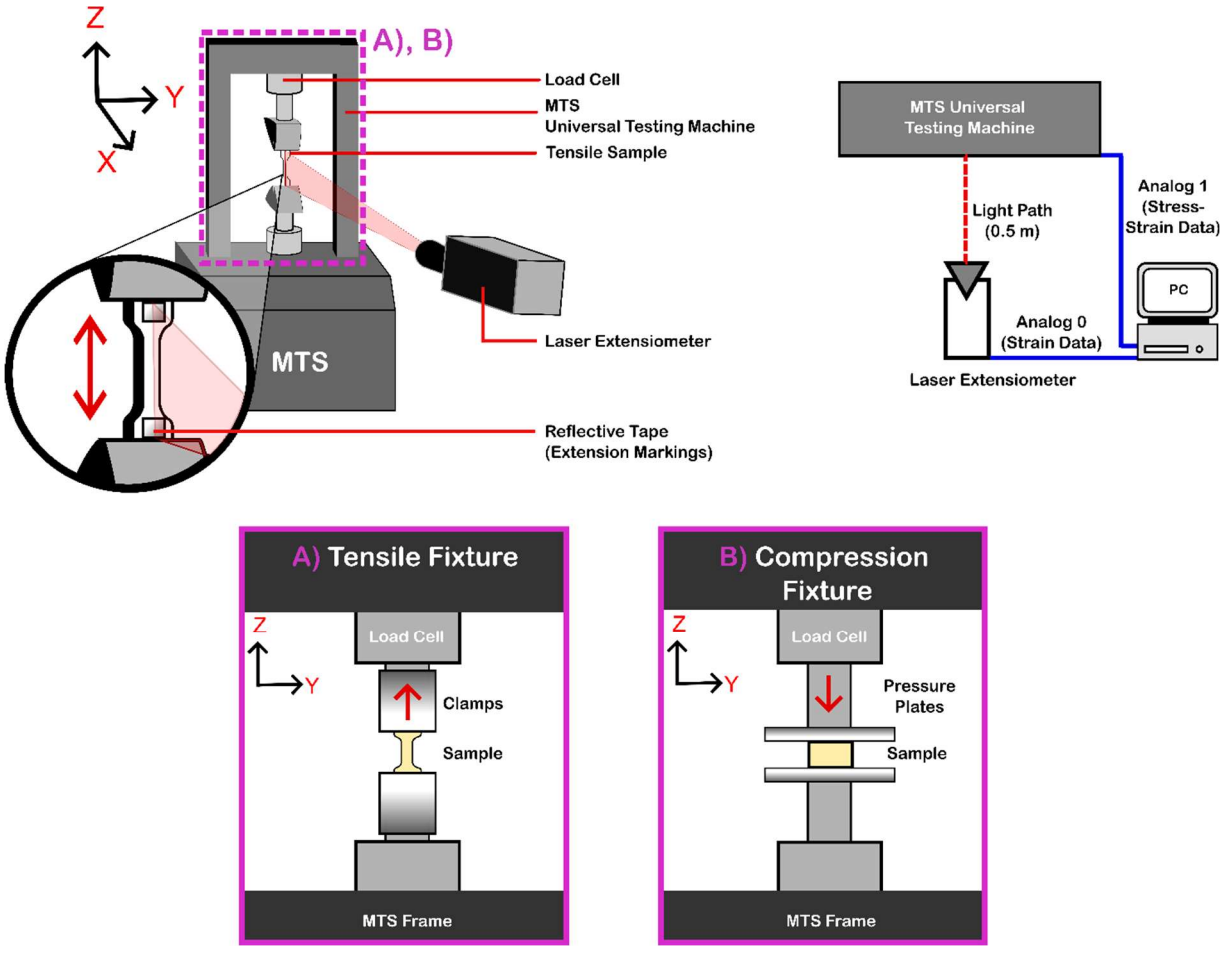


Figure 17 A) Tensile and B) Compression Testing Setup.

Figure 18 Five tensile specimens with 45° print orientation after fracture.

The tensile test data for the 60° and 75° specimens exhibited anomalous fluctuations in strain, as recorded by the LX 500 laser extensometer. These fluctuations appeared as random, discrete negative slips in strain, with no discernible pattern, even as the applied load consistently increased. While a similar error was present in the 45° specimen, the error magnitude was very small, and its data remained usable, unlike the extreme instability seen in the 60° and 75° specimens. Figure 19 illustrates the raw strain data, recorded by the laser extensometer, plotted against the stress data from the MTS crosshead.

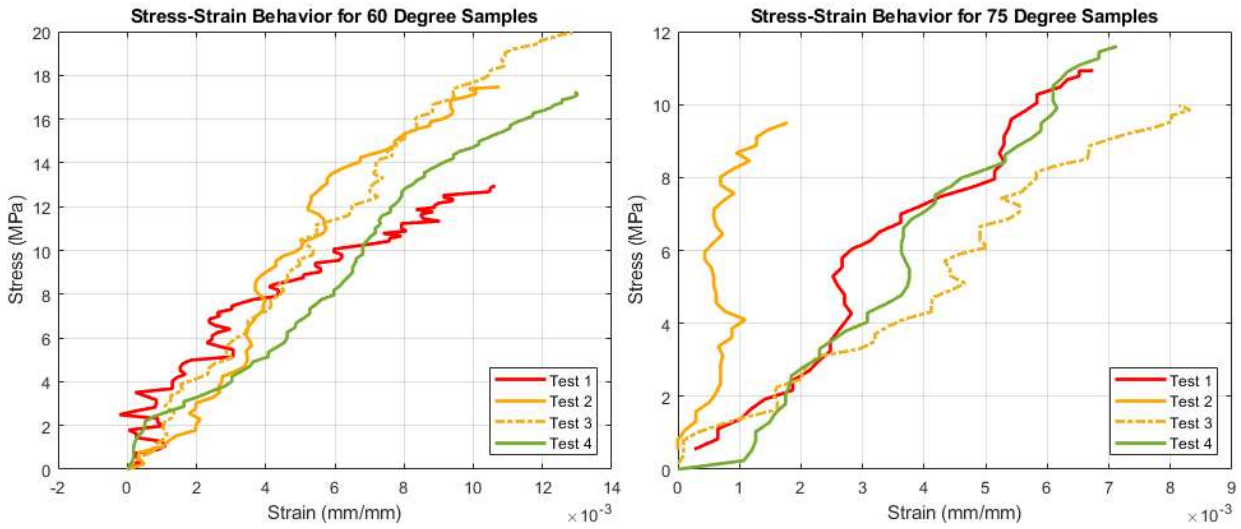


Figure 19 Raw data for 60° and 75° specimens, as recorded from the laser extensometer.

The source of these fluctuations was traced to slippage of the reflective tape used for laser calibration. The mechanism for the slippage is described in the following steps:

1) Tensile loading is applied, resulting in elongation of the material in the testing region.
2) As the strain increases, failure and shear occur at the layer interface.
3) The shearing of the layers causes very small rotations of the reflective tape.
4) One end of the tape is brought to a lower position. The laser extensometer reads a discrete, negative jump in strain.
5) As tensile strain increases, layer slippage occurs again, resulting in more tape rotation and discrete negative readings.

Figure 20 highlights this tape slippage effect. The schematic is not to scale, but amplified, as actual rotations of the tape are microscopic and not visible to the human eye.

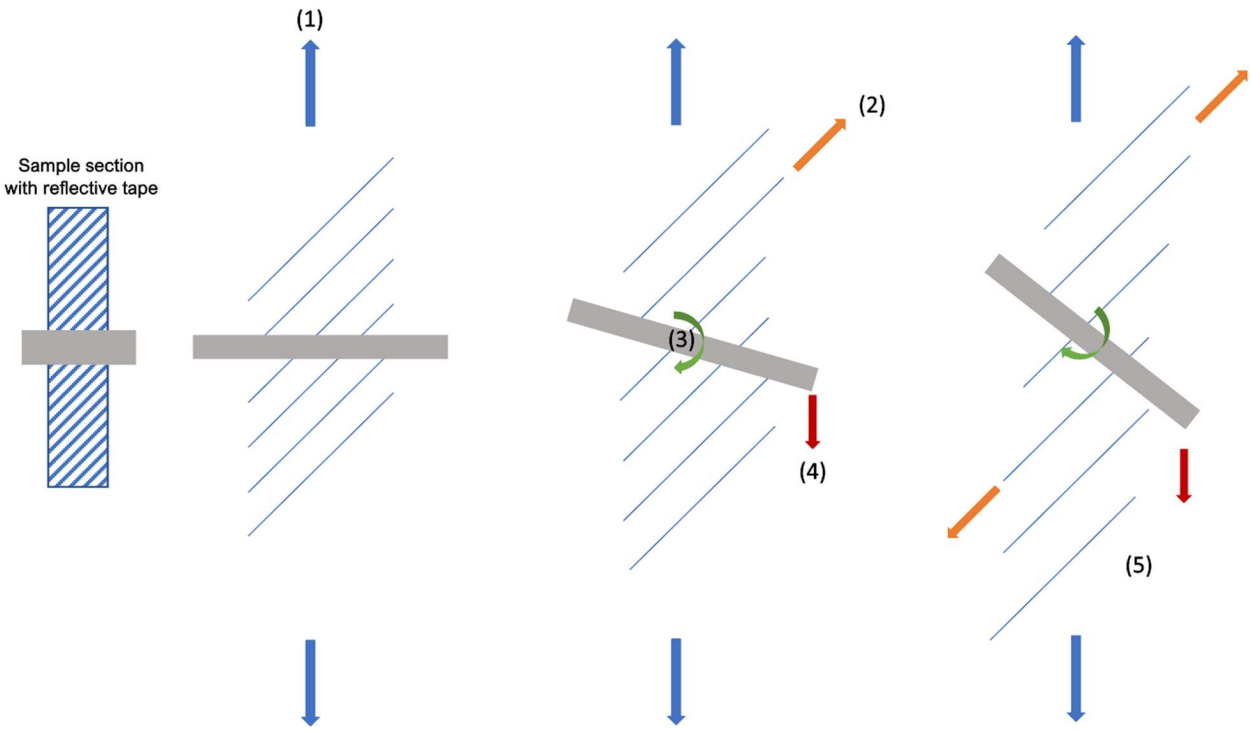


Figure 20 Schematic showing tape rotation during testing of the 60° and 75° specimens.

The phenomenon is more pronounced in the higher-angle samples due to greater vertical shear at these angles. Notably, it is not present for the 90° specimens as the interlayer is perpendicular to the tape and shearing does not result in tape rotation. It is also not present in the compression specimens. Subsequently, strain for the 60° and 75° specimens was recalculated using crosshead motion measurements. Figure 21 compares laser extensometer readings with crosshead data.

While using crosshead displacement data for strain measurement is not ideal, the laser extensometer data in this case had excessive noise, making it unsuitable for analysis. Unlike a laser extensometer, the MTS C43 calculates overall displacement without isolating the gauge length. To mitigate this issue, crosshead strain was adjusted by dividing the crosshead displacement by

the gauge length to account for the testing region length. Additionally, resolution was not an issue, as the MTS C43 has a higher resolution (0.000049 mm) compared to the LX500 (0.001 mm).

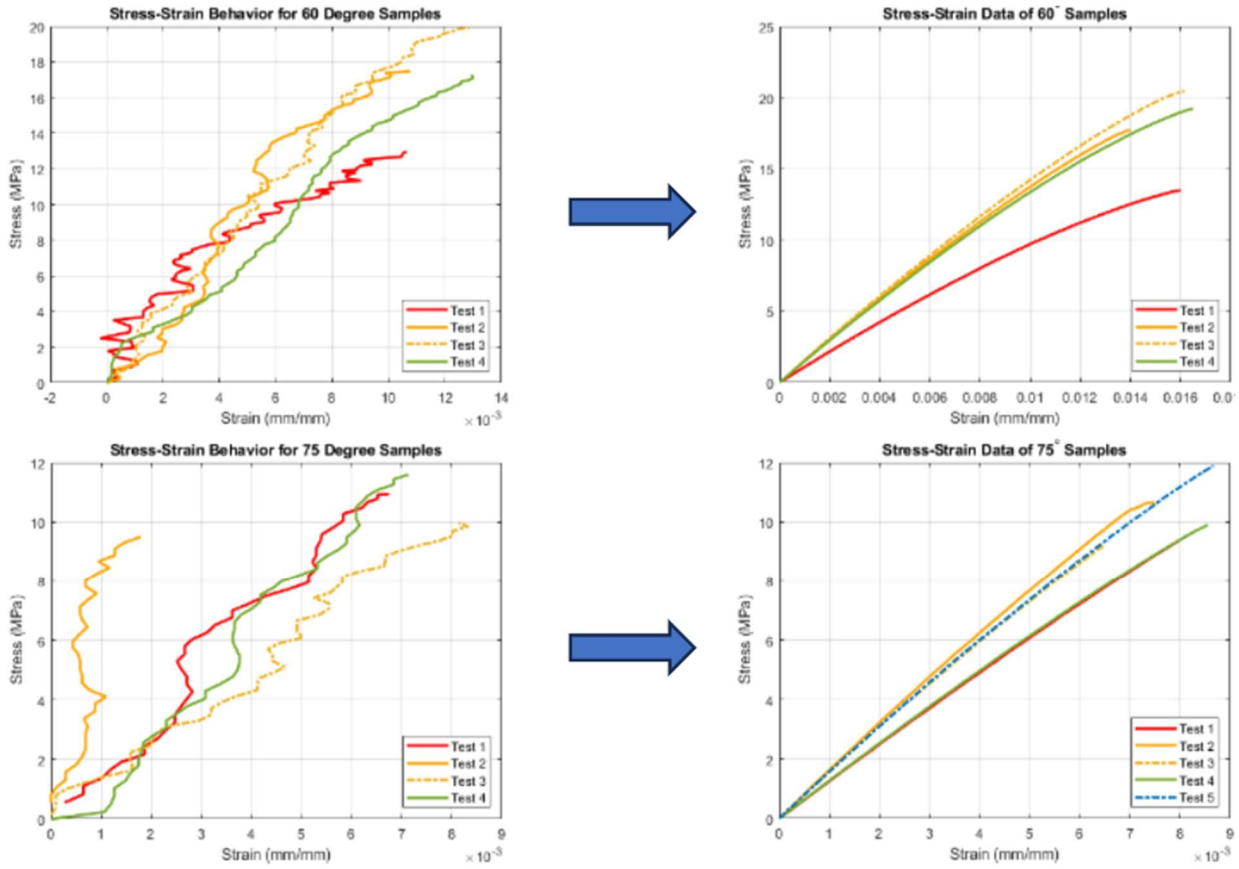


Figure 21 Comparison of strain data from laser extensometer and MTS crosshead data.

## 4.2. Compression Testing

Uniaxial compression testing was conducted on an MTS High Peak Force Universal Mechanical Tester (Criterion Model 43), with a 30 kN load cell. All strain data was measured with the LX 500 laser extensometer, using the compression plates as a reference. The strain values were then normalized to the dimensions of the testing specimen. Data was collected at a frequency of

10 Hz, with a constant crosshead motion rate of 1.3 mm/min. As see in Figure 22, the tests were terminated when compressive failure occurred, which was always by the means of axial splitting. This failure mode is visually identifiable by the formation of longitudinal cracks parallel to the loading direction. The MTS C43 machine was set to terminate the test upon detecting axial splitting. The occurrence of axial splitting leads to a sharp decrease in the specimen's load-bearing capacity, accompanied by a sudden drop in the applied force. The machine's sensors detected these abrupt changes and triggered an automatic test termination.

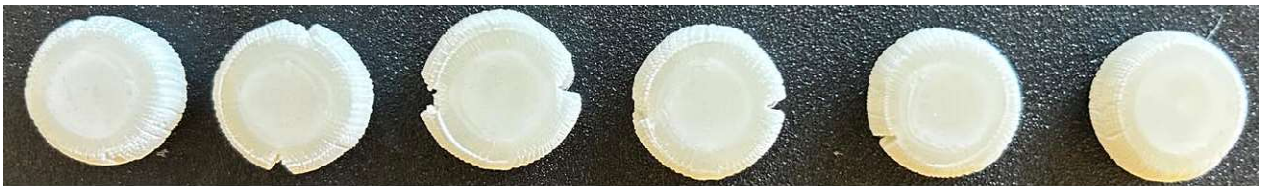

Figure 22 Six (6) 90° compression specimens after testing, showing failure via axial splitting.

## 4.3. Microtomography (Micro-CT)

The Microtomography (Micro-CT) testing process conducted in this study involved a detailed qualitative analysis of the specimens using advanced imaging techniques. The Bruker Skyscan 1272 micro-CT system was employed to capture high-resolution images, enabling an in-depth examination of the internal structures of the specimens.

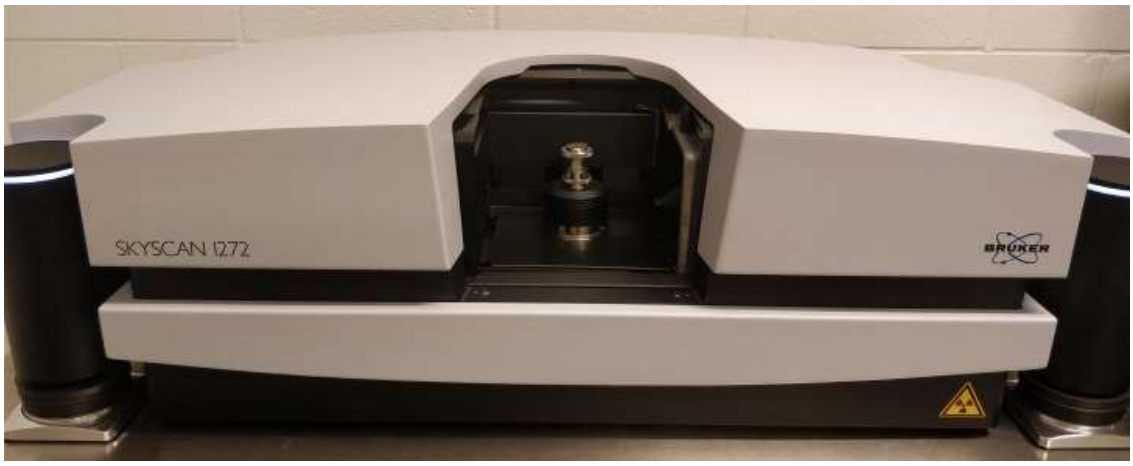


Figure 23 The Bruker Skyscan 1272 (CMOS Edition) micro-CT system, a high-resolution x-ray microscope [114].

The imaging process was carried out using a 42 kV X-ray source with a current of 176 milliamps. To enhance the image quality and reduce artifacts, a 0.25 mm aluminum filter was applied. The spatial resolution was set to 4.0 micrometers, allowing for the capture of fine structural details within the specimens. The specimens were imaged in a full 360-degree rotation, with a rotational increment of 0.1 degrees between each image, ensuring comprehensive coverage and minimizing any gaps in the data. For each rotational position, three images were averaged to reduce noise and enhance the clarity of the final dataset. The collected images were then reconstructed into a 4904x3280 pixel array, providing a high-resolution three-dimensional representation of the specimens. This meticulous process allowed for a thorough qualitative assessment of the internal features, aiding in the analysis of the material's structural integrity and performance characteristics.

# Chapter 5 Experimental Results and Discussion

## 5.1. Brief of Retrieved Data

This chapter presents the results of the testing conducted on the specimens. For each print orientation, five samples were tested in both tensile and compressive modes. After data normalization, the individual stress-strain curves were plotted for each sample, and mechanical properties such as Young's Modulus, Ultimate Tensile Strength, 0.2% offset Yield Strength, and stress and strain at fracture were calculated. To further analyze the data, a mean stress-strain curve was generated for each sample set. This was achieved by defining a common strain scale, represented as a linearly spaced vector between the minimum and maximum strain values observed in the dataset. The stress values from each individual test were then averaged for each unique strain and then interpolated onto this common strain scale. The common strain scale is described as:

$$common\ strain = \epsilon_{min} + k\Delta\epsilon\ for\ k = 0, 1, 2, \ldots, N-1 \quad (4)$$

where $\epsilon_{min}$ is the minimum strain value across all tests, $N$ is the number of points in the common strain scale (in the case, 1000), and $\Delta\epsilon$ is the strain interval, calculated as:

$$\Delta\epsilon = \frac{\epsilon_{max} - \epsilon_{min}}{N-1} \quad (5)$$

In addition to mechanical testing, dimensional data was collected by measuring the specimens using a caliper. These measurements were plotted according to printing orientation to assess any dimensional variations.

Micro-CT images were obtained for qualitative analysis. The images revealed evidence of

insufficient interlayer bonding and raster interlayer bonding, providing insights into potential structural weaknesses in the printed specimens. Their findings contribute to a comprehensive understanding of the material behavior under tensile and compressive loading.

## 5.2. Tensile Testing Results

Specimens with a 0º printing orientation exhibited stress-strain curves and failure behaviors typical of a ductile high-temperature thermoplastic, characterized by a defined linear-elastic region, peak stress at the yield point, an extended plastic region with strain softening, and eventual fracture. As the printing orientation angle increased, the plastic region progressively diminished, with specimens oriented at 60º and beyond showing virtually no plastic deformation before failure.

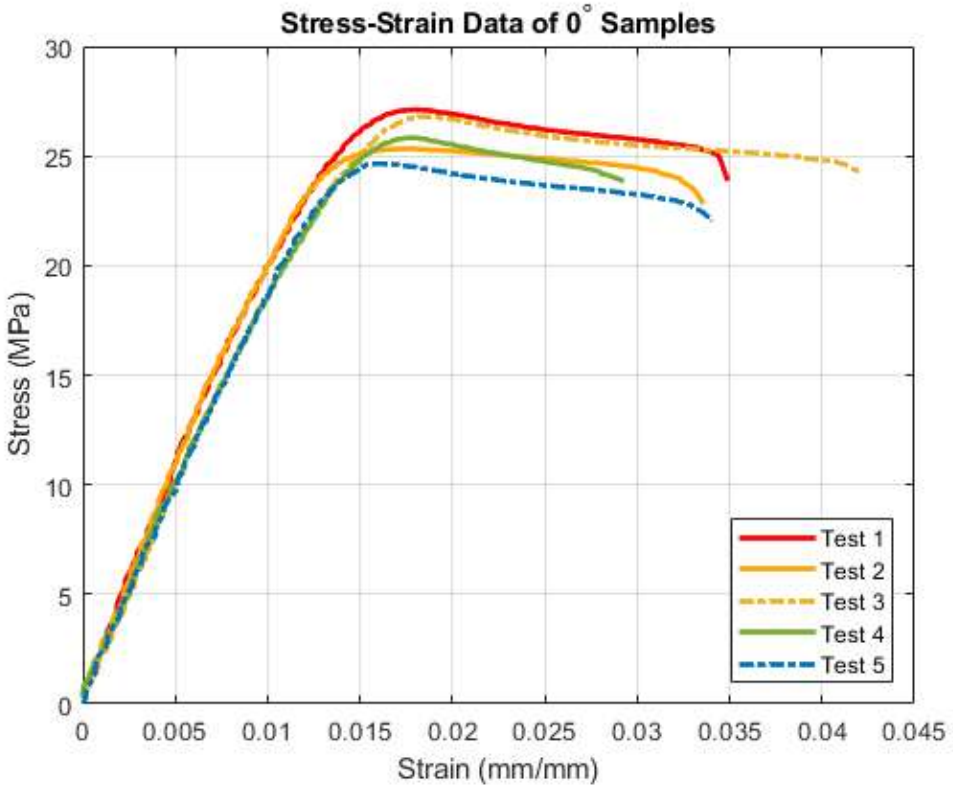


Figure 24 Individual stress-strain curves for all 0º tensile specimens.

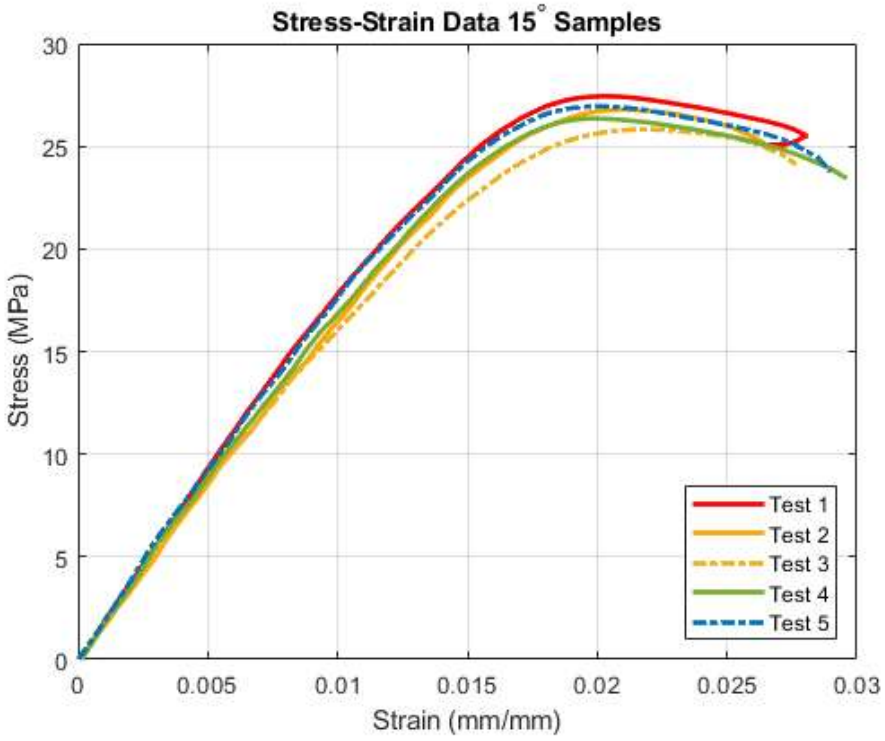


Figure 25 Individual stress-strain curves for all 15º tensile specimens.

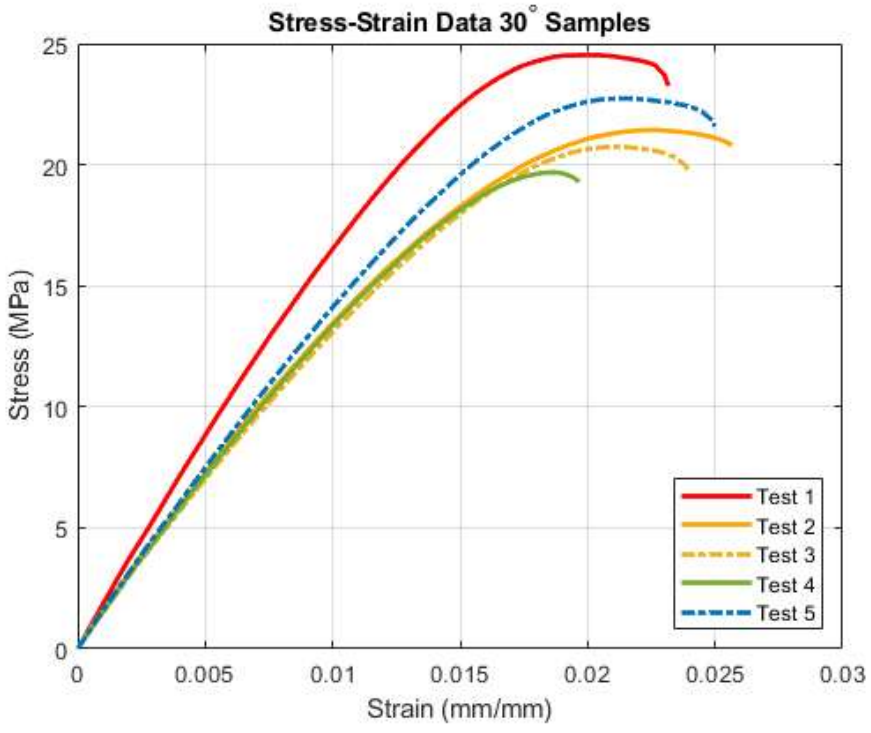


Figure 26 Individual stress-strain curves for all 30º tensile specimens.

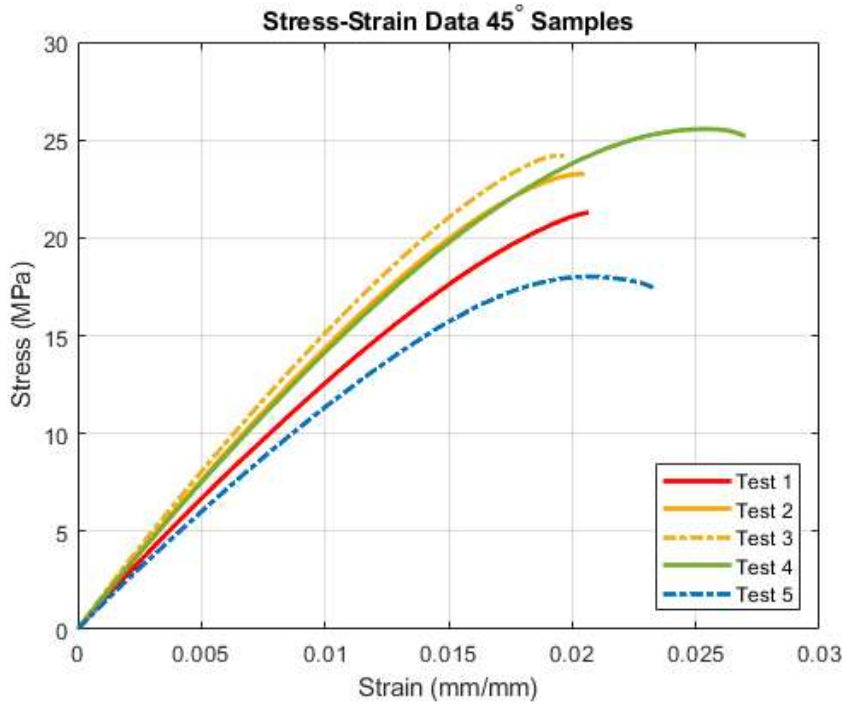


Figure 27 Individual stress-strain curves for all 45º tensile specimens.

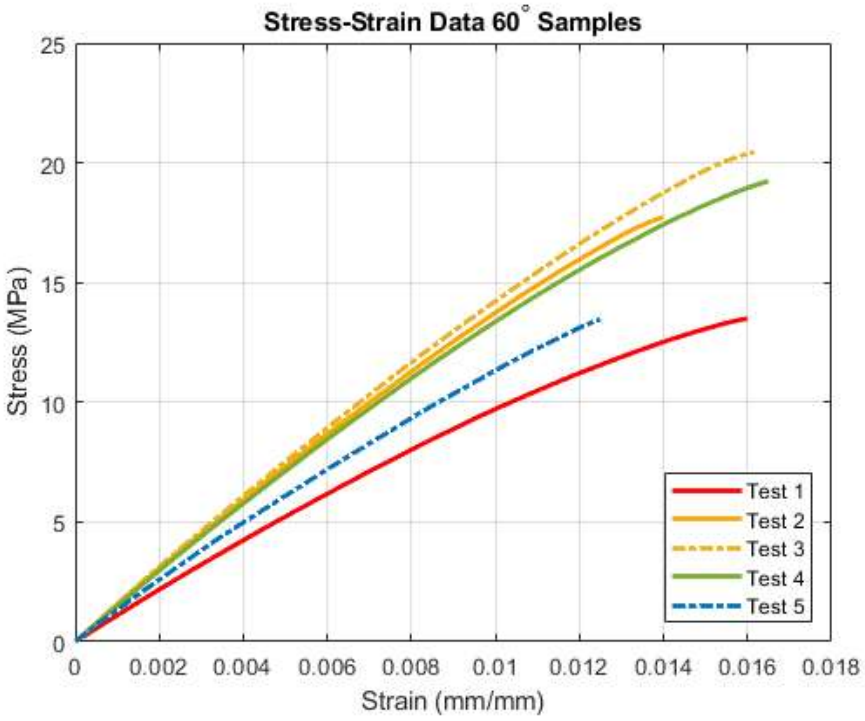


Figure 28 Individual stress-strain curves for all 60º tensile specimens.

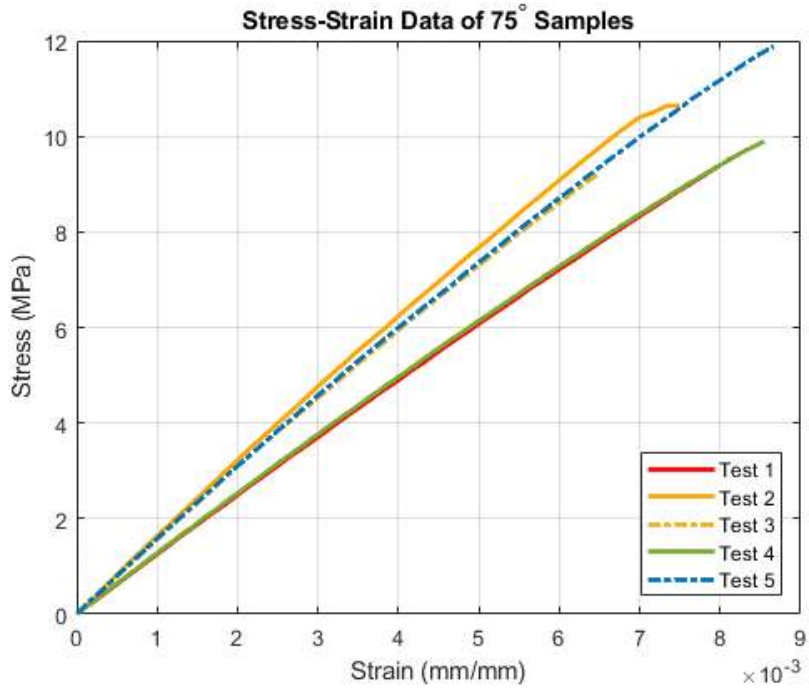


Figure 29 Individual stress-strain curves for all 75º tensile specimens.

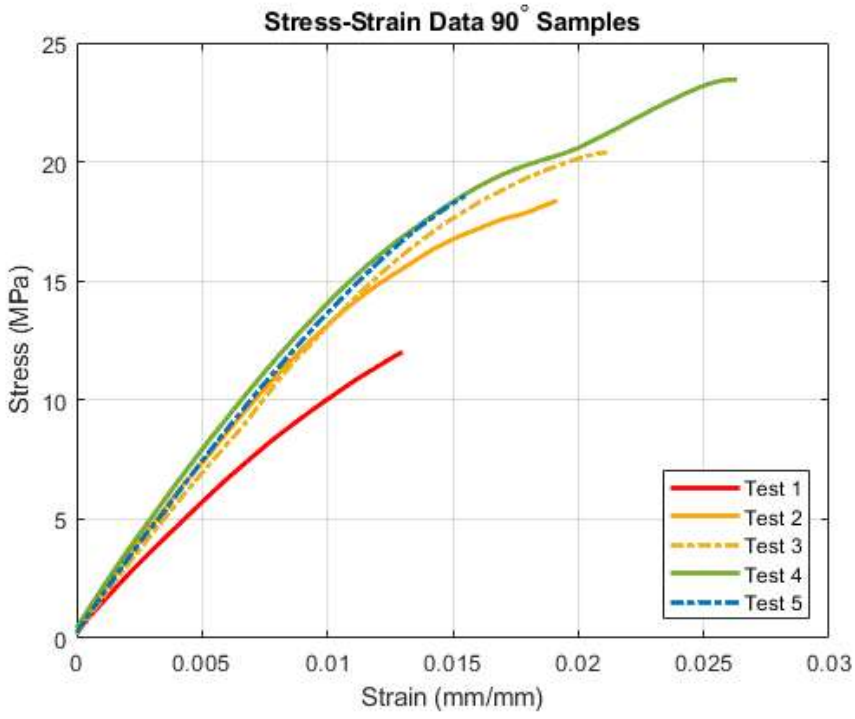


Figure 30 Individual stress-strain curves for all 90º tensile specimens.

Figure 31 to Figure 37 details the average stress-strain curves, with dashed lines representing upper and lower bounds in standard deviation. Figure 38a) displays the average stress-strain curves for all specimens, ranging from 0º to 90º, plotted on the common strain scale.

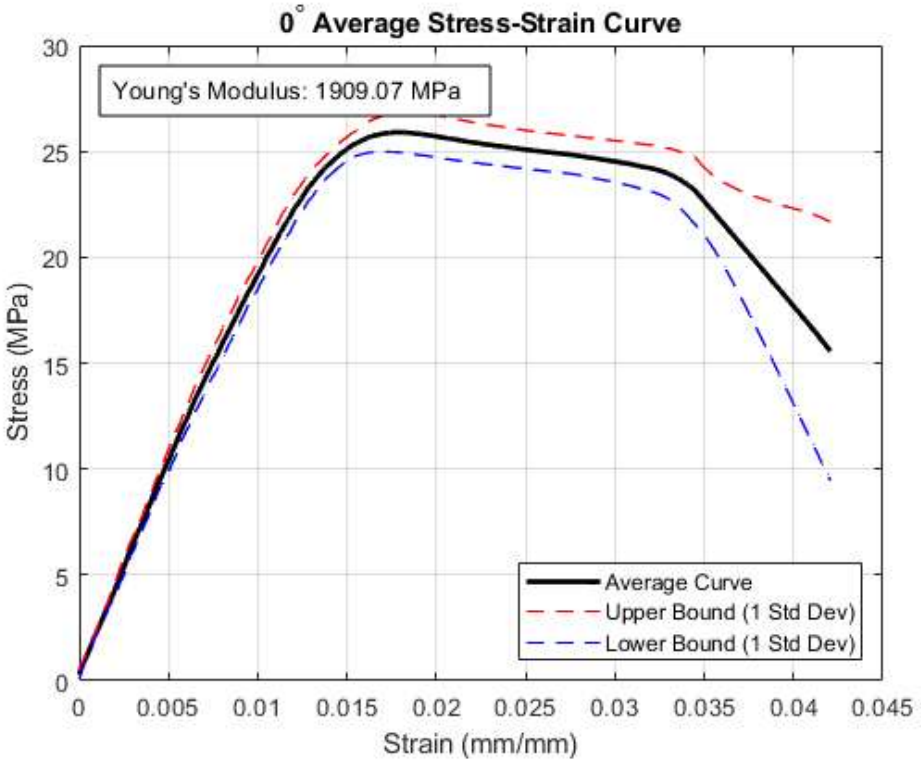


Figure 31 Average Stress Strain Curve of 0º Specimens.

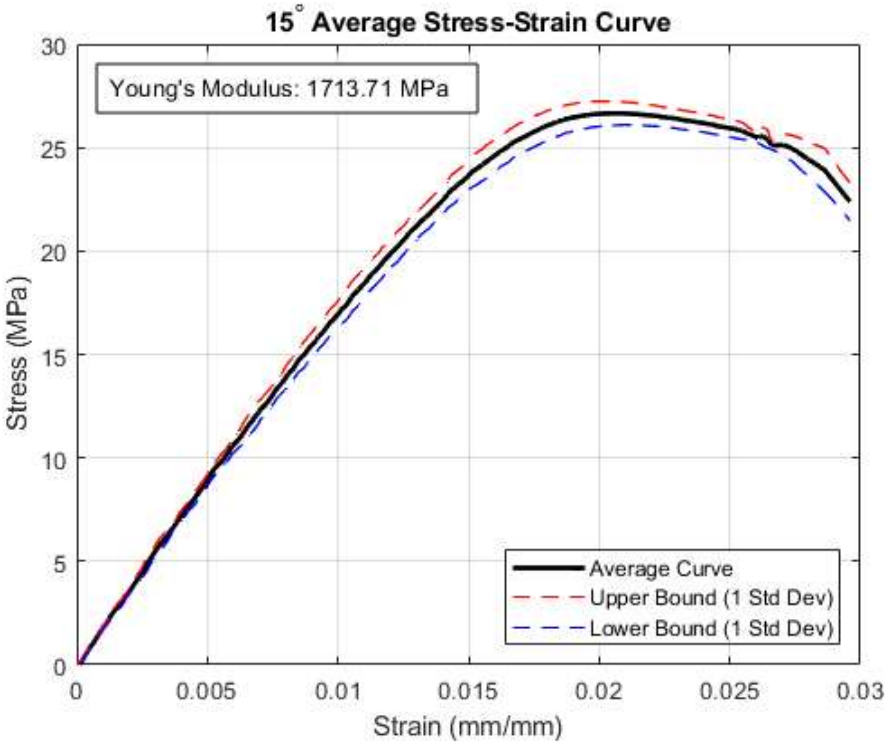


Figure 32 Average Stress-Strain Curve of 15º Specimens.

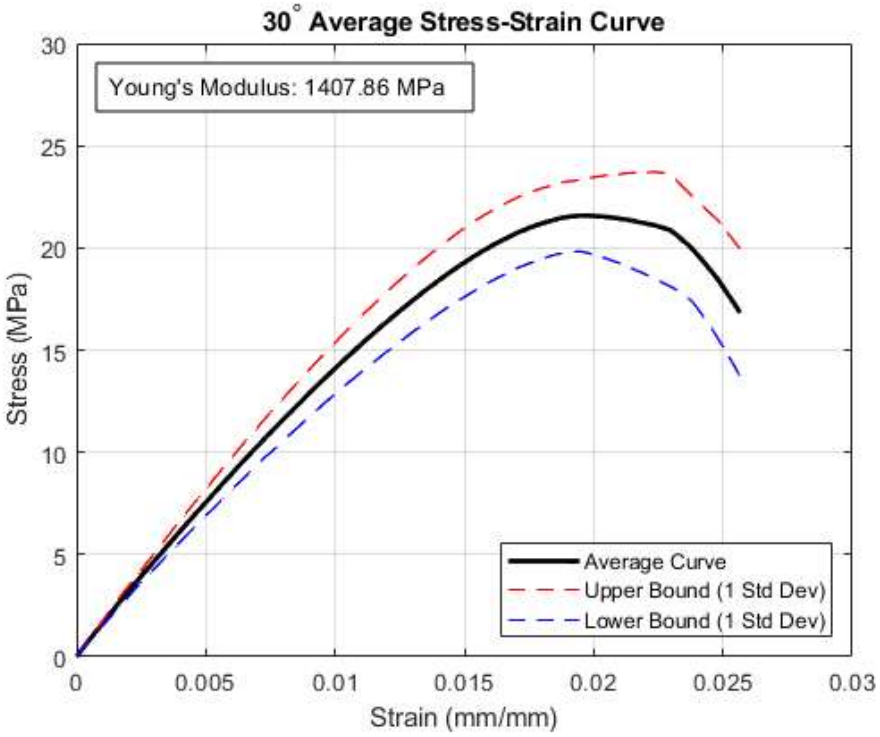


Figure 33 Average Stress-Strain Curve of 30º Specimens.

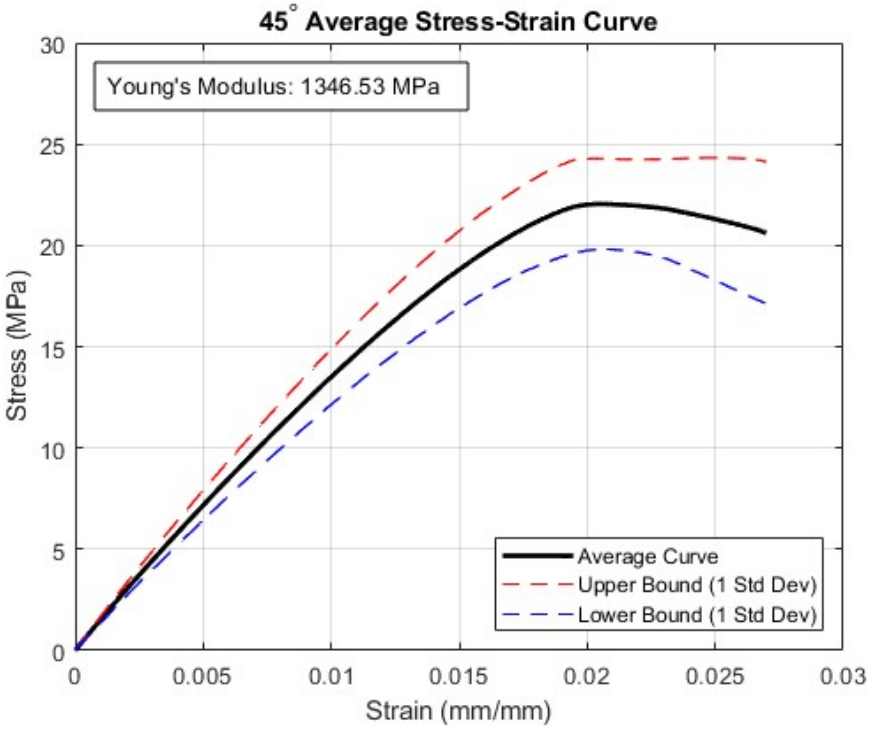


Figure 34 Average Stress-Strain Curve of 45º Specimens.

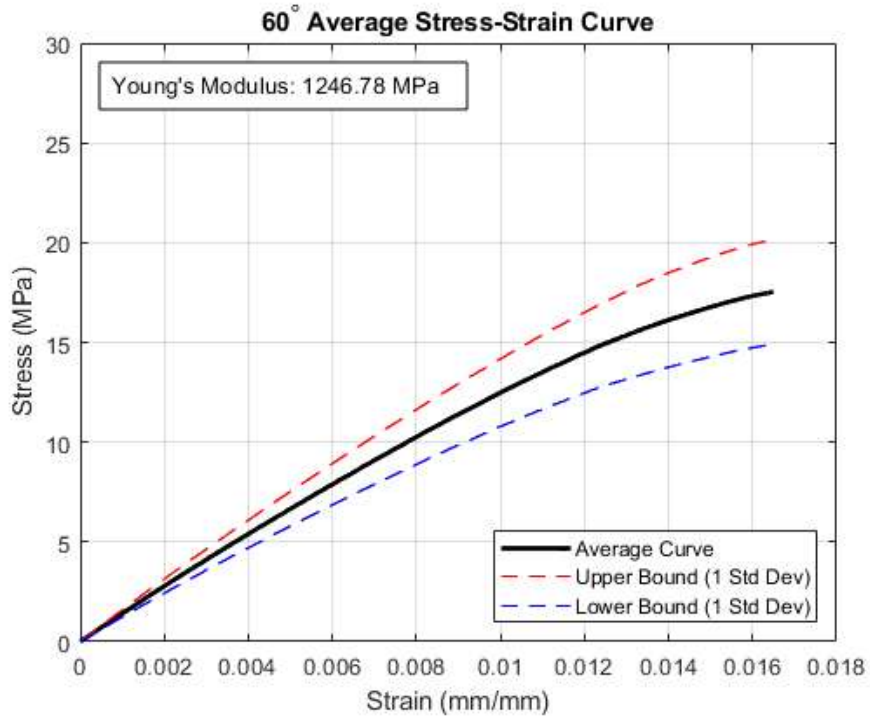


Figure 35 Average Stress-Strain Curve of 60º Specimens.

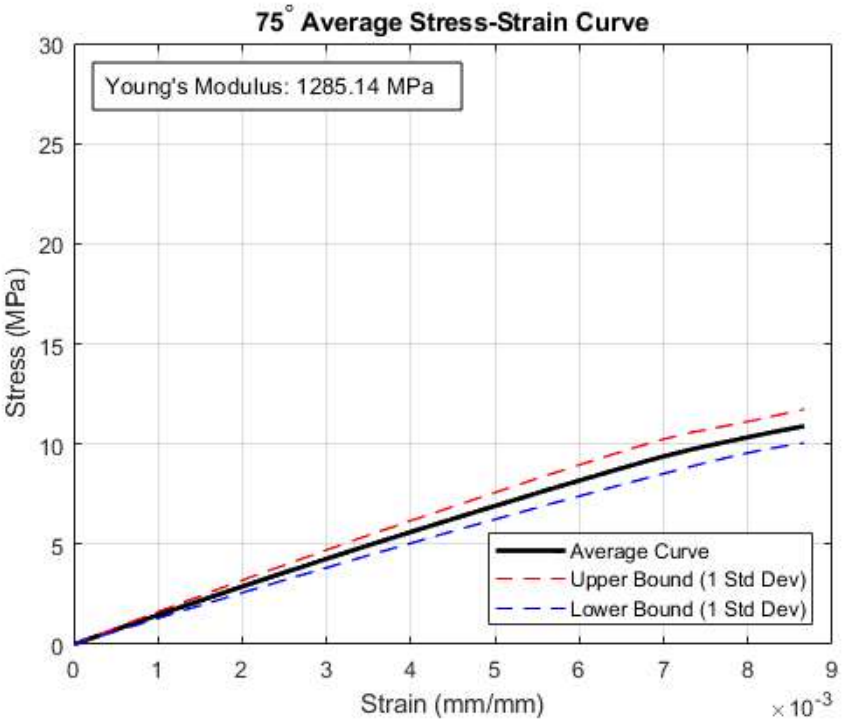


Figure 36 Average Stress-Strain Curve of 75º Specimens.

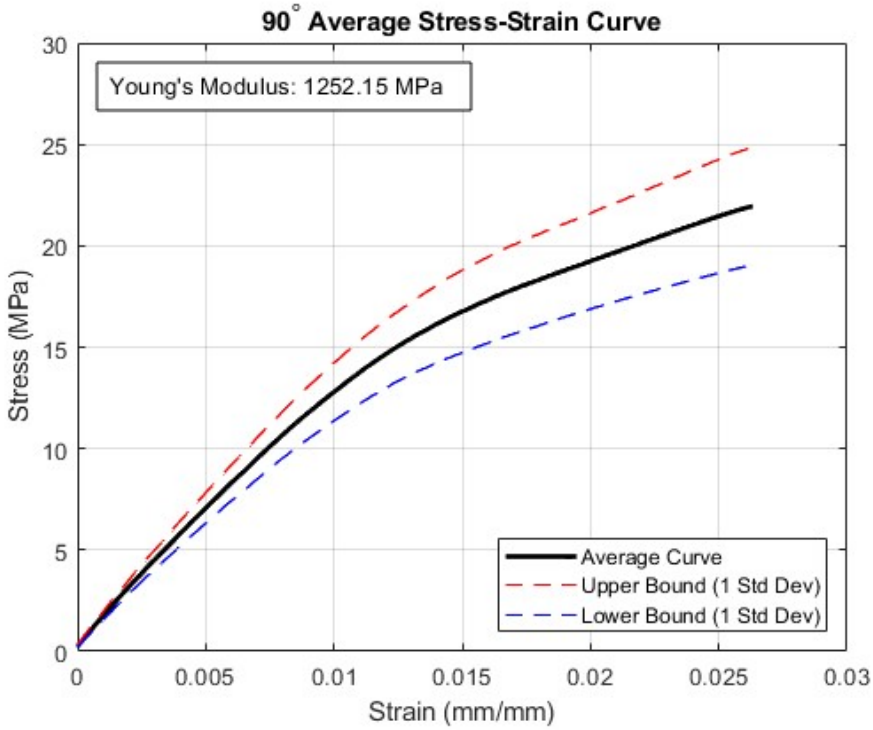


Figure 37 Average Stress-Strain Curve of 90º Specimens.

### 5.2.1. Discussion of Tensile Testing Results

The data analysis focused on ultimate tensile stress (UTS), stress at fracture, strain at fracture, Young's Modulus, and yield strength. For sample sets that exhibited a plastic region (0° to 45° specimens), yield strength was calculated using the 0.2% offset yield method. Stress and strain at fracture are measured at the point where the specimen breaks. The 0.2% method was used as the tested material exhibits a gradual transition to non-linear behavior without a distinct yield point. By using this method, it ensures that a 0.2% plastic deformation has occurred, providing a reliable estimate of the material's yield strength.

The UTS was the highest at 0° (25.94 MPa) and the lowest at 75° (10.27 MPa), showing a 60.4% decrease as the print orientation increased, with an overall trend of decreasing UTS from 0° to 75°. Similarly, fracture stress was the highest at 0° (23.37 MPa) and the lowest at 75° (10.27 MPa), with a 56.1% decrease. Fracture strain also decreased sharply, with a 77.3% reduction from 0° (0.0348 mm/mm) to 75° (0.00791 mm/mm), indicating reduced ductility at higher angles. Young's Modulus decreased as well, from 1865.96 MPa at 0° to a low of 1223.85 MPa at 60°, reflecting a 34.4% reduction and showing that the material became less stiff at higher angles. Yield strength followed a similar trend, decreasing from 25.87 MPa at 0° to 21.54 MPa at 45°, with a 16.8% drop. Overall, as the print orientation increased from 0° to 75°, mechanical properties such as strength, ductility, and stiffness generally decreased. In terms of fractional gravity, strength, ductility, and stiffness generally decreased in tensile mode as gravitational force increased from 0*g* to 0.966*g* on the raster interlayer. However, the 90° samples showed a notable increase in UTS (80.8%), strain at fracture (140.6%), and stress at fracture (80.7%) compared to the 75° samples, although these increases did not exceed the values observed at orientations below 45°. The most significant changes occurred around the 75° orientation, where UTS, fracture stress, and fracture

strain exhibited pronounced decreases. This analysis highlights that the level of gravitational force acting upon the raster layer during layer deposition significantly impacts the mechanical properties of the material, with properties being strongest at 0° (0$g$) and weakest at 75° to 90° (0.966$g$ to 1$g$). For visual aid, boxplots of UTS, fracture stress, fracture strain, Young's Modulus, and yield strength as they vary with printing orientation can be seen in Figure 38b) to 18f) to show the data variation ranges. The average values for mechanical properties of tensile testing, in tabulated numerical form, can be found in Table 6.

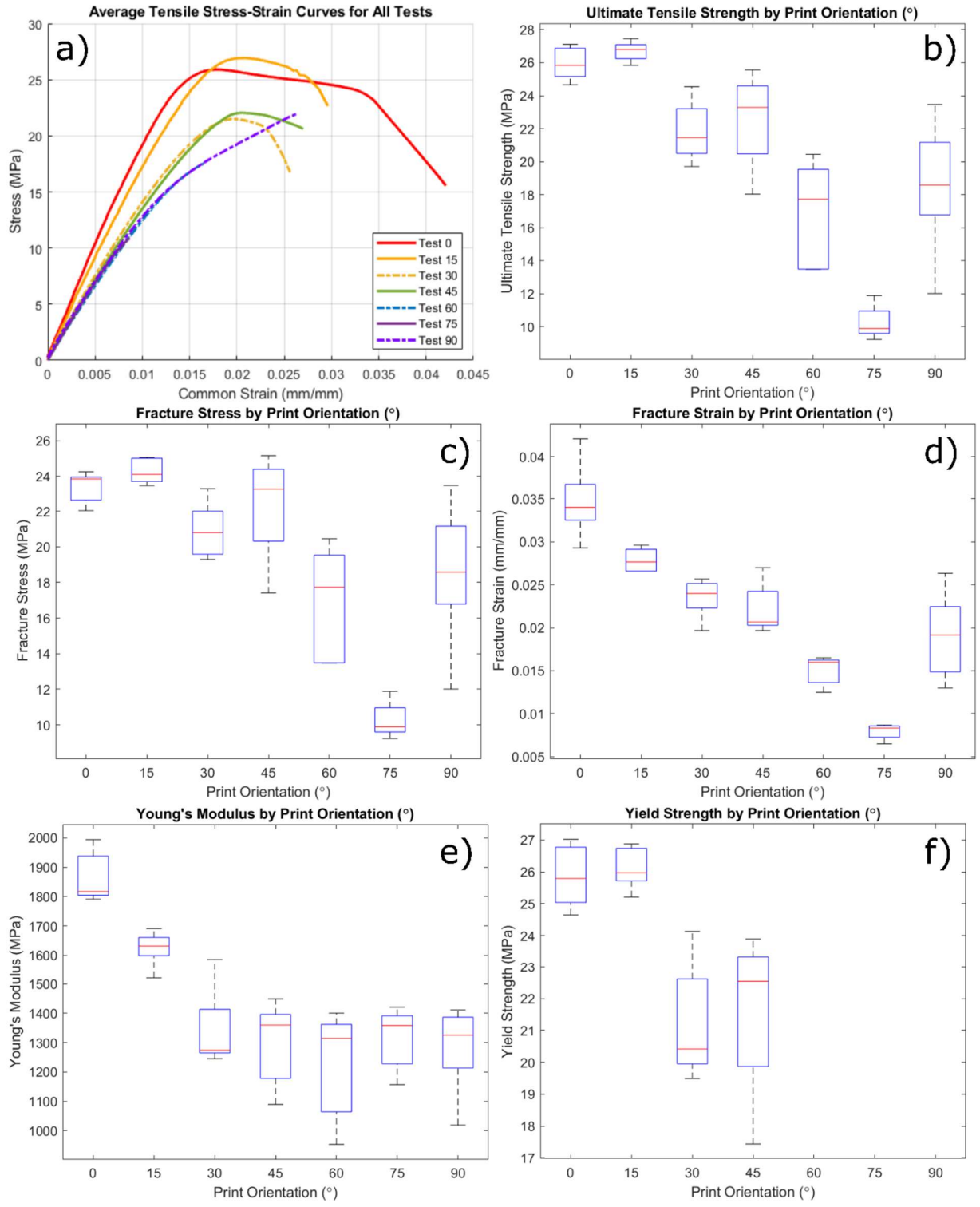


Figure 38 a) Plot of all average stress-strain curves across a common strain scale; and b)-f) Boxplots showing the variation in b) Ultimate Tensile Strength, c) Fracture Stress, d) Fracture Strain, e) Young's Modulus, and f) Yield Strength by Print Orientation.

Table 6 Average Mechanical Properties of Tensile Testing.

| Print Orientation | UTS | Fracture Stress | Fracture Strain | Young's Modulus | Yield Strength |
|---|---|---|---|---|---|
| [º] | [MPa] | [MPa] | [mm/mm] | [MPa] | [MPa] |
| 0 | 25.94246 | 23.36489 | 0.034772 | 1865.96 | 25.8648 |
| 15 | 26.6832 | 24.27636 | 0.027883 | 1624 | 26.1278 |
| 30 | 21.84363 | 20.92227 | 0.023497 | 1346.42 | 21.2498 |
| 45 | 22.48379 | 22.25123 | 0.02223 | 1296.84 | 21.5392 |
| 60 | 16.87431 | 16.87431 | 0.015029 | 1223.852 | - |
| 75 | 10.27403 | 10.27403 | 0.007908 | 1313.86 | - |
| 90 | 18.56721 | 18.56265 | 0.019028 | 1282.46 | - |

A one-way ANOVA was conducted with UTS, fracture stress, fracture strain, Young's Modulus, and yield strength as dependent variables, using print orientation as the independent variable. Levene's Test was performed to assess the homogeneity of variances, and the results generally indicated that this assumption was met. However, UTS, fracture stress, and yield strength showed p-values are greater than or close to 0.05, suggesting some potential variability in variance homogeneity. To mitigate the risk of false positives, the Bonferroni correction was applied. The ANOVA results, supported by the Bonferroni-corrected p-values, confirm that printing orientation has a significant effect on all the measured mechanical properties.

Table 7 Original p-values, and p-values for Levene's Test and the Bonferroni Correction.

| Dependent Variable | p-values | | |
|---|---|---|---|
| | Original | Levene's Test | Bonferroni Corrected |
| UTS | $2.395 \times 10^{-10}$ | 0.057364 | $1.6765 \times 10^{-9}$ |
| Fracture Stress | $9.0355 \times 10^{-9}$ | 0.05854 | $6.3248 \times 10^{-8}$ |
| Fracture Strain | $2.5826 \times 10^{-12}$ | 0.14071 | $1.8078 \times 10^{-11}$ |

| | | | |
|---|---|---|---|
| Young's Modulus | $9.2034 \times 10^{-8}$ | 0.20612 | $6.4424 \times 10^{-7}$ |
| Yield Strength | $2.1342 \times 10^{-4}$ | 0.054596 | $1.494 \times 10^{-3}$ |

Table 7 presents the original, Levene's, and Bonferroni-corrected p-values, demonstrating that print orientation significantly influences UTS, fracture stress, fracture strain, Young's Modulus, and yield strength. The residuals plots (Figure 39) show random and pattern-free residuals, indicating that the assumptions of linearity and homoscedasticity are met.

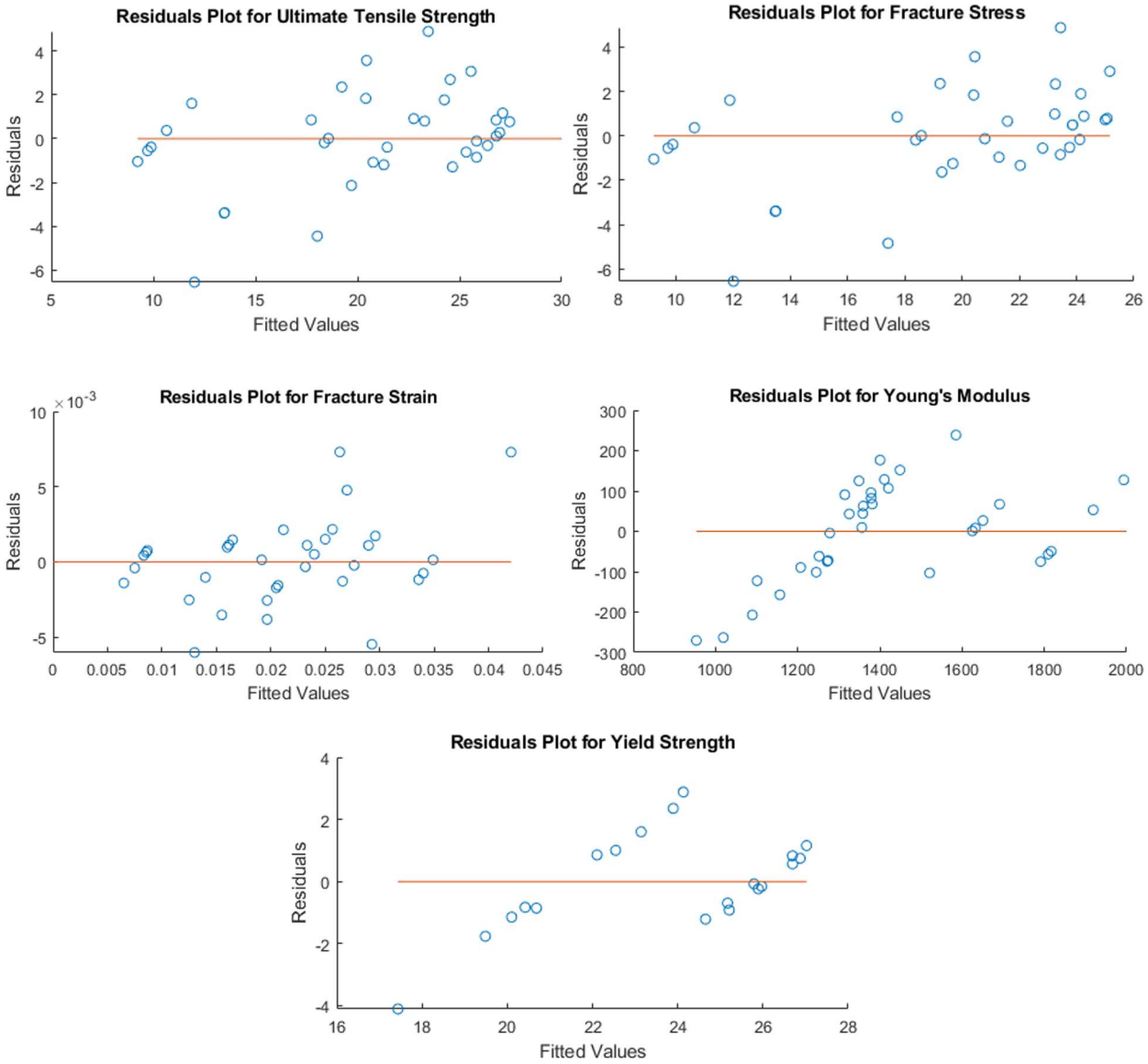


Figure 39 Residuals plots corresponding to the 1-way ANOVA for tensile properties.

### 5.2.2. Discussion of Tensile Testing Trends

The results from tensile testing suggest that as print orientation increases from 0° to 75°, there is a clear decline in mechanical properties. Specifically, UTS decreases by 60.4%, fracture stress by 56.1%, and fracture strain by 77.3%, indicating a significant reduction in ductility. Young's Modulus also declines by 34.4%, reflecting a decrease in material stiffness, and yield strength drops by 16.8%. Interestingly, at 90°, there is a notable recovery in UTS (80.8%), fracture strain (140.6%), and fracture stress (80.7%) compared to 75°, although these improvements do not reach the levels observed at orientations below 45°. From these findings, it can be concluded that the failure mode between 0° and 75° is due to failure at the raster interlayer, while 90° specimens fail at the regular interlayer. This explains the observed increase in mechanical properties at 90°. These results suggest that the raster interlayer bond weakens as printing orientation increases, likely due to the greater influence of gravity at higher printing orientations, which adversely affects bond strength. The discontinuity in UTS, fracture strain, and fracture stress data between 75° and 90° further implies that the raster and regular interlayer bonds exhibit different strengths at different gravity levels and should be assessed on separate scales.

## 5.3. Compression Testing Results

The compression curves of all samples can be divided into three distinct stages. Stage I consists of a linear elastic region characterized by rigid material behavior. Stage II is an elastic-plastic transition zone, followed by a plastic stress plateau where the material exhibits perfect plasticity. The elastic-plastic transition zone featured a local maximum in stress, and the onset of plasticity was observed as barrelling in the specimens. In Stage III, the material enters a plastic

densification region, again idealized as rigid. The samples experienced interlayer failure at peak densification, marking the end of the test and accounting for the absence of an unloading region.

Figure 40 to Figure 46 present the stress-strain curves for all tests in all testing rounds, while the average compression curves may be found in Figure 47 to Figure 53.

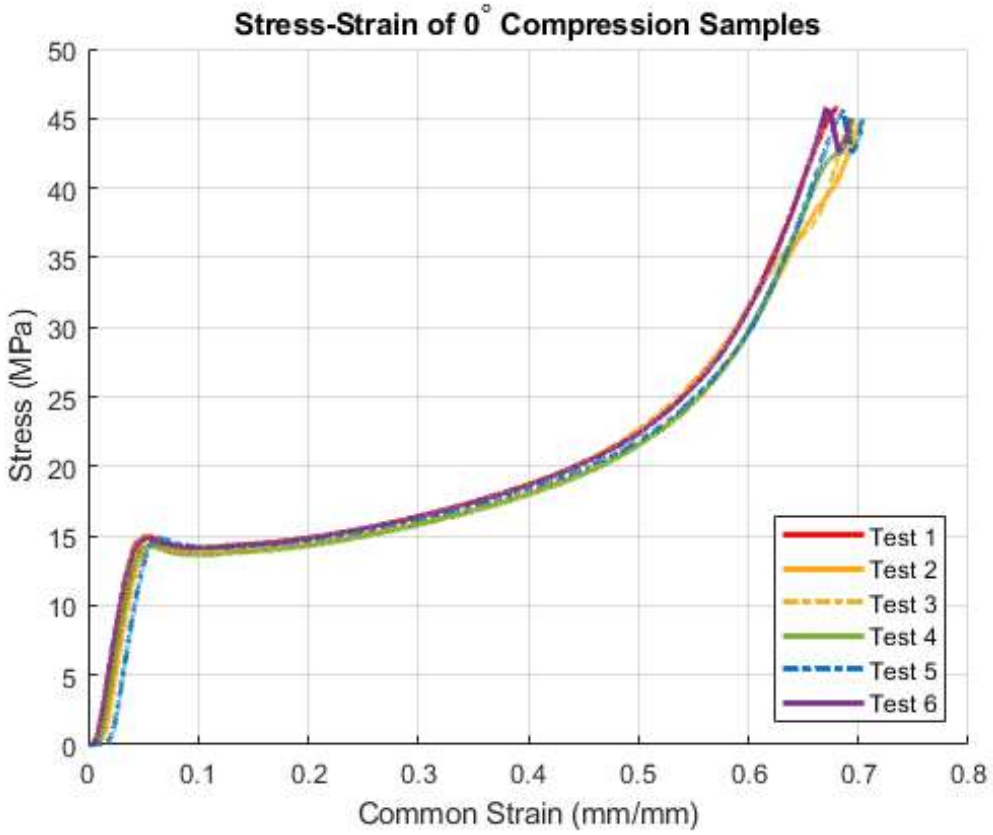

Figure 40 Individual stress-strain curves for all 0º compression specimens.

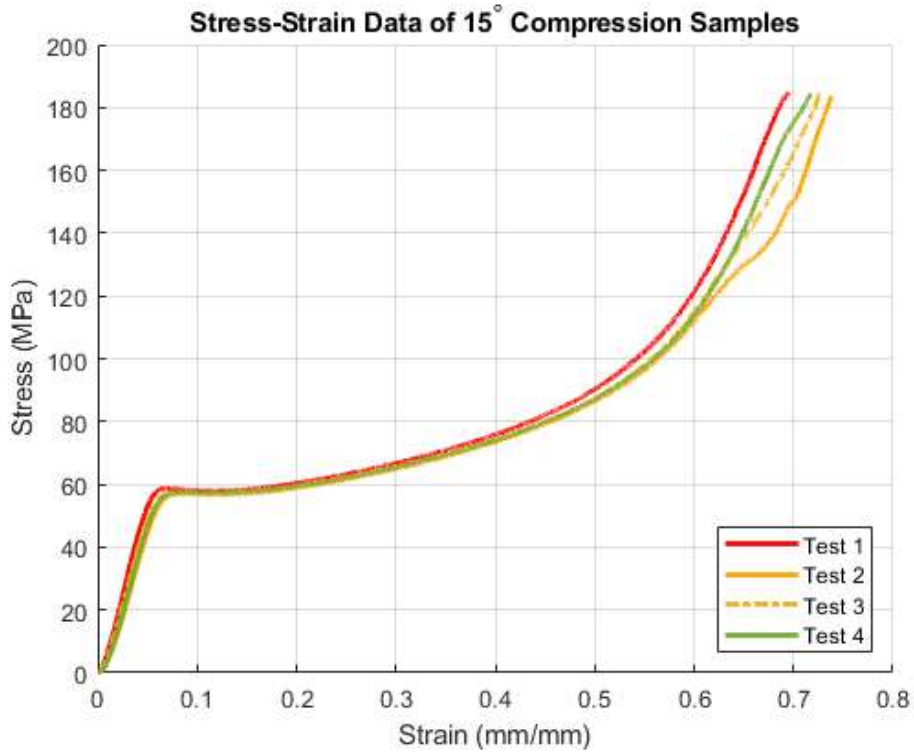

Figure 41 Individual stress-strain curves for all 15º compression specimens.

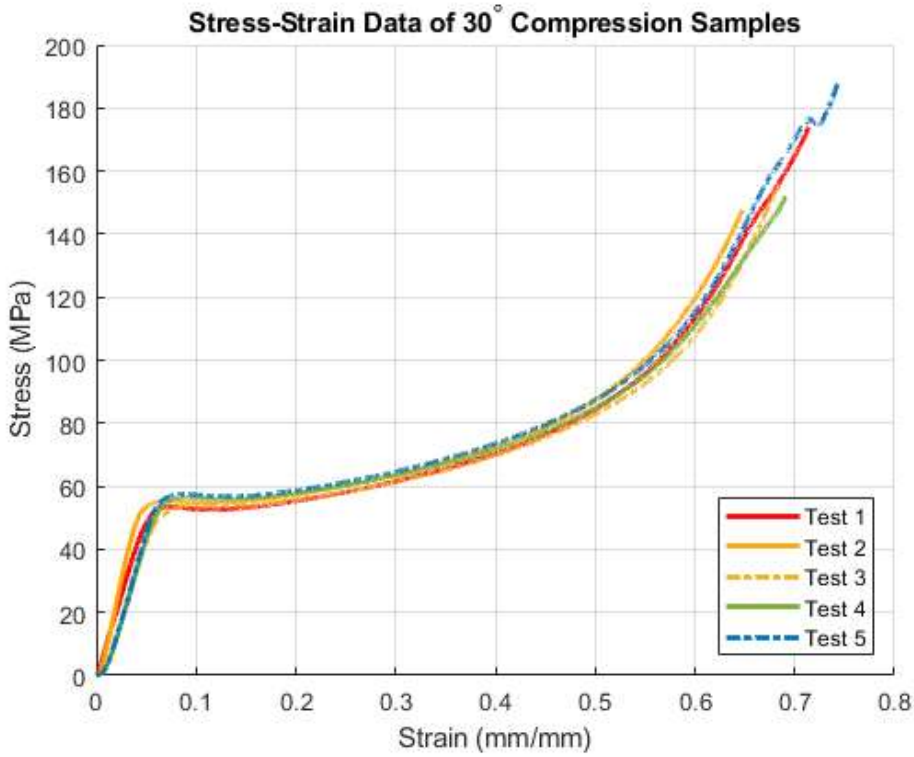

Figure 42 Individual stress-strain curves for all 30º compression specimens.

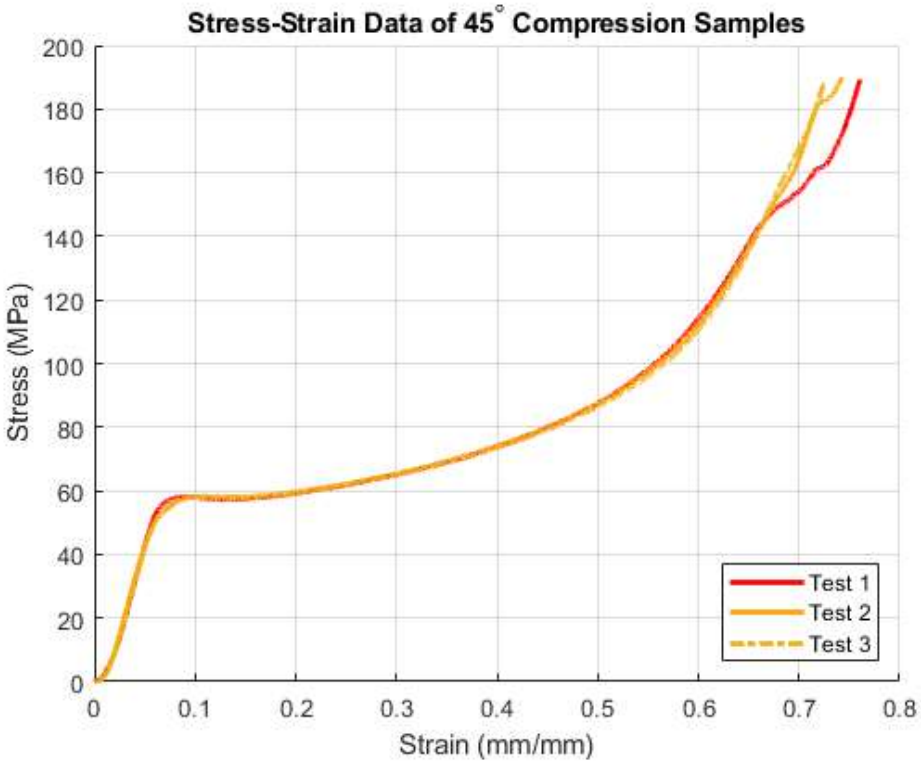

Figure 43 Individual stress-strain curves for all 45º compression specimens.

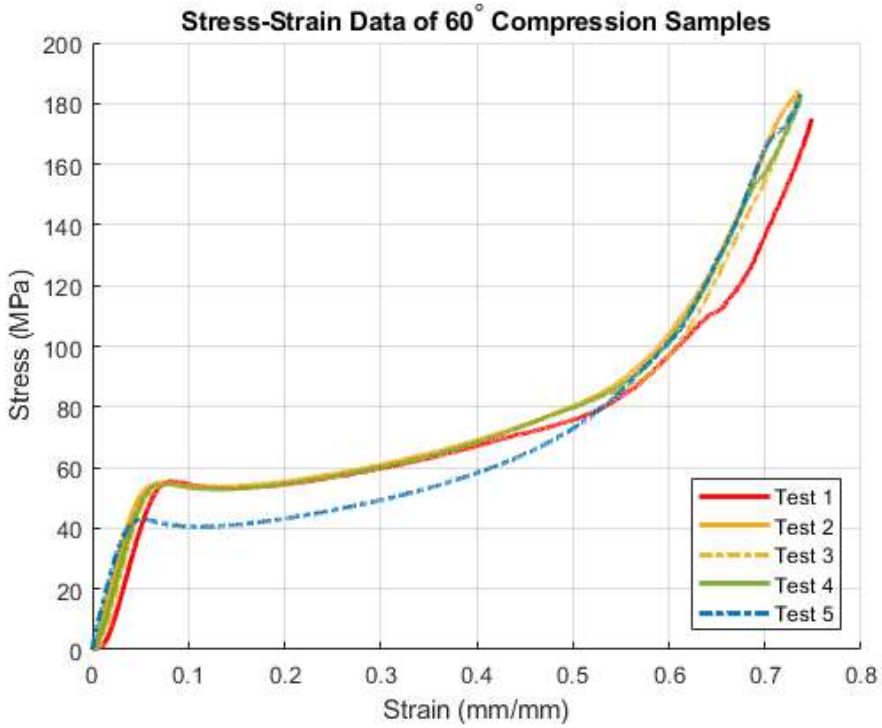

Figure 44 Individual stress-strain curves for all 60º compression specimens.

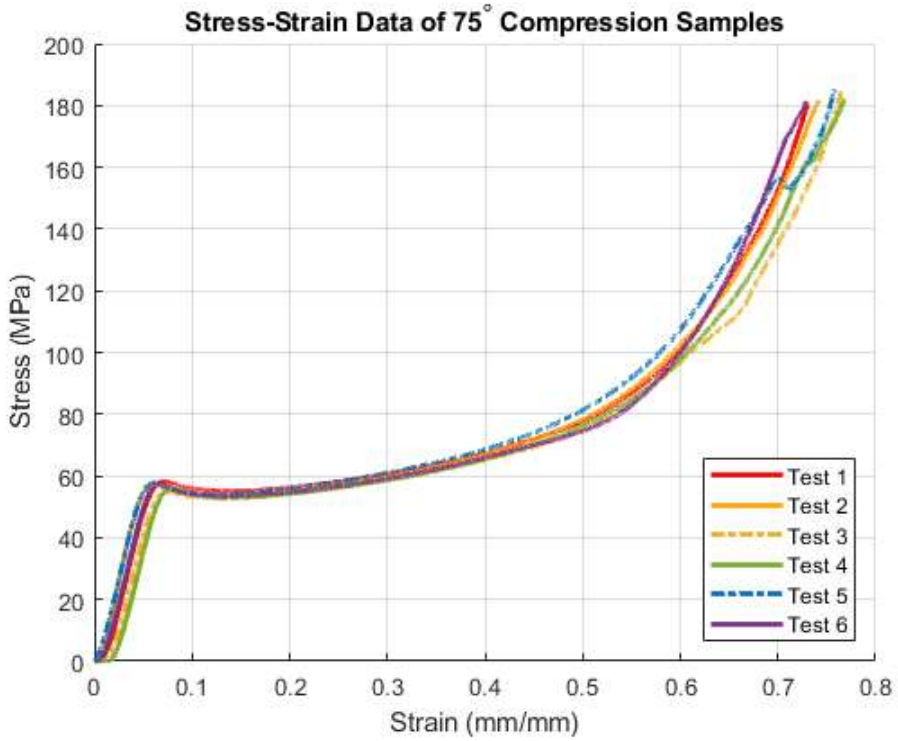


Figure 45 Individual stress-strain curves for all 75º compression specimens.

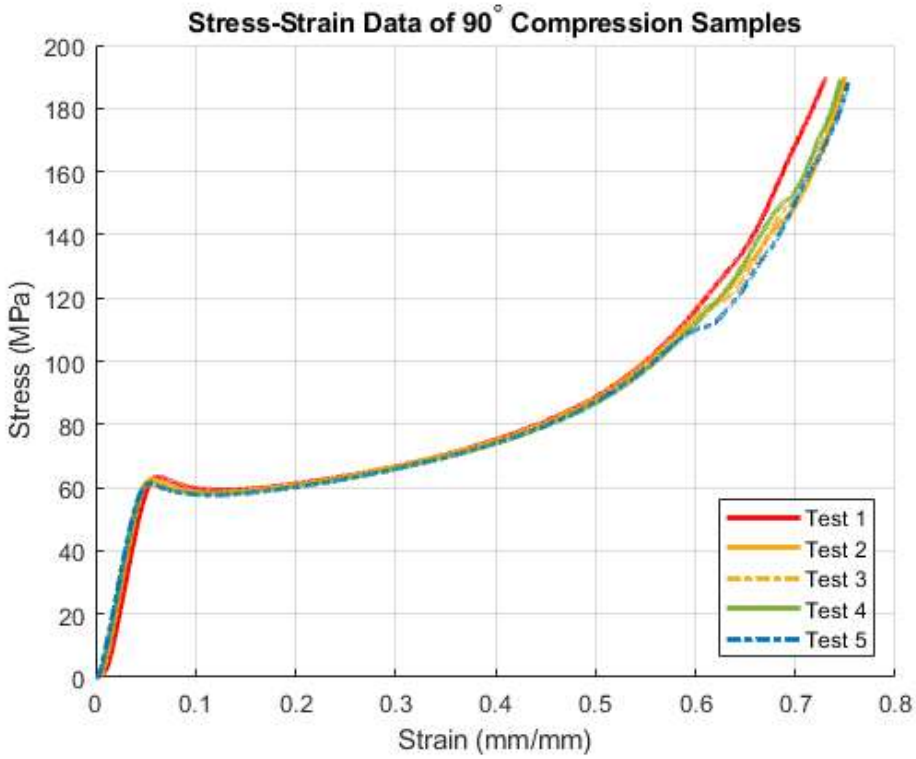


Figure 46 Individual stress-strain curves for all 90º compression specimens.

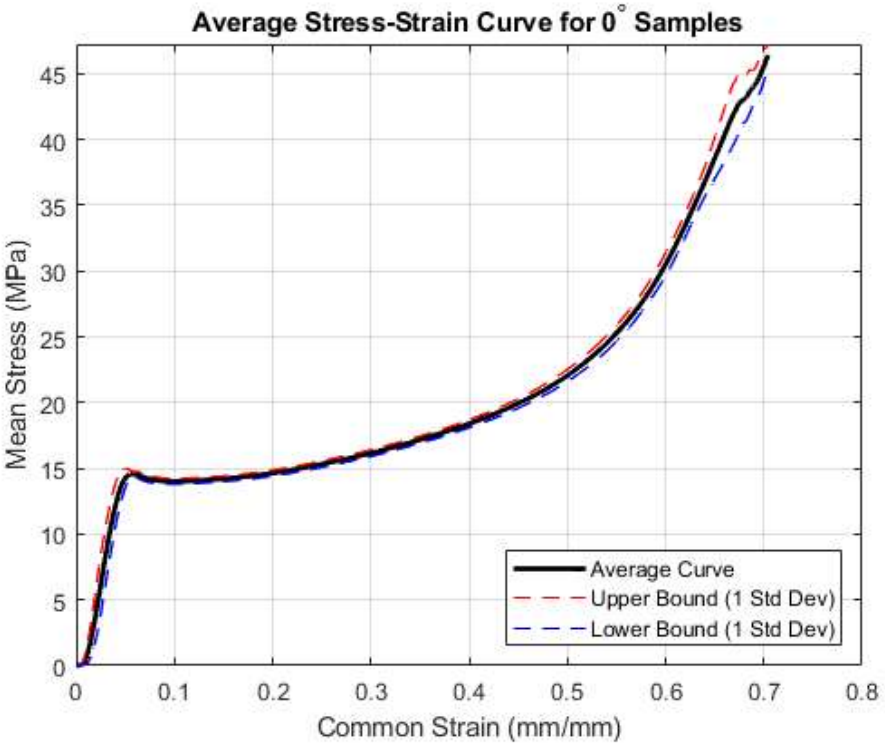


Figure 47 Average stress-strain curves for 0º compression specimens.

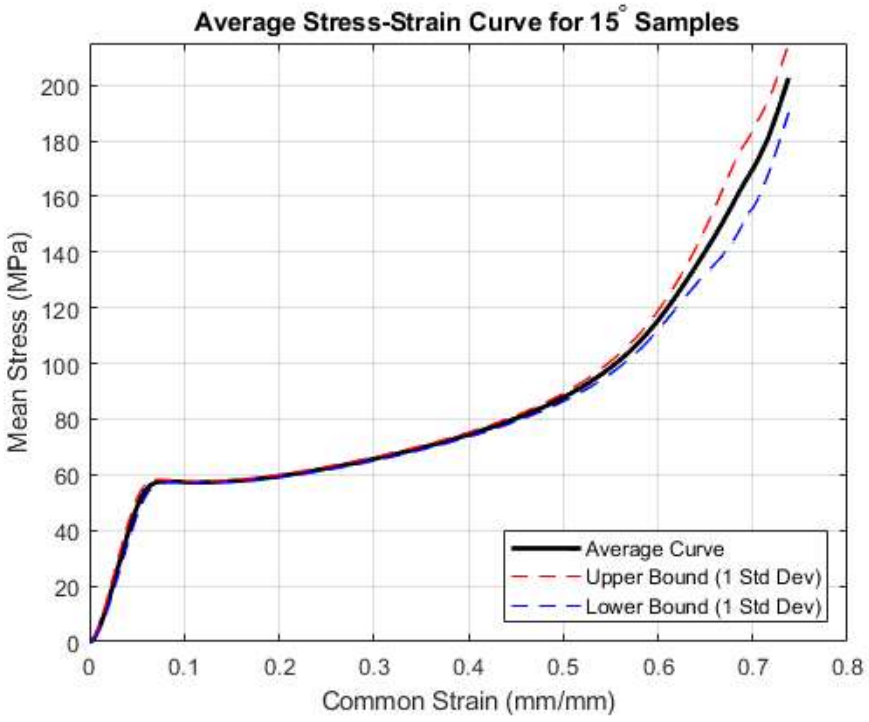


Figure 48 Average stress-strain curves for 15º compression specimens.

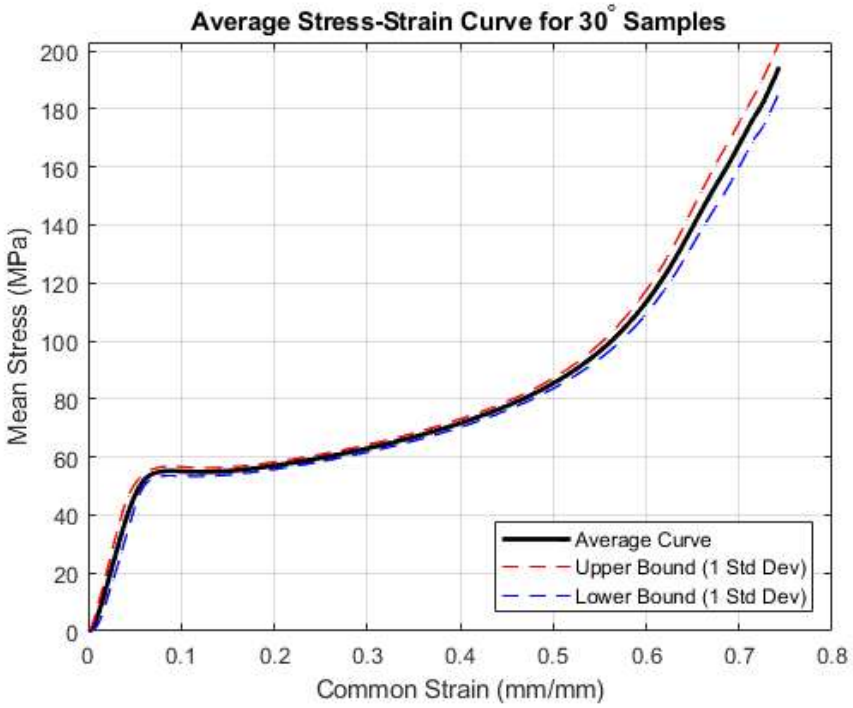


Figure 49 Average stress-strain curves for 30º compression specimens.

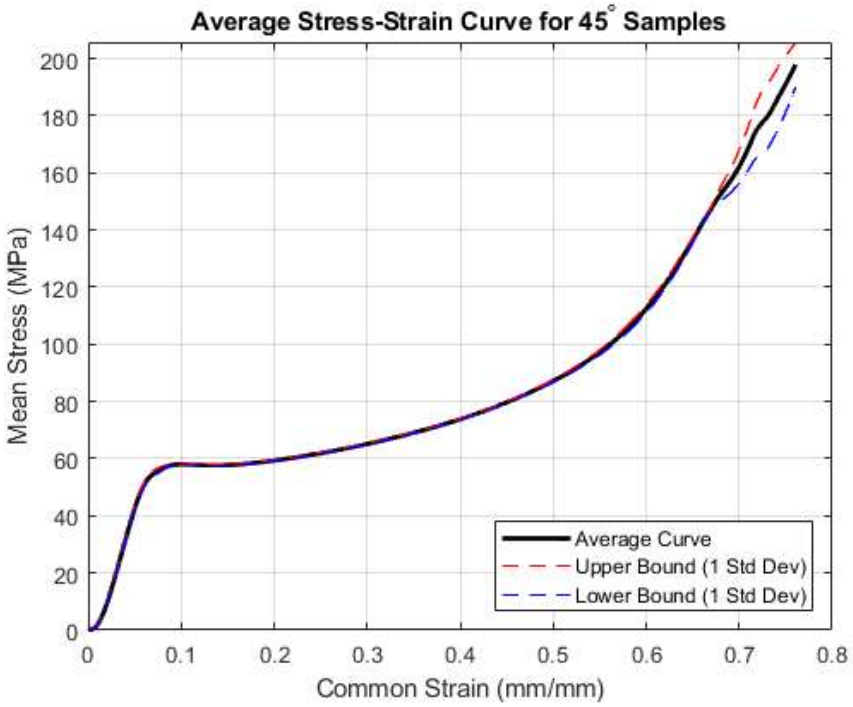


Figure 50 Average stress-strain curves for 45º compression specimens.

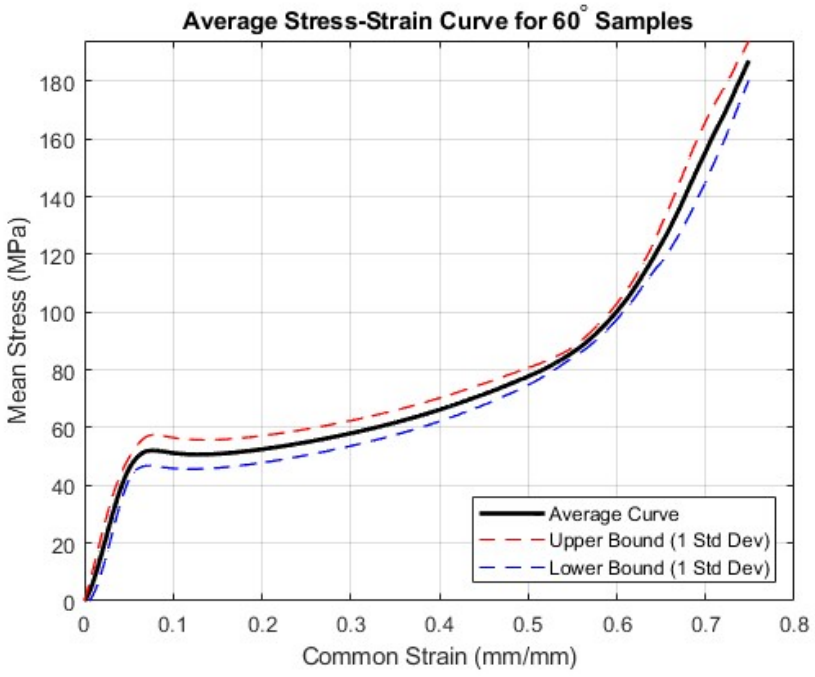


Figure 51 Average stress-strain curves for 60º compression specimens.

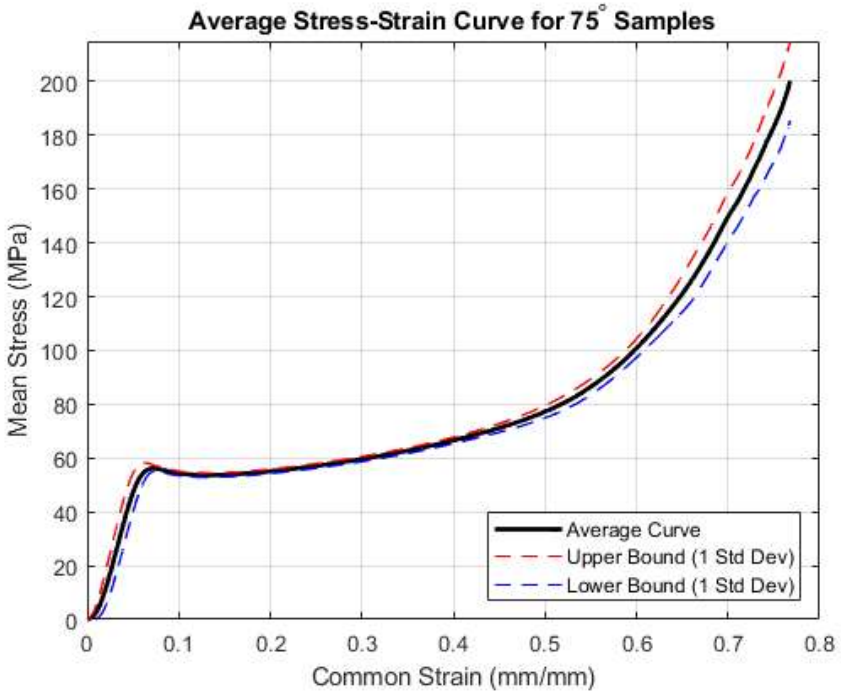


Figure 52 Average stress-strain curves for 75º compression specimens.

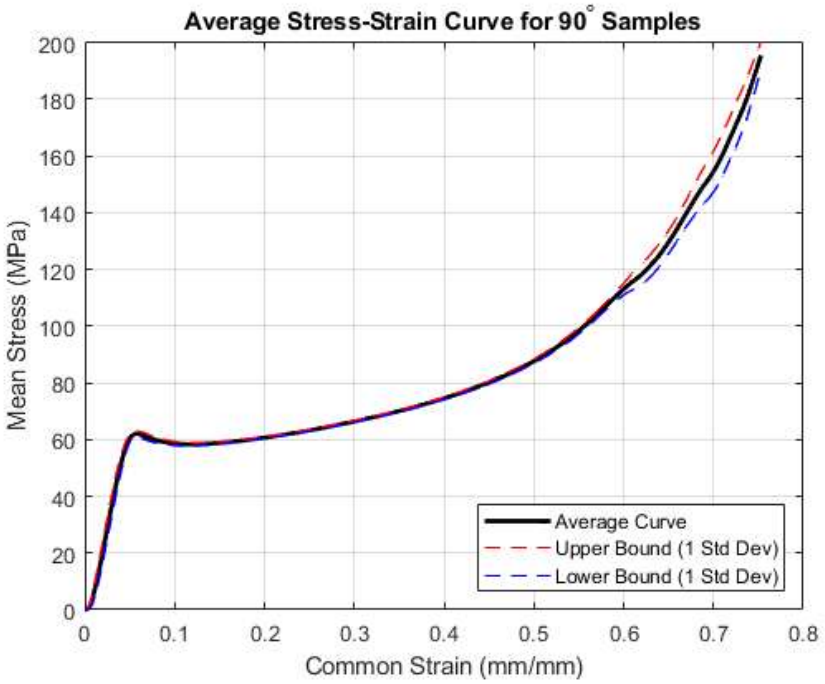


Figure 53 Average stress-strain curves for 90º compression specimens.

### 5.3.1. Discussion of Compression Testing Results

The data analysis focused on ultimate compressive stress (UCS), stress at fracture, strain at fracture, compressive modulus, 0.2% offset yield strength, densification modulus, and densification strain. The UCS was identified as the highest stress measured on the testing curve, which occurred near the end of Phase III for all tests in this section. The stress and strain at fracture were recorded at the point where the specimen failed. Like Young's Modulus in tensile testing, the compressive modulus ($E_c$) is calculated from the initial linear portion of the stress-strain curve, representing the material's stiffness under compressive loading. The 0.2% offset compressive yield strength is calculated in the same way as for tensile mode. The Densification Modulus ($E_{densification}$) quantifies the change in a material's stiffness as it undergoes densification, particularly in materials that undergo significant compaction, such as polymers, foams, or cellular solids [115]. This

modulus is derived from the slope of the stress-strain curve in the densification region after linear fitting, following the stress plateau phase. It is determined by performing a linear fit in this region, which marks the transition to the second phase of rigid material behavior. It is calculated as:

$$E_{densification} = \frac{\Delta\sigma}{\Delta\epsilon} \tag{6}$$

where $\Delta\sigma$ is the change in stress in MPa within the densification region, and $\Delta\epsilon$ is the corresponding change in strain. Densification strain ($\epsilon_{densification}$) represents the strain level at which the material enters the densification region during compression. This point marks the transition from energy absorption to a phase where the material's structure begins to compact significantly. Beyond the onset of densification strain, the material continues to absorb energy, but this comes at the cost of increased stress being transferred throughout the structure, leading to damage or collapse of the material's internal structure, but not catastrophic failure [116]. It is calculated as:

$$\epsilon_{densification} = \frac{E_{densification}}{\alpha} \tag{7}$$

where $E_{densification}$ is the densification modulus, and $\alpha$ is calculated from the linear fit result to the densification region.

The compression data shows that as print orientation increases from 0° to 90°, there is a significant improvement in mechanical properties. The most significant increases occurred between the 0° and 15° sample sets for ultimate compressive strength (UCS), fracture stress, compression modulus, and densification modulus; this was followed by a slight to moderate percentage increase from 15° to 90°. Otherwise, fracture strain and densification strain remained constant across all print orientations. Overall, UCS increased by approximately 323.5%, from 14.72 MPa at 0° to 62.33 MPa at 90°. There is a 292.3% increase from 0° to 15°, followed by a 7.99% increase from 15° to 90°. Similarly, fracture stress increases by 309.4% from 0° to 15°,

followed by a slight 1.96% increase from 15° to 90°, with an overall increase of 317.9%. The compressive modulus showed a 195.7% rise from 0° to 15°, followed by a plateau from 15° to 75°, and a subsequent 40.71% increase from 75° to 90%, resulting in a 309% overall increase. This indicates that the material becomes much stronger and stiffer at higher orientations. Yield strength increased by 302.3%, from 14.37 MPa at 0° to 57.81 MPa at 90°, with a 262.4% increase from 0° to 15°. Fracture and densification strain remained relatively consistent across all orientations, suggesting stable ductility. This analysis demonstrates that higher print orientations significantly enhance the material's strength and stiffness. Boxplots showing material properties variation with print orientation can be seen in Figure 54b) to f). The average values for mechanical properties of compression testing, in tabulated numerical form, can be found in Table 8.

Table 8 Average Mechanical Properties of Compression Testing.

| Print Orientation | UCS | Fracture Stress | Fracture Strain | Compression Modulus | Yield Strength | Densification Strain | Densification Modulus |
|---|---|---|---|---|---|---|---|
| [º] | [MPa] | [MPa] | [mm/mm] | [MPa] | [MPa] | [mm/mm] | [MPa] |
| 0 | 14.71648 | 14.02188 | 0.09994 | 377.2283 | 14.367 | 0.425864 | 175.048 |
| 15 | 57.71097 | 57.40568 | 0.099954 | 1122.65 | 52.0905 | 0.367943 | 534.12 |
| 30 | 55.39493 | 55.05253 | 0.099967 | 1009.322 | 51.305 | 0.388714 | 536.766 |
| 45 | 58.10141 | 58.01256 | 0.099979 | 1030.967 | 52.258 | 0.427287 | 613.603 |
| 60 | 52.55309 | 51.19288 | 0.099953 | 889.968 | 49.9184 | 0.455138 | 647.902 |
| 75 | 56.96353 | 54.30789 | 0.099952 | 1097.05 | 55.66717 | 0.48426 | 694.24 |
| 90 | 62.32726 | 58.58861 | 0.099967 | 1543.62 | 57.8062 | 0.461392 | 652.28 |

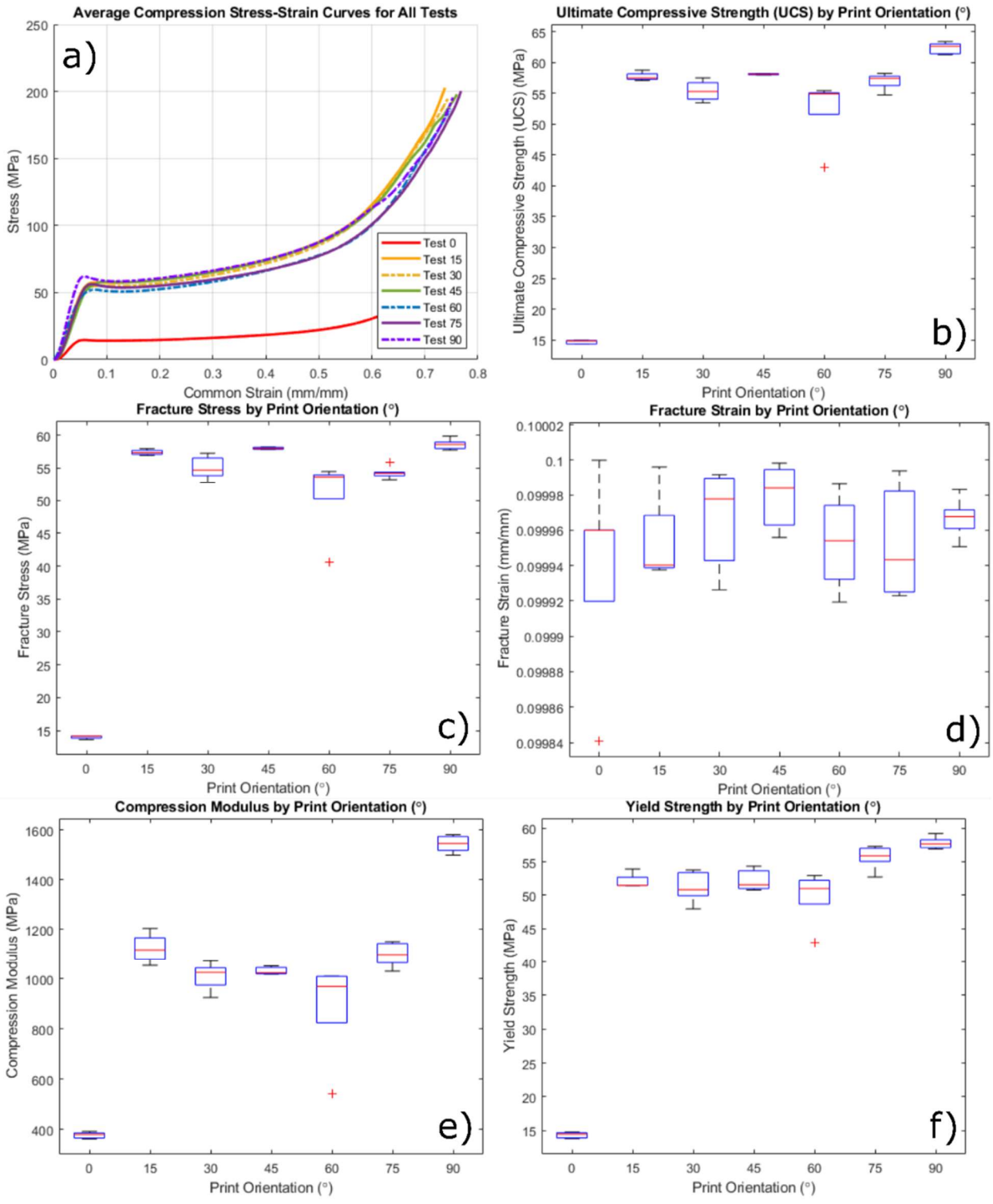


Figure 54 a) Average compressive stress-strain curves plotted on a common strain scale; b) Boxplot of UCS with print orientation; c) Boxplot of Fracture Stress with print orientation; d) Fracture Strain; e) Compression Modulus; f) Compressive Yield Strength.

After removing two outliers (as seen in Figure 55), the analysis of densification strain and modulus revealed a general trend of increase with print orientation. Initially, there is a slight decrease of 13.6% in densification strain from 0° to 15°. However, from 15° to 90°, the strain increases by 25.4%, peaking at 75° before a slight decline. Overall, densification strain shows an 8.34% increase from 0° to 90°, indicating a tendency for greater deformation before densification at higher orientations. The densification modulus demonstrates a substantial overall increase of 296.6%, with a notable 205% rise between the 0° and 15° orientations, highlighting a significant increase in the material's resistance to densification as the print orientation increases. It should be noted that increasing print orientation represents increasing gravitational loading upon the raster interlayer during the FDM process.

This suggests that as the material becomes more resistant to densification (indicated by a higher modulus), it also tends to experience greater strain before densification occurs. The slight decrease in densification modulus at the last data point may indicate a transitional phase in the material's behavior. Overall, higher magnitudes of gravity enhance the material's strength and stiffness, making it more robust under compressive loads.

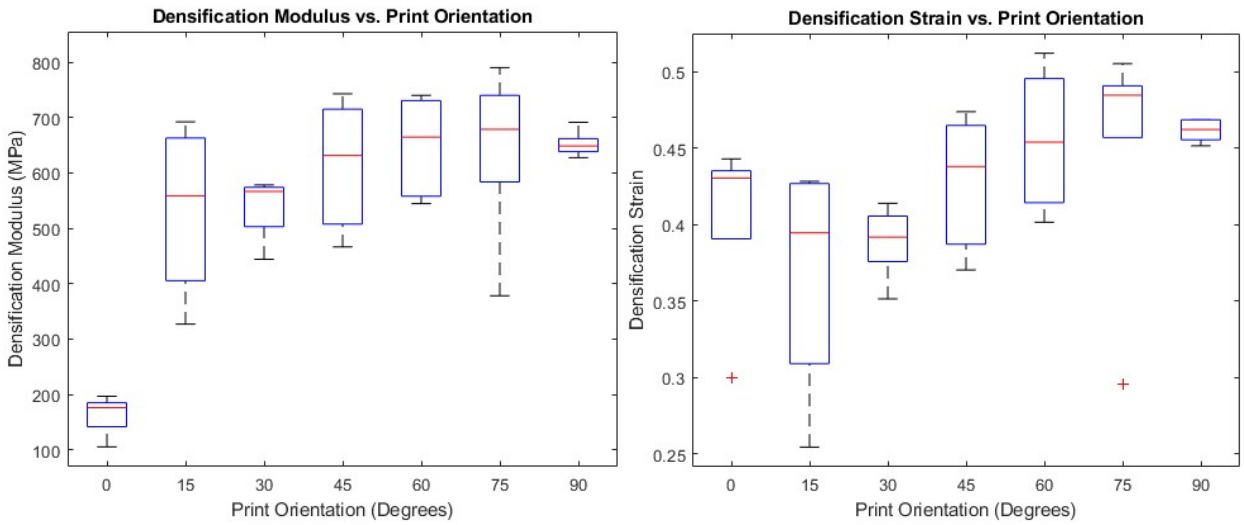


Figure 55 (Left) Boxplot showing variation in Densification Modulus with print orientation; (Right) variation in Densification Strain with print orientation.

Table 9 Original, Levene's Test, and Bonferroni Corrected p-values for Compression Specimens.

| Dependent Variable | p-values | | |
|---|---|---|---|
| | Original | Levene's Test | Bonferroni Corrected |
| UCS | $2.4932 \times 10^{-23}$ | 0.0031401 | $1.7446 \times 10^{-22}$ |
| Fracture Stress | $3.7115 \times 10^{-22}$ | 0.0015711 | $2.5981 \times 10^{-21}$ |
| Fracture Strain | 0.6664 | 0.17718 | 1.000 |
| Compression Modulus | $1.2585 \times 10^{-16}$ | 0.0097778 | $8.8093 \times 10^{-16}$ |
| Yield Strength | $1.7677 \times 10^{-23}$ | 0.063457 | $1.2374 \times 10^{-22}$ |
| Densification Strain | 0.090758 | 0.206 | 0.81682 |
| Densification Mod. | $6.2956 \times 10^{-8}$ | 0.013924 | $5.666 \times 10^{-7}$ |

Table 9 shows the p-values corresponding to the 1-way ANVOA performed on the compression stress-strain data. Overall, the p-values were acceptable for all parameters except for densification strain and fracture strain. The high p-values suggest that densification strain is not significantly impacted by print orientation in your data set, implying that the processes or material

characteristics related to densification strain remain relatively consistent across different orientations. After applying the Bonferroni correction, which adjusts for multiple comparisons, the non-significance of densification strain is further confirmed, with a corrected p-value of 0.81682, even higher than the original. This correction reduces the risk of Type I errors (false positives) and strengthens the conclusion that print orientation does not significantly affect densification strain. Additionally, p-values for fracture strain are similarly high. The residuals plots may be seen in Figure 56.

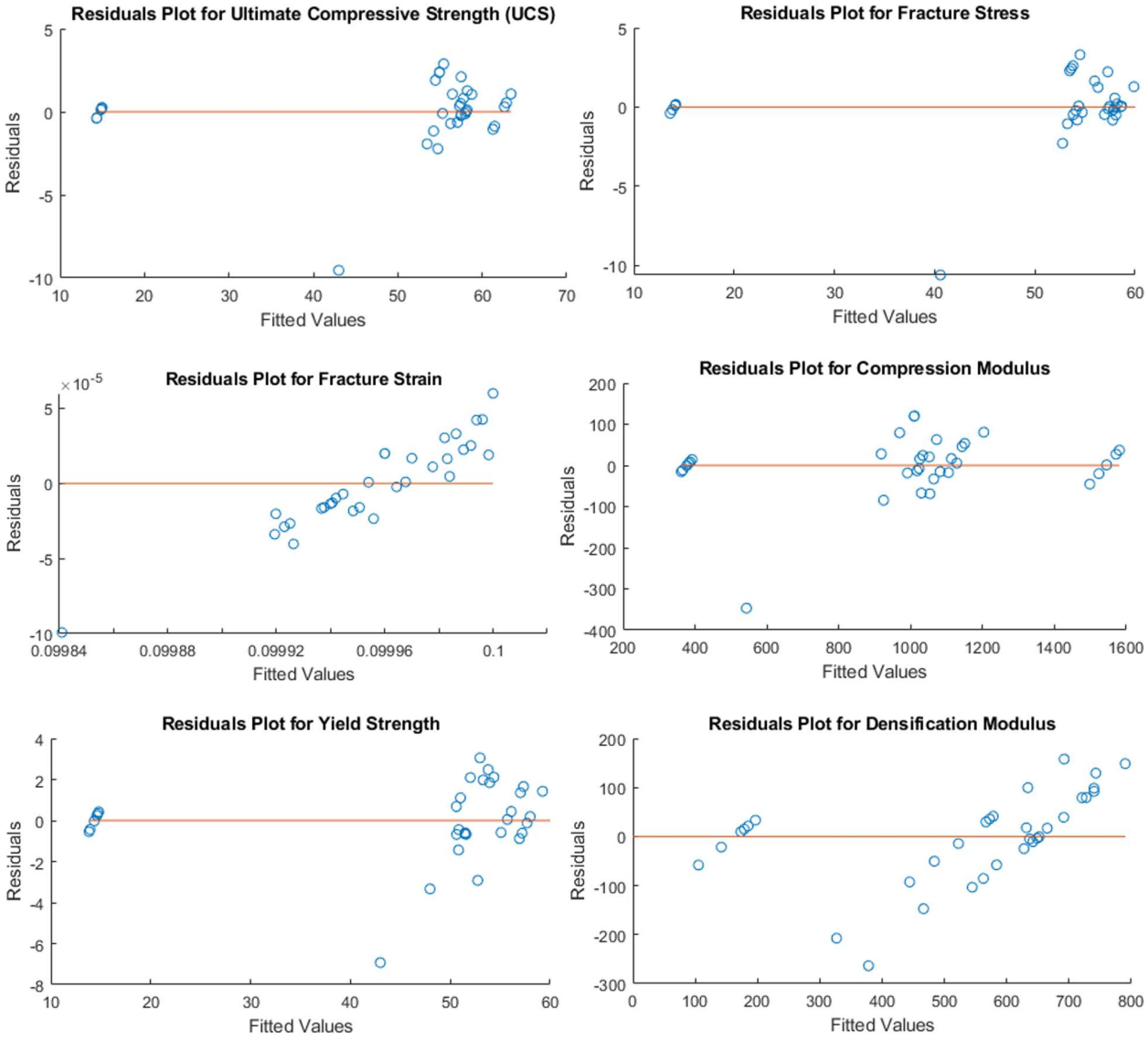

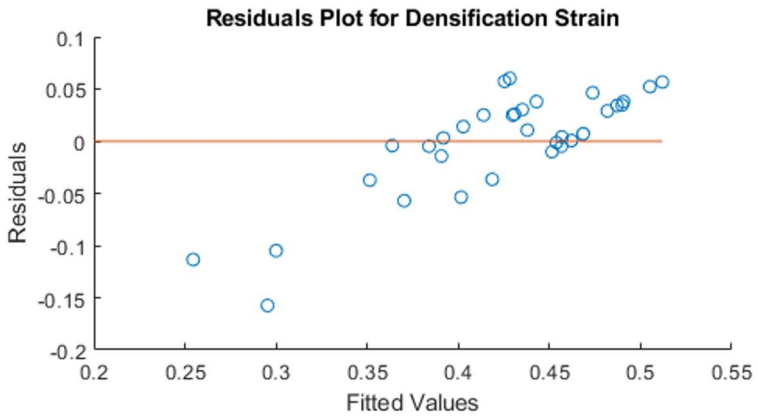


Figure 56 Residuals plots corresponding to the 1-way ANOVA for compression properties.

### 5.3.2. Discussion of Compression Testing Trends

The compression data reveals that mechanical properties improve significantly as print orientation increases from 0° to 90°, with the most notable gains occurring between 0° and 15°. Specifically, ultimate compressive strength (UCS) increases by 292.3%, fracture stress by 309.4%, compressive modulus by 195.7%, and densification modulus by 205% in this range. From 15° to 90°, these properties continue to improve, though at a slower rate, ultimately leading to an overall increase of 323.5% in UCS, 317.9% in fracture stress, and 309% in compressive modulus. Interestingly, fracture strain and densification strain remain relatively consistent across orientations, suggesting that they are not significantly affected by changes in print orientation.

The substantial gains observed from 0° to 15° suggest that the 0° print orientation, which simulates zero-gravity conditions, produces the weakest material properties. This observation indicates that even a small introduction of gravity influences the raster interlayer bond, resulting in significant increases in UCS, fracture stress, and densification modulus. These findings imply that zero-gravity conditions notably weaken the raster interlayer strength, leading to lower compressive properties. However, when comparing microgravity conditions to on-earth printing,

the compressive properties of FDM-AM ABS-M30 are only slightly diminished, indicating that microgravity exerts a lesser impact on material strength than complete zero-gravity conditions.

## 5.4. Dimensional Data

The dimensions for the tensile specimens included thickness and width, while the compression specimens were measured for length and diameter. All measurements were taken using a caliper. Trends were observed in the dimensions based on the print orientation, indicating a potential influence of orientation on the final specimen sizes. A one-way Analysis of Variance (ANOVA) was performed on the dimensional data to determine the statistical significance of the relationships.

Table 10 Tabulated Averages of Tensile Specimen Dimensions.

| Print Orientation | Thickness | Width |
|---|---|---|
| [º] | [mm] | [mm] |
| 0 | 2.724 | 6.118 |
| 15 | 2.72 | 6.06 |
| 30 | 2.70 | 6.132 |
| 45 | 2.66 | 6.05 |
| 60 | 2.574 | 6.066 |
| 75 | 2.47 | 5.91 |
| 90 | 2.364 | 5.592 |

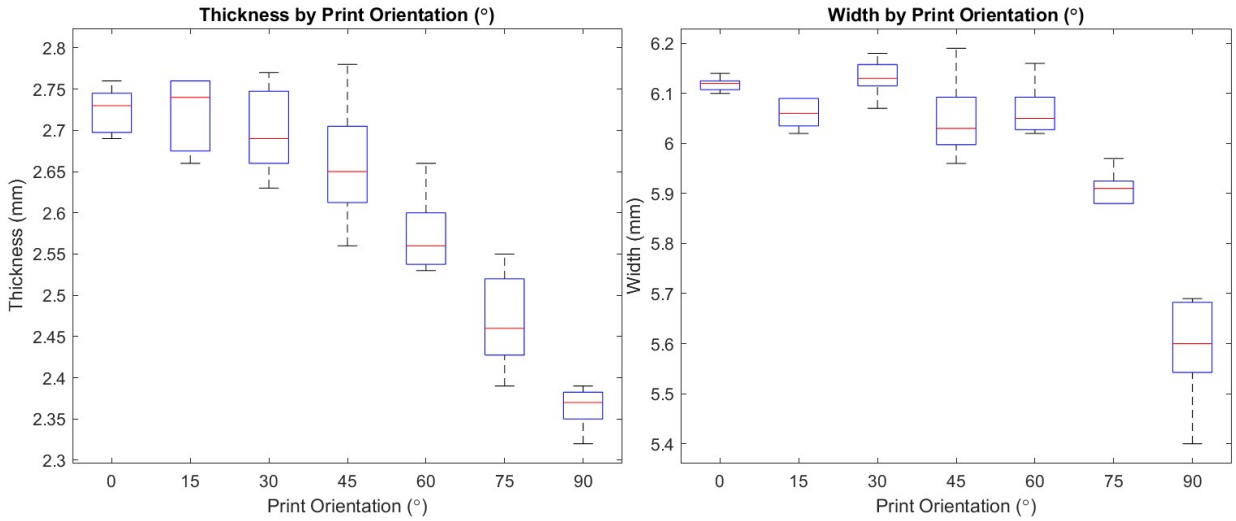

Figure 57 (Left) Boxplot of tensile specimen thickness with print orientation; (Right) Boxplot of tensile specimen width with print orientation.

Dimensions input into the CAD file for FDM manufacturing, according to ASTM D638-IV standards, were 6.0mm for thickness and 3.2mm for width. It should by noted that all specimens printed below the CAD-specified dimensions. There was a 13.23% decrease in thickness from 0° to 90°, with a consistent reduction as the print orientation increased. The width also trended downward, though with more variation, showing an 8.6% decrease from 0° to 90°. Notably, there were slight increases in width between 15° to 30° and 45° to 60°. Overall, the smallest dimensions were observed in the 90° specimens.

Table 11 Original, Levene's Test, and Bonferroni Corrected p-values corresponding to the 1-way ANOVA performed on the dimensional data of the tensile specimens.

| Dependent Variable | p-values | | |
|---|---|---|---|
| | Original | Levene's Test | Bonferroni Corrected |
| Thickness | $1.186 \times 10^{-11}$ | 0.41813 | $8.3019 \times 10^{-11}$ |
| Width | $4.8527 \times 10^{-13}$ | 0.1739 | $3.3969 \times 10^{-12}$ |

The p-values from the 1-way ANOVA indicate statistically significant differences in both thickness and width across the tested groups, with original p-values of $1.186 \times 10^{-11}$ and $4.8527 \times 10^{-13}$, respectively. Levene's Test p-values (0.41813 for thickness and 0.1739 for width) confirm that the assumption of equal variances is met. After applying the Bonferroni correction, the p-values remain significantly low, reinforcing the conclusion that the differences in thickness and width are highly significant across the groups.

Table 12 Tabulated Averages of Compression Specimen Dimensions.

| Print Orientation | Diameter | Length |
|---|---|---|
| [º] | [mm] | [mm] |
| 0 | 12.467 | 25.013 |
| 15 | 12.478 | 25.320 |
| 30 | 12.490 | 25.504 |
| 45 | 12.233 | 25.257 |
| 60 | 12.482 | 25.630 |
| 75 | 12.455 | 25.692 |
| 90 | 12.236 | 25.618 |

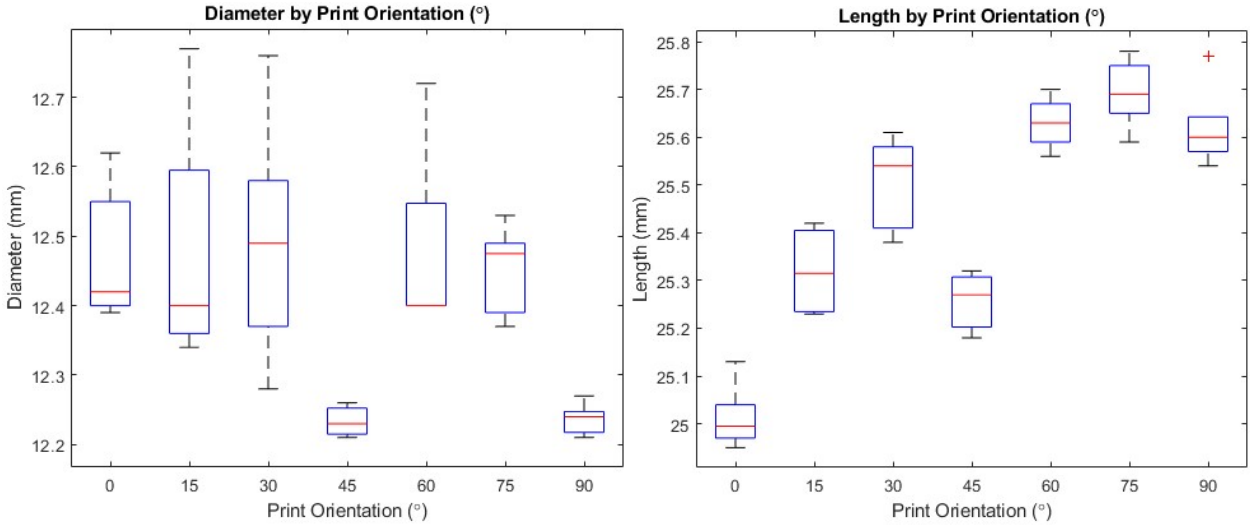


Figure 58 Boxplots of compression specimen diameter and length with print orientation.

The ASTM D695 standard specifies dimensions of 12.7 mm for diameter and 25.4 mm for length. However, all printed specimens had diameters slightly below the standard 12.7 mm. Additionally, three sample sets—0°, 15°, and 45°—had lengths shorter than the standardized 25.4 mm. Diameter measurements exhibited an overall decrease of approximately 1.85% from 0° to 90°, with some fluctuations, including minor increases between certain orientations. In contrast, the length shows an overall increase of about 2.42% from 0° to 90°, following a consistent upward trend, except for slight decreases of 0.97% and 0.26% between 30° to 45° and 75° to 90°, respectively.

Table 13 Original, Levene's Test, and Bonferroni Corrected p-values corresponding to the 1-way ANOVA performed on the dimensional data of the tensile specimens.

| Dependent Variable | p-values | | |
|---|---|---|---|
| | Original | Levene's Test | Bonferroni Corrected |
| Diameter | $4.942 \times 10^{-3}$ | 0.068147 | 0.03444 |
| Length | $1.0475 \times 10^{-13}$ | 0.42253 | $7.3325 \times 10^{-13}$ |

Both diameter and length show statistically significant differences across the tested groups. The Levene's Test results indicate that the assumption of equal variances is met for both variables, supporting the validity of the ANOVA results. The Bonferroni correction reinforces the significance of the findings, particularly for length, where the differences are extremely pronounced. The residuals plots for both the analyses may be seen in Figure 59 and Figure 60.

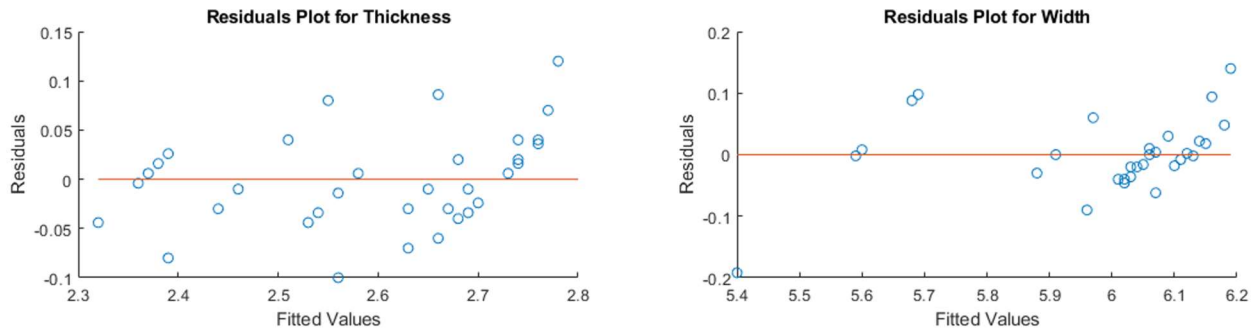


Figure 59 Residuals plots for the thickness and width of tensile specimens.

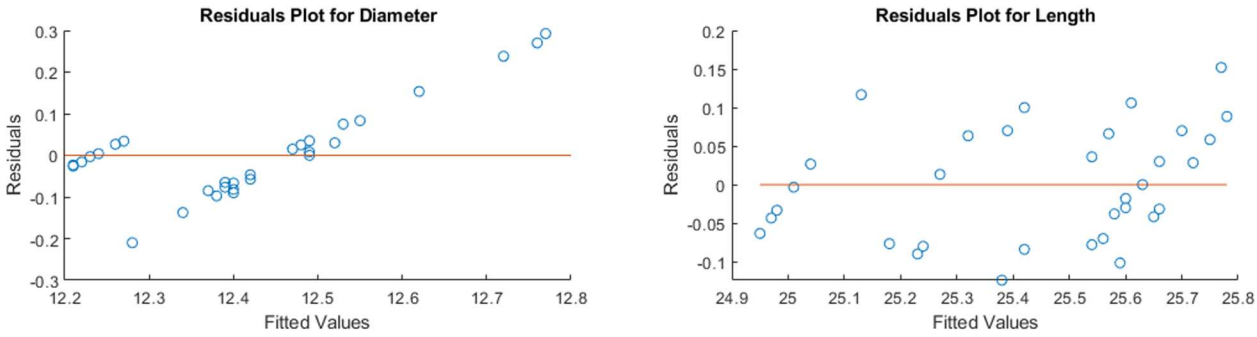


Figure 60 Residuals plots for the diameter and width of compression specimens.

### 5.4.1. Tensile Specimen Dimensional Variation

The dimensional analysis of tensile specimens revealed that all printed specimens were slightly smaller than the specified dimensions input into the printer. Thickness decreased by 13.23% from 0° to 90°, while width showed an 8.6% decrease over the same range, with slight increases between 15° to 30° and 45° to 60°. The smallest dimensions were observed in the 90° specimens, indicating that print orientation significantly affects the final dimensions. Higher orientations, representing higher gravitation, generally produces smaller parts. These dimensional variations suggest that the gravity level significantly affects the final dimensions of FDM-manufactured tensile specimens, with higher gravity levels generally producing smaller dimensions.

### 5.4.2. Compression Specimen Dimensional Variation

For compression specimens, the printed results also deviated slightly from the CAD input. All specimens had slightly smaller diameters, and three sets (0°, 15°, and 45°) had lengths below 25.4 mm. Diameter decreased by 1.85% from 0° to 90°, with some fluctuations, while length increased by 2.42%, except for slight decreases between 30° to 45° and 75° to 90°.These findings indicate that gravity level not only affects the tensile properties but also plays a significant role in determining the dimensional accuracy of compression specimens, particularly influencing the final diameter and length.

## 5.5. Micro-CT Results

A qualitative micro-CT analysis was performed to observe the presence of internal flaws and visually inspect the levels of fusion within the interlayer and the raster interlayer. The imaged specimen was a 0° sample designed to mimic a zero-gravity environment between the interlayers. Figure 61 presents a top-down view of this 0° specimen, clearly displaying the raster deposition pattern. A 0° specimen was chosen as this print orientation represents zero-gravity environments, and thus would be the optimal sample to image for microgravity-induced FDM part flaws. The image reveals visible gaps within the raster and some voids, indicating insufficient raster interlayer bonding, particularly at the ends of the sample.

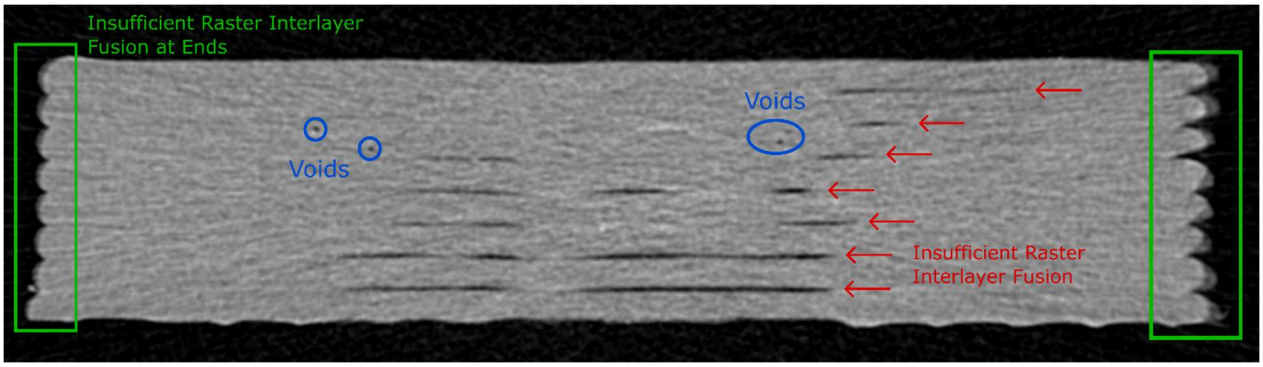


Figure 61 Top-down view of the raster deposition pattern of a 0° specimen, showcasing insufficient raster interlayer fusion, voids, and insufficient fusion at the extreme ends.

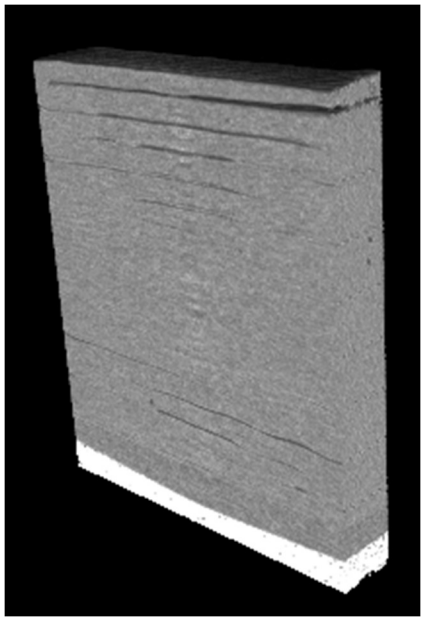

Figure 62 Orthographic view of a 0° sample under micro-CT imaging.

Figure 62 provides an orthographic view of a 3D volumetric cut-out of the same 0° specimen, clearly showing the interlayer structure. This view also shows incomplete interlayer fusion, particularly near the top of the 3D image, where interlayer gaps are most evident. The white portion visible at the bottom of the image corresponds to the metal base of the x-ray chamber, which

accounts for the reduced image quality in that region. The specimen image is cropped approximately halfway up, focusing on the bottom portion. This cropping was necessary due to a slight tilt in the micro-CT machine's stage, which caused poor image quality in the upper section, manifested as a pronounced ring effect. While the ring artifacts could be processed out in the lower layers of the image, the upper portion remained affected, so only the bottom half is displayed for clarity.

# Chapter 6 Conclusion and Future Work

## 6.1. Conclusion

The study demonstrates that the magnitude of gravity acting upon the raster interlayer significantly influences the mechanical properties and dimensional accuracy of parts fabricated by FDM AM using ABS-M30. The results of one-way ANOVAs for the tensile, compressive, and dimensional relationships indicate statistical significance.

Changes in gravitation was executed through a combination of raster pattern and print angle from the print bed. Tensile testing revealed a clear decline in UTS, fracture stress, and fracture strain, as print orientation increased from 0° to 75°. A recovery in these properties was observed at 90°, likely due to a shift in the failure mode from the raster interlayer to the regular interlayer. This suggests that the raster interlayer bond weakens with increasing print orientation due to the greater influence of gravity, which impacts bond strength.

Compression testing showed significant improvements in mechanical properties as print orientation increased from 0° to 90°, with the most substantial gains occurring between 0° and 15°. Ultimate compressive strength, fracture stress, compressive modulus, and densification modulus all increased significantly, indicating that the material becomes stronger and stiffer at higher orientations. Fracture strain and densification strain remained unaffected by changes in orientation, suggesting stable ductility across the tested range. The findings imply that zero-gravity conditions weaken the raster interlayer bond, leading to lower compressive properties, while microgravity

conditions have a lesser impact on material strength compared to on-earth printing.

Dimensional analysis revealed that print orientation significantly impacts the final dimensions of both tensile and compression specimens. Tensile specimens printed at higher orientations generally exhibited smaller dimensions, while compression specimens showed a slight decrease in diameter as print orientation increased. This suggests that gravity magnitude directly affects dimensional accuracy. The observed decrease in tensile properties and increase in compressive properties at higher gravitation may also be influenced by the reduced load-bearing area during testing due to these smaller dimensions.

## 6.2. Limitations

One limitation of this study is the lack of investigation into the effects of raster discontinuities during the printing process. Some FDM/FFF printers use a purge tower, where raster deposition is interrupted mid-layer to purge unwanted material. This process can create point discontinuities in the raster, which may act as weak spots during mechanical testing, potentially leading to premature failure in those areas.

Another limitation is the study's focus on raster interlayer and regular interlayer bonding without exploring the broader impact of microgravity on the FDM 3D printing process. The physical effects of microgravity on heat transfer mechanisms were not addressed. In zero-gravity environments, convection is significantly diminished or even non-existent due to the lack of buoyancy-driven fluid movement. This reduction in convection can impact the cooling and solidification of the printed material. While conduction and radiation remain unaffected by gravity, the absence of natural convection could influence the quality and consistency of the printed layers in ways not explored in this thesis.

## 6.3. Contribution

This study contributes to the understanding of how gravity levels impact the mechanical properties and dimensional accuracy of parts fabricated by FDM AM by controlling the gravity level at the interfaces of the raster interlayer. It provides valuable insights into how gravity direction influences the final dimensions and mechanical properties of the printed parts.

## 6.4. Future Work

Future research could extend this study by incorporating point discontinuities where applicable to assess their impact on material strength and failure mechanisms. Additionally, conducting similar experiments under conditions that simulate zero-gravity and microgravity heat transfer mechanisms, potentially within a vacuum chamber, would provide a more accurate and realistic model. For a more comprehensive bulk material analysis, micro-CT imaging of samples at different gravity magnitudes (45° and 90°) is a possible research direction. Lastly, developing a comprehensive process-structure-properties framework that explores the relationship between gravity levels and material and mechanical properties would significantly enhance our understanding of how different gravitational conditions affect the properties of parts fabricated by FDM AM.

*All raw data from this thesis is available upon request.*

# Bibliography


[1] B. Sawik, "Space Mission Risk, Sustainability and Supply Chain: Review, Multi-Objective Optimization Model and Practical Approach," *Sustainability*, vol. 15, no. 14, Art. no. 14, Jan. 2023, doi: 10.3390/su151411002.

[2] M. Hoffmann and A. Elwany, "In-Space Additive Manufacturing: A Review," *J. Manuf. Sci. Eng.*, vol. 145, no. 020801, Nov. 2022, doi: 10.1115/1.4055603.

[3] T. Ghidini, "An Overview of Current AM activities at the European Space Agency," presented at the Industrial Applications Global Summit 2013, London, UK, Nov 19-20. [Online]. Available: http://www.3d-printing-additive-manufacturing.com/media/downloads/52-d1-12-20-c-tommaso-ghidini-esa.pd

[4] K. Ishfaq, M. Asad, M. Mahmood, M. Abdullah, and C. Pruncu, "Opportunities and challenges in additive manufacturing used in space sector:a comprehensive review," *Rapid Prototyp. J.*, vol. ahead-of-print, Sep. 2021, doi: 10.1108/RPJ-04-2021-0091.

[5] D. Syrlybayev, B. Zharylkassyn, A. Seisekulova, M. Akhmetov, A. Perveen, and D. Talamona, "Optimisation of Strength Properties of FDM Printed Parts-A Critical Review," *Polymers*, vol. 13, no. 10, p. 1587, May 2021, doi: 10.3390/polym13101587.

[6] F. Ferranti, M. Del Bianco, and C. Pacelli, "Advantages and Limitations of Current Microgravity Platforms for Space Biology Research," *Appl. Sci.*, vol. 11, no. 1, Art. no. 1, Jan. 2021, doi: 10.3390/app11010068.

[7] V. Pletser, "Aircraft Parabolic Flights: A Gateway to Orbital Microgravity and Extra-Terrestrial Planetary Gravities," May 2020, doi: 10.5772/intechopen.93464.

[8] W. Hu and Q. Kang, Eds., *Physical Science Under Microgravity: Experiments on Board the*

*SJ-10 Recoverable Satellite*. in Research for Development. Singapore: Springer Singapore, 2019. doi: 10.1007/978-981-13-1340-0.

[9] A. Cowley *et al.*, "Effects of variable gravity conditions on additive manufacture by fused filament fabrication using polylactic acid thermoplastic filament," *Addit. Manuf.*, vol. 28, pp. 814–820, Aug. 2019, doi: 10.1016/j.addma.2019.06.018.

[10] Q. A. Bean, K. G. Cooper, J. E. Edmunson, M. M. Johnston, and M. J. Werkheiser, "INTERNATIONAL SPACE STATION (ISS) 3D PRINTER PERFORMANCE AND MATERIAL CHARACTERIZATION METHODOLOGY".

[11] T. Prater, "Summary Report on Phase I Results From the 3D Printing in Zero-G Technology Demonstration Mission Volume I."

[12] T. J. Prater and N. J. Werkheiser, "Summary Report on Phase I and Phase II Results From the 3D Printing in Zero-G Technology Demonstration Mission, Volume II".

[13] T. Prater *et al.*, "Analysis of specimens from phase I of the 3D printing in Zero G technology demonstration mission," *Rapid Prototyp. J.*, vol. 23, no. 6, pp. 1212–1225, Jan. 2017, doi: 10.1108/RPJ-09-2016-0142.

[14] T. J. Prater *et al.*, "A Ground-Based Study on Extruder Standoff Distance for the 3D Printing in Zero Gravity Technology Demonstration Mission." Jun. 01, 2017. Accessed: Jul. 22, 2024. [Online]. Available: https://ntrs.nasa.gov/citations/20170005539

[15] T. Prater, N. Werkheiser, F. Ledbetter, D. Timucin, K. Wheeler, and M. Snyder, "3D Printing in Zero G Technology Demonstration Mission: Complete Experimental Results and Summary of Related Material Modeling Efforts," *Int. J. Adv. Manuf. Technol.*, vol. 101, no. 1–4, pp. 391–417, Mar. 2019, doi: 10.1007/s00170-018-2827-7.

[16] G. Musso *et al.*, "Portable on Orbit Printer 3D: 1st European Additive Manufacturing

Machine on International Space Station," vol. 489, 2016, pp. 643–655. doi: 10.1007/978-3-319-41694-6_62.

[17] "China conducts 1st 3D printing experiment in space - China Military." Accessed: Jun. 24, 2024. [Online]. Available: http://eng.chinamil.com.cn/CHINA_209163/TopStories_209189/9808745.html

[18] W. J. Swanson, P. W. Turley, P. J. Leavitt, P. J. Karwoski, J. E. LaBossiere, and R. L. Skubic, "High temperature modeling apparatus," US6722872B1, Apr. 20, 2004 Accessed: Jul. 23, 2024. [Online]. Available: https://patents.google.com/patent/US6722872B1/en

[19] "Trademark Status & Document Retrieval." Accessed: Jul. 23, 2024. [Online]. Available: https://tsdr.uspto.gov/#caseNumber=4325106&caseSearchType=US_APPLICATION&caseType=DEFAULT&searchType=statusSearch

[20] A. Bellini, S. Gu¨c¸eri, and M. Bertoldi, "Liquefier Dynamics in Fused Deposition," *J. Manuf. Sci. Eng.*, vol. 126, no. 2, pp. 237–246, Jul. 2004, doi: 10.1115/1.1688377.

[21] S. Vyavahare, S. Teraiya, D. Panghal, and S. Kumar, "Fused deposition modelling: a review," *Rapid Prototyp. J.*, vol. 26, no. 1, pp. 176–201, Jan. 2019, doi: 10.1108/RPJ-04-2019-0106.

[22] "Xometry_DesignGuide_FDM.pdf." Accessed: Jul. 23, 2024. [Online]. Available: https://cdn2.hubspot.net/hubfs/340051/Design_Guides/Xometry_DesignGuide_FDM.pdf

[23] S. Han, J. Park, and J. Kim, *Typical structure of the Bowden FFF machine*. Accessed: Jul. 28, 2024. [Electronic]. Available: https://www.mdpi.com/electronics/electronics-12-01918/article_deploy/html/images/electronics-12-01918-g001.png

[24] "Deed - Attribution 4.0 International - Creative Commons." Accessed: Aug. 09, 2024. [Online]. Available: https://creativecommons.org/licenses/by/4.0/

[25] S. Ahn, M. Montero, D. Odell, S. Roundy, and P. K. Wright, "Anisotropic material properties of fused deposition modeling ABS," *Rapid Prototyp. J.*, vol. 8, no. 4, pp. 248–257, Oct. 2002, doi: 10.1108/13552540210441166.

[26] K. M. Ashtankar, A. M. Kuthe, and B. S. Rathour, "Effect of Build Orientation on Mechanical Properties of Rapid Prototyping (Fused Deposition Modelling) Made Acrylonitrile Butadiene Styrene (ABS) Parts," presented at the ASME 2013 International Mechanical Engineering Congress and Exposition, American Society of Mechanical Engineers Digital Collection, Apr. 2014. doi: 10.1115/IMECE2013-63146.

[27] W. Smith and R. Dean, "Structural characteristics of fused deposition modeling polycarbonate material," *Polym. Test.*, vol. 32, pp. 1306–1312, Dec. 2013, doi: 10.1016/j.polymertesting.2013.07.014.

[28] O. S. Carneiro, A. F. Silva, and R. Gomes, "Fused deposition modeling with polypropylene," *Mater. Des.*, vol. 83, pp. 768–776, Oct. 2015, doi: 10.1016/j.matdes.2015.06.053.

[29] M. Eryildiz, "Effect of Build Orientation on Mechanical Behaviour and Build Time of FDM 3D-Printed PLA Parts: An Experimental Investigation," *Eur. Mech. Sci.*, vol. 5, no. 3, pp. 116–120, Sep. 2021, doi: 10.26701/ems.881254.

[30] M. A. N. B. Mohd Khairul Nizam, K. I. B. Ismail, and T. C. Yap, "The Effect of Printing Orientation on the Mechanical Properties of FDM 3D Printed Parts," in *Enabling Industry 4.0 through Advances in Manufacturing and Materials*, A. S. Abdul Sani, M. N. Osman Zahid, M. R. Mohamad Yasin, S. Z. Ismail, M. Z. Mohd Zawawi, A. R. Abdul Manaf, S. N. Mohd Saffe, R. Abd Aziz, and F. Mohd Turan, Eds., in Lecture Notes in Mechanical Engineering. , Singapore: Springer Nature Singapore, 2022, pp. 75–85. doi: 10.1007/978-981-19-2890-1_8.

[31] J. Djokikj *et al.*, “Mechanical properties of parts fabricated with additive manufacturing: A review of mechanical properties of fused filament fabrication parts,” no. 8, 2022.

[32] C. R. Tripathy, R. K. Sharma, and V. K. Rattan, “Effect of printing parameters on the mechanical behaviour of the thermoplastic polymer processed by FDM technique: A research review,” *Adv. Prod. Eng. Manag.*, vol. 17, no. 3, pp. 279–294, Sep. 2022, doi: 10.14743/apem2022.3.436.

[33] C. S. Lee, S. G. Kim, H. J. Kim, and S. H. Ahn, “Measurement of anisotropic compressive strength of rapid prototyping parts,” *J. Mater. Process. Technol.*, vol. 187–188, pp. 627–630, Jun. 2007, doi: 10.1016/j.jmatprotec.2006.11.095.

[34] A. G. Salazar-Martín, M. A. Pérez, A.-A. García-Granada, G. Reyes, and J. M. Puigoriol-Forcada, “A study of creep in polycarbonate fused deposition modelling parts,” *Mater. Des.*, vol. 141, pp. 414–425, Mar. 2018, doi: 10.1016/j.matdes.2018.01.008.

[35] Q. Chen, J. D. Mangadlao, J. Wallat, A. De Leon, J. K. Pokorski, and R. C. Advincula, “3D Printing Biocompatible Polyurethane/Poly(lactic acid)/Graphene Oxide Nanocomposites: Anisotropic Properties,” *ACS Appl. Mater. Interfaces*, vol. 9, no. 4, pp. 4015–4023, Feb. 2017, doi: 10.1021/acsami.6b11793.

[36] S. Vanaei, M. Rastak, A. El Magri, H. R. Vanaei, K. Rassi, and A. Tcharkhtchi, “Orientation-Dependent Mechanical Behavior of 3D Printed Polylactic Acid Parts: An Experimental-Numerical Study,” *Machines*, vol. 11, no. 12, Dec. 2023, Accessed: Jul. 22, 2024. [Online]. Available: https://www.mdpi.com/2075-1702/11/12/1086

[37] Y. Li, K. Xu, X. Liu, M. Yang, J. Gao, and P. Maropoulos, “Stress-oriented 3D printing path optimization based on image processing algorithms for reinforced load-bearing parts,” *CIRP Ann.*, vol. 70, no. 1, pp. 195–198, Jan. 2021, doi: 10.1016/j.cirp.2021.04.037.

[38] N. H. Patadiya, H. K. Dave, and S. R. Rajpurohit, "Effect of Build Orientation on Mechanical Strength of FDM Printed PLA," in *Advances in Additive Manufacturing and Joining*, M. S. Shunmugam and M. Kanthababu, Eds., Singapore: Springer, 2020, pp. 301–307. doi: 10.1007/978-981-32-9433-2_26.

[39] M. S. Uddin, M. F. R. Sidek, M. A. Faizal, R. Ghomashchi, and A. Pramanik, "Evaluating Mechanical Properties and Failure Mechanisms of Fused Deposition Modeling Acrylonitrile Butadiene Styrene Parts," *J. Manuf. Sci. Eng.*, vol. 139, no. 081018, Jun. 2017, doi: 10.1115/1.4036713.

[40] A. R. Torrado, C. M. Shemelya, J. D. English, Y. Lin, R. B. Wicker, and D. A. Roberson, "Characterizing the effect of additives to ABS on the mechanical property anisotropy of specimens fabricated by material extrusion 3D printing," *Addit. Manuf.*, vol. 6, pp. 16–29, Apr. 2015, doi: 10.1016/j.addma.2015.02.001.

[41] J. M. Chacón, M. A. Caminero, E. García-Plaza, and P. J. Núñez, "Additive manufacturing of PLA structures using fused deposition modelling: Effect of process parameters on mechanical properties and their optimal selection," *Mater. Des.*, vol. 124, pp. 143–157, Jun. 2017, doi: 10.1016/j.matdes.2017.03.065.

[42] A. Lanzotti, M. Grasso, G. Staiano, and M. Martorelli, "The impact of process parameters on mechanical properties of parts fabricated in PLA with an open-source 3-D printer," *Rapid Prototyp. J.*, vol. 21, no. 5, pp. 604–617, Aug. 2015, doi: 10.1108/RPJ-09-2014-0135.

[43] S. Raut, V. S. Jatti, N. K. Khedkar, and T. P. Singh, "Investigation of the Effect of Built Orientation on Mechanical Properties and Total Cost of FDM Parts," *Procedia Mater. Sci.*, vol. 6, pp. 1625–1630, Jan. 2014, doi: 10.1016/j.mspro.2014.07.146.

[44] A. K. Sood, R. K. Ohdar, and S. S. Mahapatra, "Improving dimensional accuracy of Fused

Deposition Modelling processed part using grey Taguchi method," *Mater. Des.*, vol. 30, no. 10, pp. 4243–4252, Dec. 2009, doi: 10.1016/j.matdes.2009.04.030.

[45] M. S. Hossain, D. Espalin, J. Ramos, M. Perez, and R. Wicker, "Improved Mechanical Properties of Fused Deposition Modeling-Manufactured Parts Through Build Parameter Modifications," *J. Manuf. Sci. Eng.*, vol. 136, no. 061002, Oct. 2014, doi: 10.1115/1.4028538.

[46] O. Es-Said, J. Foyos, R. Noorani, M. Mendelson, R. Marloth, and B. Pregger, "Effect of Layer Orientation on Mechanical Properties of Rapid Prototyped Samples," *Mater. Manuf. Process.*, vol. 15, pp. 107–122, Jan. 2000, doi: 10.1080/10426910008912976.

[47] G. Onwubolu and F. Rayegani, "Characterization and Optimization of Mechanical Properties of ABS Parts Manufactured by the Fused Deposition Modelling Process," *Int. J. Manuf. Eng.*, vol. 2014, Nov. 2014, doi: 10.1155/2014/598531.

[48] S. H. Masood, "10.04 - Advances in Fused Deposition Modeling," in *Comprehensive Materials Processing*, S. Hashmi, G. F. Batalha, C. J. Van Tyne, and B. Yilbas, Eds., Oxford: Elsevier, 2014, pp. 69–91. doi: 10.1016/B978-0-08-096532-1.01002-5.

[49] X. Gao, D. Zhang, S. Qi, X. Wen, and Y. Su, "Mechanical properties of 3D parts fabricated by fused deposition modeling: Effect of various fillers in polylactide," *J. Appl. Polym. Sci.*, vol. 136, no. 31, p. 47824, 2019, doi: 10.1002/app.47824.

[50] H. Rezayat, W. Zhou, A. Siriruk, D. Penumadu, and S. S. Babu, "Structure–mechanical property relationship in fused deposition modelling," *Mater. Sci. Technol.*, vol. 31, no. 8, pp. 895–903, Jun. 2015, doi: 10.1179/1743284715Y.0000000010.

[51] O. A. Mohamed, S. H. Masood, and J. L. Bhowmik, "Optimization of fused deposition modeling process parameters: a review of current research and future prospects," *Adv.*

*Manuf.*, vol. 3, no. 1, pp. 42–53, Mar. 2015, doi: 10.1007/s40436-014-0097-7.

[52] S. Ziemian, M. Okwara, and C. Ziemian, "Tensile and fatigue behavior of layered acrylonitrile butadiene styrene," *Rapid Prototyp. J.*, vol. 21, pp. 270–278, Apr. 2015, doi: 10.1108/RPJ-09-2013-0086.

[53] M. Galeja, A. Hejna, P. Kosmela, and A. Kulawik, "Static and Dynamic Mechanical Properties of 3D Printed ABS as a Function of Raster Angle," *Materials*, vol. 13, no. 2, Art. no. 2, Jan. 2020, doi: 10.3390/ma13020297.

[54] H. Li *et al.*, "Bonding quality and fracture analysis of polyamide 12 parts fabricated by fused deposition modeling," *Rapid Prototyp. J.*, vol. 23, no. 6, pp. 973–982, Jan. 2017, doi: 10.1108/RPJ-03-2016-0033.

[55] W. Wu, P. Geng, G. Li, D. Zhao, H. Zhang, and J. Zhao, "Influence of Layer Thickness and Raster Angle on the Mechanical Properties of 3D-Printed PEEK and a Comparative Mechanical Study between PEEK and ABS," *Materials*, vol. 8, no. 9, Art. no. 9, Sep. 2015, doi: 10.3390/ma8095271.

[56] S. L. Messimer, T. Rocha Pereira, A. E. Patterson, M. Lubna, and F. O. Drozda, "Full-Density Fused Deposition Modeling Dimensional Error as a Function of Raster Angle and Build Orientation: Large Dataset for Eleven Materials," *J. Manuf. Mater. Process.*, vol. 3, no. 1, Art. no. 1, Mar. 2019, doi: 10.3390/jmmp3010006.

[57] A. Das *et al.*, "Current understanding and challenges in high temperature additive manufacturing of engineering thermoplastic polymers," *Addit. Manuf.*, vol. 34, p. 101218, Aug. 2020, doi: 10.1016/j.addma.2020.101218.

[58] J. F. Rodriguez, J. P. Thomas, and J. E. Renaud, "Maximizing the Strength of Fused-Deposition ABS Plastic Parts," 1999, Accessed: Aug. 10, 2024. [Online]. Available:

https://hdl.handle.net/2152/73644

[59] J. Kiendl and C. Gao, "Controlling toughness and strength of FDM 3D-printed PLA components through the raster layup," *Compos. Part B Eng.*, vol. 180, p. 107562, Jan. 2020, doi: 10.1016/j.compositesb.2019.107562.

[60] G. A. Mazzei Capote, N. M. Rudolph, P. V. Osswald, and T. A. Osswald, "Failure surface development for ABS fused filament fabrication parts," *Addit. Manuf.*, vol. 28, pp. 169–175, Aug. 2019, doi: 10.1016/j.addma.2019.05.005.

[61] C. Casavola, A. Cazzato, V. Moramarco, and C. Pappalettere, "Orthotropic mechanical properties of fused deposition modelling parts described by classical laminate theory," *Mater. Des.*, vol. 90, pp. 453–458, Jan. 2016, doi: 10.1016/j.matdes.2015.11.009.

[62] J. F. Rodríguez, J. P. Thomas, and J. E. Renaud, "Mechanical behavior of acrylonitrile butadiene styrene fused deposition materials modeling," *Rapid Prototyp. J.*, vol. 9, no. 4, pp. 219–230, Jan. 2003, doi: 10.1108/13552540310489604.

[63] M. Gokcek, Ed., "Anisotropic Mechanical Properties of ABS Parts Fabricated by Fused Deposition Modelling," in *Mechanical Engineering*, InTech, 2012, pp. 159–169.

[64] R. T. L. Ferreira, I. C. Amatte, T. A. Dutra, and D. Bürger, "Experimental characterization and micrography of 3D printed PLA and PLA reinforced with short carbon fibers," *Compos. Part B Eng.*, vol. 124, pp. 88–100, Sep. 2017, doi: 10.1016/j.compositesb.2017.05.013.

[65] S. R. Rajpurohit and H. K. Dave, "Analysis of tensile strength of a fused filament fabricated PLA part using an open-source 3D printer," *Int. J. Adv. Manuf. Technol.*, vol. 101, no. 5, pp. 1525–1536, Apr. 2019, doi: 10.1007/s00170-018-3047-x.

[66] K. M. Rahman, T. Letcher, and R. Reese, "Mechanical Properties of Additively Manufactured PEEK Components Using Fused Filament Fabrication," presented at the

ASME 2015 International Mechanical Engineering Congress and Exposition, American Society of Mechanical Engineers Digital Collection, Mar. 2016. doi: 10.1115/IMECE2015-52209.

[67] Y. Zhao, K. Zhao, Y. Li, and F. Chen, "Mechanical characterization of biocompatible PEEK by FDM," *J. Manuf. Process.*, vol. 56, pp. 28–42, Aug. 2020, doi: 10.1016/j.jmapro.2020.04.063.

[68] M. F. Arif, S. Kumar, K. M. Varadarajan, and W. J. Cantwell, "Performance of biocompatible PEEK processed by fused deposition additive manufacturing," *Mater. Des.*, vol. 146, pp. 249–259, May 2018, doi: 10.1016/j.matdes.2018.03.015.

[69] C. Hohimer, N. Aliheidari, C. Mo, and A. Ameli, "Mechanical Behavior of 3D Printed Multiwalled Carbon Nanotube/Thermoplastic Polyurethane Nanocomposites," presented at the ASME 2017 Conference on Smart Materials, Adaptive Structures and Intelligent Systems, American Society of Mechanical Engineers Digital Collection, Nov. 2017. doi: 10.1115/SMASIS2017-3808.

[70] X. Gao, D. Zhang, X. Wen, S. Qi, Y. Su, and X. Dong, "Fused deposition modeling with polyamide 1012," *Rapid Prototyp. J.*, vol. 25, no. 7, pp. 1145–1154, Jan. 2019, doi: 10.1108/RPJ-09-2018-0258.

[71] D. Zhu *et al.*, "Thermal and mechanical properties of polyamide 12/graphene nanoplatelets nanocomposites and parts fabricated by fused deposition modeling," *J. Appl. Polym. Sci.*, vol. 134, no. 39, p. 45332, 2017, doi: 10.1002/app.45332.

[72] M. Spoerk *et al.*, "Polypropylene Filled With Glass Spheres in Extrusion-Based Additive Manufacturing: Effect of Filler Size and Printing Chamber Temperature," *Macromol. Mater. Eng.*, vol. 303, no. 7, p. 1800179, 2018, doi: 10.1002/mame.201800179.

[73] M. Jin, C. Neuber, and H.-W. Schmidt, “Tailoring polypropylene for extrusion-based additive manufacturing,” *Addit. Manuf.*, vol. 33, p. 101101, May 2020, doi: 10.1016/j.addma.2020.101101.

[74] C. G. Schirmeister, T. Hees, E. H. Licht, and R. Mülhaupt, “3D printing of high density polyethylene by fused filament fabrication,” *Addit. Manuf.*, vol. 28, pp. 152–159, Aug. 2019, doi: 10.1016/j.addma.2019.05.003.

[75] T. J. Coogan and D. O. Kazmer, “Healing simulation for bond strength prediction of FDM,” *Rapid Prototyp. J.*, vol. 23, no. 3, pp. 551–561, Jan. 2017, doi: 10.1108/RPJ-03-2016-0051.

[76] C. Bellehumeur, L. Li, Q. Sun, and P. Gu, “Modeling of Bond Formation Between Polymer Filaments in the Fused Deposition Modeling Process,” *J. Manuf. Process.*, vol. 6, no. 2, pp. 170–178, Jan. 2004, doi: 10.1016/S1526-6125(04)70071-7.

[77] M. Kamyabi, R. Sotudeh-Gharebagh, R. Zarghami, and K. Saleh, “Principles of viscous sintering in amorphous powders: A critical review,” *Chem. Eng. Res. Des.*, vol. 125, pp. 328–347, Sep. 2017, doi: 10.1016/j.cherd.2017.06.009.

[78] O. Pokluda, C. T. Bellehumeur, and J. Vlachopoulos, “Modification of Frenkel’s model for sintering,” *AIChE J.*, vol. 43, no. 12, pp. 3253–3256, 1997, doi: 10.1002/aic.690431213.

[79] N. Roy, E. Buhler, and J.-M. Lehn, “Double dynamic self-healing polymers: supramolecular and covalent dynamic polymers based on the bis-iminocarbohydrazide motif,” *Polym. Int.*, vol. 63, no. 8, pp. 1400–1405, 2014, doi: 10.1002/pi.4646.

[80] I. Kammakakam, K. E. O’Harra, G. P. Dennis, E. M. Jackson, and J. E. Bara, “Self-healing imidazolium-based ionene-polyamide membranes: an experimental study on physical and gas transport properties,” *Polym. Int.*, vol. 68, no. 6, pp. 1123–1129, 2019, doi: 10.1002/pi.5802.

[81] J. Yin, C. Lu, J. Fu, Y. Huang, and Y. Zheng, “Interfacial bonding during multi-material fused deposition modeling (FDM) process due to inter-molecular diffusion,” *Mater. Des.*, vol. 150, pp. 104–112, Jul. 2018, doi: 10.1016/j.matdes.2018.04.029.

[82] M. Spoerk, J. Sapkota, G. Weingrill, T. Fischinger, F. Arbeiter, and C. Holzer, “Shrinkage and Warpage Optimization of Expanded-Perlite-Filled Polypropylene Composites in Extrusion-Based Additive Manufacturing,” *Macromol. Mater. Eng.*, vol. 302, no. 10, p. 1700143, 2017, doi: 10.1002/mame.201700143.

[83] C. Kousiatza and D. Karalekas, “In-situ monitoring of strain and temperature distributions during fused deposition modeling process,” *Mater. Des.*, vol. 97, pp. 400–406, May 2016, doi: 10.1016/j.matdes.2016.02.099.

[84] T.-M. Wang, J.-T. Xi, and Y. Jin, “A model research for prototype warp deformation in the FDM process,” *Int. J. Adv. Manuf. Technol.*, vol. 33, no. 11, pp. 1087–1096, Aug. 2007, doi: 10.1007/s00170-006-0556-9.

[85] A. Kantaros and D. Karalekas, “Fiber Bragg grating based investigation of residual strains in ABS parts fabricated by fused deposition modeling process,” *Mater. Des.*, vol. 50, pp. 44–50, Sep. 2013, doi: 10.1016/j.matdes.2013.02.067.

[86] B. N. Turner, R. Strong, and S. A. Gold, “A review of melt extrusion additive manufacturing processes: I. Process design and modeling,” *Rapid Prototyp. J.*, vol. 20, no. 3, pp. 192–204, Jan. 2014, doi: 10.1108/RPJ-01-2013-0012.

[87] S. F. Costa, F. M. Duarte, and J. A. Covas, “Thermal conditions affecting heat transfer in FDM/FFE: a contribution towards the numerical modelling of the process: This paper investigates convection, conduction and radiation phenomena in the filament deposition process,” *Virtual Phys. Prototyp.*, vol. 10, no. 1, pp. 35–46, Jan. 2015, doi:

10.1080/17452759.2014.984042.

[88] X. Zhang and J. Wang, “Controllable interfacial adhesion behaviors of polymer-on-polymer surfaces during fused deposition modeling 3D printing process,” *Chem. Phys. Lett.*, vol. 739, p. 136959, Jan. 2020, doi: 10.1016/j.cplett.2019.136959.

[89] Y. Shmueli *et al.*, “Simultaneous in Situ X-ray Scattering and Infrared Imaging of Polymer Extrusion in Additive Manufacturing,” *ACS Appl. Polym. Mater.*, vol. 1, no. 6, pp. 1559–1567, Jun. 2019, doi: 10.1021/acsapm.9b00328.

[90] B. G. Compton, B. K. Post, C. E. Duty, L. Love, and V. Kunc, “Thermal analysis of additive manufacturing of large-scale thermoplastic polymer composites,” *Addit. Manuf.*, vol. 17, pp. 77–86, Oct. 2017, doi: 10.1016/j.addma.2017.07.006.

[91] M. E. Mackay, “The importance of rheological behavior in the additive manufacturing technique material extrusion,” *J. Rheol.*, vol. 62, no. 6, pp. 1549–1561, Nov. 2018, doi: 10.1122/1.5037687.

[92] D. Bhalodi, K. Zalavadiya, and P. K. Gurrala, “Influence of temperature on polymer parts manufactured by fused deposition modeling process,” *J. Braz. Soc. Mech. Sci. Eng.*, vol. 41, no. 3, p. 113, Feb. 2019, doi: 10.1007/s40430-019-1616-z.

[93] M. S. Stark, “Improving and Understanding Inter-filament Bonding in 3D-printed Polymers”.

[94] Q. Li *et al.*, “3D printing high interfacial bonding polyether ether ketone components via pyrolysis reactions,” *Mater. Des.*, vol. 198, p. 109333, Nov. 2020, doi: 10.1016/j.matdes.2020.109333.

[95] T. D. Ngo, A. Kashani, G. Imbalzano, K. T. Q. Nguyen, and D. Hui, “Additive manufacturing (3D printing): A review of materials, methods, applications and challenges,”

*Compos. Part B Eng.*, vol. 143, pp. 172–196, Jun. 2018, doi: 10.1016/j.compositesb.2018.02.012.

[96] N. Vidakis, M. Petousis, A. Maniadi, E. Koudoumas, A. Vairis, and J. Kechagias, "Sustainable Additive Manufacturing: Mechanical Response of Acrylonitrile-Butadiene-Styrene over Multiple Recycling Processes," *Sustainability*, vol. 12, no. 9, Art. no. 9, Jan. 2020, doi: 10.3390/su12093568.

[97] Manish, D. Gurjar, S. Sharma, Akash, and M. Sarkar, "A Review on testing methods of recycled Acrylonitrile Butadiene-Styrene," *Mater. Today Proc.*, vol. 5, no. 14, Part 2, pp. 28296–28304, Jan. 2018, doi: 10.1016/j.matpr.2018.10.113.

[98] "ABS - An Engineering Plastic," AtoZ Plastics. Accessed: Jul. 12, 2024. [Online]. Available: http://atozplastics.com/upload/literature/84_abs_engineering_1.asp

[99] J. R. Wagner, E. M. Mount, and H. F. Giles, "22 - Processing Recommendations for Various Resin Systems," in *Extrusion: The Definitive Processing Guide and Handbook*, 2nd ed., in Plastics Design Library. , Elsevier Inc., pp. 255–275.

[100] "SECTION 8: GUIDES FOR THE FOLLOWING MATERIALS," in *The Dynisco Extrusion Processors Handbook*, 2nd ed., Dynisco, pp. 150–158. [Online]. Available: https://www.dynisco.com/userfiles/files/27429_Legacy_Txt.pdf

[101] "Acrylonitrile Butadiene Styrene (ABS Plastic): Uses, Properties & Structure." Accessed: Jul. 21, 2024. [Online]. Available: https://omnexus.specialchem.com/selection-guide/acrylonitrile-butadiene-styrene-abs-plastic

[102] "Compressive Strength Testing of Plastics." Accessed: Jul. 21, 2024. [Online]. Available: https://www.matweb.com/reference/compressivestrength.aspx

[103] C. Abeykoon, P. Sri-Amphorn, and A. Fernando, "Optimization of fused deposition

modeling parameters for improved PLA and ABS 3D printed structures," *Int. J. Lightweight Mater. Manuf.*, vol. 3, no. 3, pp. 284–297, Sep. 2020, doi: 10.1016/j.ijlmm.2020.03.003.

[104] D20 Committee, *Test Method for Tensile Properties of Plastics*. doi: 10.1520/D0638-14.

[105] D20 Committee, *Test Method for Compressive Properties of Rigid Plastics*. doi: 10.1520/D0695-15.

[106] K. Raney, E. Lani, and D. K. Kalla, "Experimental characterization of the tensile strength of ABS parts manufactured by fused deposition modeling process," *Mater. Today Proc.*, vol. 4, no. 8, pp. 7956–7961, Jan. 2017, doi: 10.1016/j.matpr.2017.07.132.

[107] K. Ozsoy, A. Erçetin, and Z. Çevik, "Comparison of Mechanical Properties of PLA and ABS Based Structures Produced by Fused Deposition Modelling Additive Manufacturing," *Eur. J. Sci. Technol.*, pp. 802–809, Dec. 2021, doi: 10.31590/ejosat.983317.

[108] Z. Golubović *et al.*, "A Comprehensive Mechanical Examination of ABS and ABS-like Polymers Additively Manufactured by Material Extrusion and Vat Photopolymerization Processes," *Polymers*, vol. 15, no. 21, p. 4197, Oct. 2023, doi: 10.3390/polym15214197.

[109] "ABS-M30 FDM Thermoplastic Filament." Stratasys, 2021. [Online]. Available: https://www.stratasys.com/siteassets/materials/materials-catalog/fdm-materials/abs-m30/mds_fdm_abs-m30_0921a.pdf

[110] "ABS-M30: A High Strength 3D Printing Material." Accessed: Jul. 22, 2024. [Online]. Available: https://www.stratasys.com/en/materials/materials-catalog/fdm-materials/abs-m30/?

[111] "ABS-M30 FDM Thermoplastic Filament." Accessed: Jul. 16, 2024. [Online]. Available: https://www.stratasys.com/siteassets/materials/materials-catalog/fdm-materials/abs-m30/mds_fdm_abs-m30_0921a.pdf

[112] “SR-100 Soluble Support Material - EN FDM FAQs.pdf.” Accessed: Sep. 26, 2024. [Online]. Available: https://stratasysstorage01.file.core.windows.net/portal10-files-prod/f6497a1c-ff79-4682-b983-113eff44db30/SR-100%20Soluble%20Support%20Material%20-%20EN%20FDM%20FAQs.pdf?sv=2019-07-07&sr=f&sig=wl%2FFwCH9JI6zieHHF3z4zbqYCO7efqDB02WerPlk44s%3D&st=2024-09-25T18%3A39%3A13Z&se=2024-09-27T00%3A39%3A13Z&sp=r&rsct=application%2Fpdf&rsce=UTF-8&rscd=inline%3B%20filename%3D%22SR-100%20Soluble%20Support%20Material%20-%20EN%20FDM%20FAQs.pdf%22

[113] “1D, 2D and 3D Non-Contacting Extensometers,” MTS. Accessed: Sep. 15, 2024. [Online]. Available: https://www.mts.com/en/articles/materials/1d-2d-3d-extensometers

[114] “mts-criterion-test-system-brochure.pdf.” Accessed: Sep. 15, 2024. [Online]. Available: https://www.mts.com/-/media/materials/pdfs/brochures/mts-criterion-test-system-brochure.pdf

[115] “Equipment | Garrett Melenka.” Accessed: Aug. 22, 2024. [Online]. Available: https://gmelenka.info.yorku.ca/equipment/

[116] H. Tan and S. Qu, “Impact of Cellular Materials”.

[117] D. Li, W. Liao, N. Dai, and Y. M. Xie, “Comparison of Mechanical Properties and Energy Absorption of Sheet-Based and Strut-Based Gyroid Cellular Structures with Graded Densities,” *Materials*, vol. 12, no. 13, Art. no. 13, Jan. 2019, doi: 10.3390/ma12132183.